



Complex Granular Flow Dynamics in Fruit Powder Production Lines

Ali Bakhshinejad



**Faculty of Industrial Engineering, Mechanical
Engineering and Computer Science
University of Iceland
2013**

Complex Granular Flow Dynamics in Fruit Powder Production Lines

Ali Bakhshinejad

60 ECTS thesis submitted in partial fulfillment of a
Magister Scientiarum degree in Mechanical Engineering

Advisors

Professor Piroz Zamankhan
Professor Jónas Elíasson

Faculty Representative
Professor Sigurjon Arason

Faculty of Industrial Engineering, Mechanical Engineering
and Computer Science
School of Engineering and Natural Sciences
University of Iceland
Reykjavik, May 2013

Complex Granular Flow Dynamics in Fruit powder Production Lines
Complex Granular Flow Dynamics
60 ECTS thesis submitted in partial fulfillment of a *Magister Scientiarum* degree in
Mechanical Engineering

Copyright © 2013 Ali Bakhshinejad
All rights reserved

Faculty of Industrial Engineering, Mechanical Engineering and Computer Science
School of Engineering and Natural Sciences
University of Iceland
Hjardarhagi 2-6
107 Reykjavik
Iceland

Telephone: 525 4700

Bibliographic information:

Ali Bakhshinejad, 2013, *Complex Granular Flow Dynamics in Fruit powder Production Lines*, Master's thesis, Faculty of Industrial Engineering, Mechanical Engineering and Computer Science, University of Iceland, pp. 64.

Printing: Háskólaprent
Reykjavik, Iceland, May 2013

Abstract

One of the most important parts in every industry, is packaging which is located at the last part of the product line.

In fruit powder product line lots of studies applied to study the complex dynamics of the powders in response to the vertical vibration. In this study cyclone collector condition was simulate with a rectangular throw out bin and the dynamics of the powders in response to the horizontal vibration studied. An ADXL345 accelerometer does employed in order to observe the acceleration of the system in all three dimensions.

In order to have better observation two hollow cylinder was added to the container. At the peak values of acceleration, novel swirling granular flows were observed in the cylinders while the grains cascaded down the outer surface of the piles that formed outside the cylinders.

An image processing algorithm employed to make a surface scan from the top surface of the material.

Computer simulations were performed that supported our interpretation of the dynamics observed in the experiments. And a comparison between the image processing algorithm and computer simulation evaluate our simulation results.

Dedication

To my parents and siblings

For their endless love, support and encouragement

Table of Contents

List of Figures	vi
List of Tables	ix
Abbreviations	x
Acknowledgements	xiii
1 Introduction.....	1
1.1 Application of advanced technology in agricultural farms	1
1.1.1 Value added products.....	1
1.1.2 Traditional Approach	2
1.1.3 Statistics of waste crops	4
1.1.4 Economic Analysis	4
1.1.5 Advanced methods	6
1.2 Subject of the work.....	8
1.3 Spray Drying	8
1.3.1 Atomization.....	9
1.3.2 Spray-air mixing and moisture (vaporization).....	13
1.3.1 A model for the fluid phase	18
1.3.2 Separation of the dry product from the exiting air.....	23
1.4 Dense granular materials	26
2 Materials and methods	29
2.1 Experimental setup	29
2.2 Measurement of acceleration.....	31
2.3 Particle size distribution (PSD)	38
2.4 Observations	41
2.4.1 Flowing grains in a rectangular container.....	41
2.4.2 Free surface mapping	41
3 Results[103]	43
3.1 Computer Simulations.....	43
3.2 Polydisperse aggregates	43
3.3 Simulation of sand perturbed by an orbital shaker.....	46
3.4 Simulation of swirling granular flows.....	47
4 Conclusions.....	49
References	51
Appendix A.....	56

List of Figures

Figure 1-1: Various value-adding processes	1
Figure 1-2: The traditional approach to food processing	2
Figure 1-3: a) Peach halves being sun dried. b) A zoom-out view of the same.....	3
Figure 1-4: Relative strength of solar irradiance at Earth's surface.....	4
Figure 1-5: Top industries: Fast growers [14].....	5
Figure 1-6 Average annual expenditure of U.S. households on food [15].....	6
Figure 1-7: Production scheme and sampling of different fruit products (juice, concentrate, powder) [23].....	7
Figure 1-8: Spray-drying process and plant [24]	8
Figure 1-9: Wheel atomizer with straight radial vanes	11
Figure 1-10: Various designs of wheel atomizers.....	11
Figure 1-11: A pressure nozzle	12
Figure 1-12: A system of multiple nozzles in a single drying chamber.....	12
Figure 1-13: Spray-dried powder: (a) produced by a wheel atomizer; (b) produced by a pressure nozzle	13
Figure 1-14: A schematic illustration of the forces acting on particle i from contacting particle j and non-contacting particle k	14
Figure 1-15: Two-stage drying of droplets containing solids	19
Figure 1-16: Particle traces colored by particle surface temperature (in K).	22
Figure 1-17: Three-dimensional contours of particle concentration at $t = 30$ s. (a) DD + PP model, (b) DD model built in ANSYS FLUENT solver, (c) the difference between the two model predictions. Left – XZ cut, middle – YZ cut, right – isometric view.....	23
Figure 1-18: A cyclone collector.....	24
Figure 1-19: A schematic and grid representation of the cyclone considered, together with the definition of the sections: (a) 3D view of geometry; (b) 3D view of CFD grids; (c) top view of the sections; and (d) front view of the sections.	25

Figure 1-20: Snapshots showing the flow of particles in a cyclone with solid loading ratio 2.5 (colors signify particle velocity in the z direction)	26
Figure 2.1: (a and b) Images of the container and nomenclature. The dimensions of the container are $W = 18$ cm, $L = 28$ cm, and $H = 7$ cm.	30
Figure 2.2 The ellipse-type orbits of the shaker.	31
Figure 2.3 Differential temperature sensing inside a closed chamber: (a) hot air bubble experiencing no acceleration, (b) no temperature difference sensed at zero acceleration, (c) a hot air bubble shifted due to acceleration, and (d) a temperature difference sensed due to acceleration [92].....	32
Figure 2.4 Mass-spring damper system.....	33
Figure 2.5: Top and cross-sectional views illustrating the triple-axis detection principle. The four seismic masses are suspended from thin beams oriented in different $\{1\ 1\ 1\}$ planes.	35
Figure 2.6: A single sensing element with a capacitor plate for read-out. A local coordinate system, x' , y' and z' , oriented along the $\{1\ 1\ 1\}$ plane of the crystal, is used for the analytical model.....	36
Figure 2.7: A schematic view of a surface micromachined polysilicon accelerometer	37
Figure 2.8 a) A stack of sieves, schematic b) The stack of sieves on a shaker used in this study.....	38
Figure 2.9 The particle size distribution of the sand used in the current study. The crosslets signify the results of the sieving. The solid line is a log-normal fit with location and scale parameters $\mu = 0.69$ and $\sigma = 0.68$, respectively.	40
Figure 2.10 An image of a pile of a ternary mixture of glass beads used in the current study on a flat surface. The slope of the pile is $\theta_s = 34^\circ$	40
Figure 2.11 (a) Multi-camera arrangement. Six cameras were located at the vertices of a regular hexagon with side length of 35 cm, $R = 35$ cm, and $\theta = 60^\circ$. (b) An instantaneous free surface, obtained using Autodesk 123D Catch. The sampling slice is located at $x = L$, where L is approximately 10 cm. (c) A set of cross-sectional views of the free surface of the sand in the container. (d) The contour of the free surface on the sampling slice shown in (b).....	42
Figure 3.1 (a) A polydisperse aggregate and its computational grid. The diameters of ball-1, ball-2 and ball-3 are 500 μm , 350 μm , and 600 μm , respectively. (b) Time evolution of the dimensionless velocities of the particles in the aggregate. At the end of the contact process, ball-2 and ball-3 stuck together. (c and d) Time evolution of the translational and angular	

velocities of the particles in the aggregate. The two configurations are separated by $t = 20 \mu\text{s}$ 43

Figure 3.2 (a) The computed dimensionless velocity of particles in the x-direction as a function of time using FEM. Here and in (c) and (e), squares, circles and diamonds represent the dimensionless velocities of “ball 1”, “ball 2”, and “ball 3”, respectively. (b) The computed dimensionless velocity of particles in the x-direction as a function of time. Here and in (d) and (f), the results were obtained with a simplified model. (c) The computed dimensionless velocity of particles in the y-direction as a function of time using FEM. (d) The computed dimensionless velocity of the particles in the y-direction as a function of time. (e) The computed angular velocity of particles in the z-direction as a function of time using FEM. (f) The computed angular velocity of particles in the z-direction as a function of time..... 45

Figure 3.3 (a) The initial configuration of the solid particles used for the numerical simulation where $h_{p0} = 3.5 \text{ cm}$. (b) The instantaneous configuration of the solid particles at $t = 1 \text{ s}$, with $W_b = 14 \text{ cm}$ and $L_b = 24$. (c) The instantaneous configuration of the solid particles at $t = 2 \text{ s}$. (d) The computed average particle velocity distribution on a $y z$ -plane. Inset: the free surface and position of the plane, $L_s = 11 \text{ cm}$ 46

Figure 3.4 (a and b) The initial configuration of the solid particles used for the numerical simulation, where $h_{p0} = 3.5 \text{ cm}$, $H = 6 \text{ cm}$, $W_b = 14 \text{ cm}$, $L_b = 16 \text{ cm}$, $h_c = 3.2 \text{ cm}$, $t = 0.2 \text{ cm}$ and $\Delta h_p = 0.3 \text{ cm}$ 47

Figure 3.5 (a–c) The instantaneous configuration of the solid particles at $t = 2 \text{ s}$. (d) The computed average particle velocity field in the xy -plane at $z_1 = 3.22 \text{ cm}$. (e) The computed average particle velocity field in the xz -plane at $y_1 = 0$. (f) The computed average air velocity field in the same xy -plane as (d). 48

List of Tables

Table 1.1: Spherical droplet surface versus droplet size	10
Table 1.2: Range of droplet and particle sizes obtained in spray dryers (μm):.....	10
Table 1.3: Contact force and torque models.....	15
Table 1.4: Particle-fluid interaction forces	17
Table 2.1 Material properties [83, 84]	29
Table 2.2: Geometrical parameters of the accelerometer design.....	36
Table 2.3: A set of data collected from the accelerometer	37
Table 2.4 Sieve analysis results.....	39

Abbreviations

Index	Description	Unit	Equation
$I(r)$	Irradiance at distance r from the sun	W/m^2	(1.1)
E	Irradiance at the surface of the sun	W/m^2	(1.1)
R	Radius of the sun	Km	(1.1)
r	Distance from the sun	Km	(1.1)
ρ_g	Air density	kg/m^3	(1.2)
v_g	Air velocity	m/s	(1.2)
v_f	Feed fluid velocity	m/s	(1.2)
d_p	Droplet diameter	m	(1.2)
σ	Surface tension	N/m	(1.2)
v_i	Translational velocities of particle i		(1.4)
ω_i	Angular velocities of particle i	rad/s	(1.4)
F_{ij}^c	Contact force acting on particle i by particle j or walls	N	(1.4)
M_{ij}	Torque acting on particle i by particle j or walls	N.m	(1.5)
F_{ik}^{nc}	Non-contacting force acting on particle i by particle k or other sources	N	(1.4)
F_i^f	Particle-fluid interaction force on particle i	N	(1.4)
F_i^g	Gravitation force	N	(1.4)
A_x	Displacement amplitudes of the vibrating container in x direction	m	(1.31)
A_y	Displacement amplitudes of the vibrating container in y direction	m	(1.31)
ω_x	Angular frequencies of the vibration in x direction	rad/s	(1.31)

ω_y	Angular frequencies of the vibration in y direction	rad/s	(1.31)
e_x	Unit vectors in x direction		(1.31)
e_y	Unit vectors in y direction		(1.31)
a	Acceleration applied to the system	m/s^2	(2.2)
ρ	Density of the fluid inside the chamber	kg/m^3	(2.2)
μ	Fluid viscosity		(2.2)
x	Characteristic dimension		(2.2)
β	Fluid's volumetric coefficient of thermal expansion	$1/T$	(2.2)
ΔT	Temperature difference between the heater and the boundary of the system	$^{\circ}C$	(2.2)
m	Mass of the proof-mass	Kg	(2.5)
z	Relative movement of the proof-mass with respect to frame	m	(2.5)
c	Damper coefficient	Ns/m	(2.5)
k	Spring constant	N/m	(2.5)
F	Force applied	N	(2.5)
ω_n	Un damped resonance frequency	Hz	(2.11)
ζ	Damping factor		(2.12)

Acknowledgements

I would like to express my deep gratitude to my master thesis advisor, Dr. Piroz Zamankhan. I have learned many things since I commenced my study under supervision of Dr. Piroz Zamankhan. He spends much time instructing me how to write a paper, explore in literature and collect data. I am also grateful to Dr. Jónas Elíasson and Dr. Sigurjon Arason for spending time read this thesis and providing me with useful suggestions regarding this thesis. In addition, I would like to appreciate Dr. Ólafur Pétur Pálsson's support during my study time at the University of Iceland not just as the head of faculty but more likely as a friend. They are all hard-working professors and I believe their academic achievements will continue to increase.

My special thanks are given to my good friends, Kevin Frank and Hrafn Arnorsson for their great proofread for my paper. Also I would thank my best friend Elvar Karl Bjarkason for his support and endless helps.

I also want to appreciate the great helps and efforts of Dr. Wu in order to publish my paper in their 2012 last issue of the Particuology Journal.

Last but not the least important, I owe more than thanks to my family, in particular my parents, my great uncle, and an elder brother, for their financial support and encouragement throughout my life at graduate institute.

1 Introduction

1.1 Application of advanced technology in agricultural farms

1.1.1 Value added products

The structure of agricultural production in developing countries has radically changed in the last two decades. Since the late 60s and 70s, the World Bank and its various agricultural research institutes have actively promoted the adoption of industrial (high chemical input) agricultural methods. This soon brought about the so-called Green Revolution [1], involving ‘miracle’ seeds that promised landfall yields. It was expected these high technology methods would benefit all farmers, including the poor [2].

Forty years after the beginning of the Green Revolution, most farmers in developing countries still work in a traditional way. A way to measure this is by transportation time [3, 4]. A significant percentage of these ‘landfall yields’ go to waste. The waste is generated at two different time points; firstly, it is what falls from the tree before the harvest time and secondly, it is what gets wasted in transportation.

Throughout the long history of agriculture, farmers have tried to add value to their crops in various ways. Processes used involved one or several of those shown in Figure 1-1. During the long period of time involved, great ingenuity has been used to improve the processes.

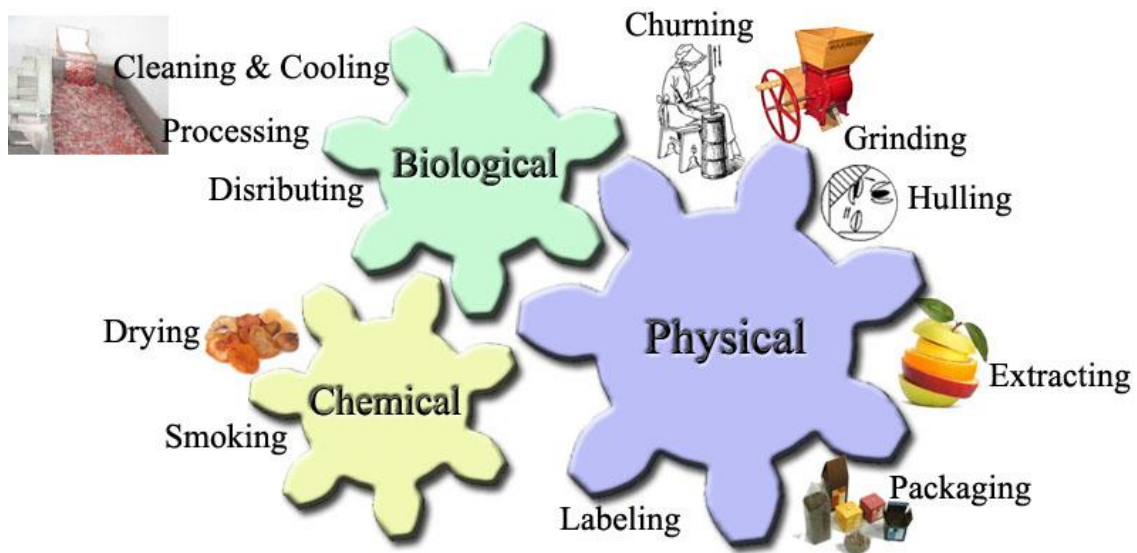


Figure 1-1: Various value-adding processes

Fruit powder is the product of one of the processes. Fruit powders have many interesting qualities such as long shelf life, multiple uses and easy packaging. During the drying process, fruit powders, being an example of a granular material, are vibrated [5]. Powders

or granular materials are abundant in nature and their response to vibration plays an important role in various natural events such as earthquakes [6] and avalanches [7].

1.1.2 Traditional Approach

The traditional agricultural process may be modeled as shown in Figure 1-2.

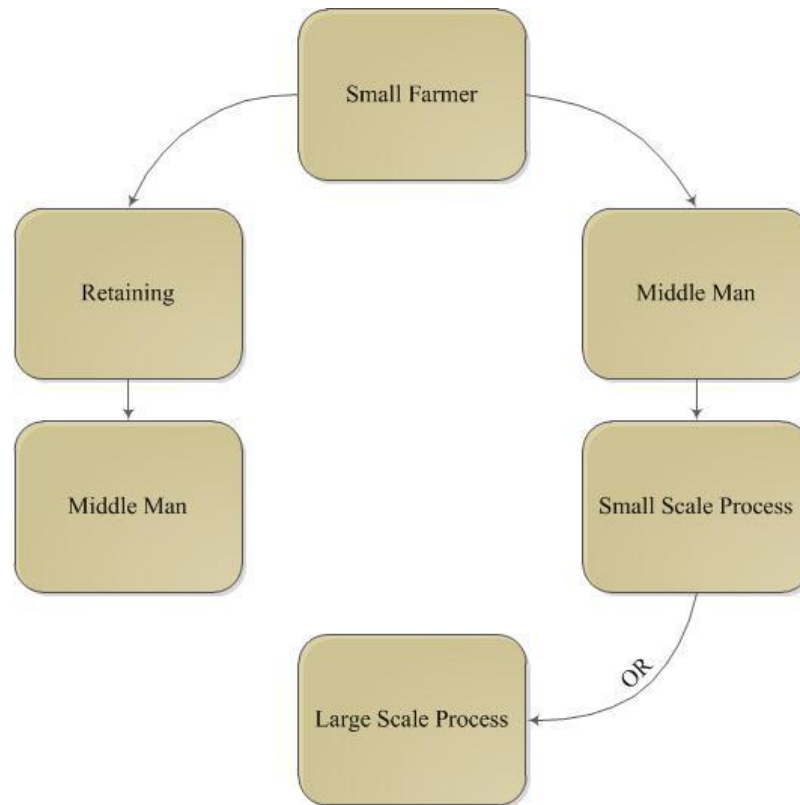


Figure 1-2: The traditional approach to food processing

Dry crops are a common type of agricultural products with a wide range of usage. In countries with abundant sunshine (see Figure 1-4), farmers started drying their crops by laying them out in the sun already in ancient times.

The traditional way of solar drying is as follows. After selecting the suitable fruits for drying, they are sulfured, cut in half and laid out in the sun [8]. Four days later, what was originally big juicy halves of fruits have shrunk and started to look like dried fruits (Figure 1-3). There is space in the previously crowded fruit trays. However, the halves are still moist and gooey and will not store at this point; they will take several more days to finish.

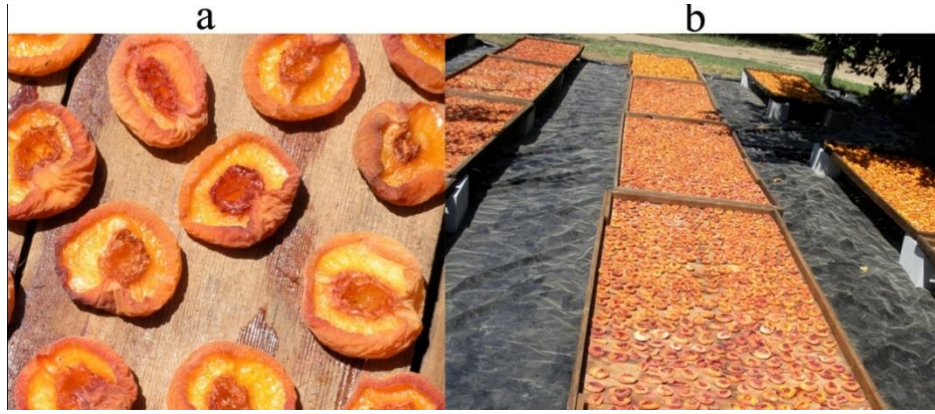


Figure 1-3: a) Peach halves being sun dried. b) A zoom-out view of the same

As is evident from this description and great space is needed for this process as well as a long time.

The *solar constant* is defined as the average amount of solar electromagnetic radiation per unit area that would be received on a plane perpendicular to the incoming radiation at the distance of one astronomical unit (AU) from the sun [9].

The *inverse square law* is used to calculate the decrease in radiation intensity due to an increase in distance from the radiation source. Thus, *irradiance* (power per unit area) with the sun as source may be given as [9]

$$I(\mathbf{r}) = E \frac{4\pi R^2}{4\pi r^2} \quad (1.1)$$

The real amount of solar energy that impinges on Earth's surface is a function of latitude, time of year, time of day, and weather conditions. Calculating it in specific instances is outside of the scope of this study. However, the following figure from Loster [10] (Figure 1-4) shows the areas on Earth that receive enough sunshine for traditional sun drying to be practical (the yellow and orange colored areas).

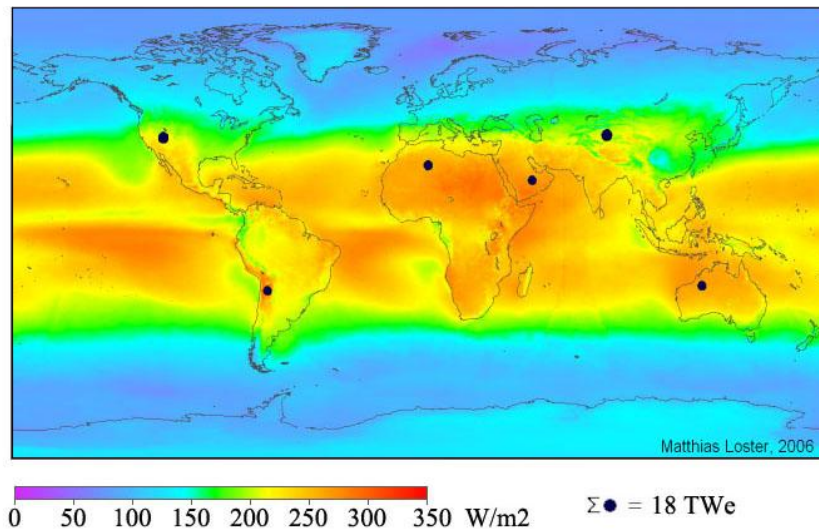


Figure 1-4: Relative strength of solar irradiance at Earth's surface

1.1.3 Statistics of waste crops

Apples are one of the most common fruit crops in Iran. The introduction of advanced techniques for apple cultivation has further enhanced their production. In 2007, Iran held the 3rd place in global apple production (about 2,660,000 tons) and the 8th place in global peach production (about 421,000 tons) [11]. Both fruit types have a short post-harvest shelf life because of their highly perishable nature. Unlike developed countries, in Iran less than 2% of the annual agricultural output result in consumer-grade products by value-adding processes of fruits [3]. A short shelf life and increased production necessitates the development of nonconventional products from apples. More than 250,000 tons of apples were wasted in transportation for the domestic market in Iran in 2007 [3], about 10% of the total production. Ilyas et al. [4] have reported a 23% waste of the apple production in transportation in Pakistan. As a contrast, in the same year the U.S. Apple Association [12] reported that 32% of the U.S apple crop was processed, more than 99% of which were marketed.

The Economic Research Service of the U.S. Department of Agriculture [13] has reported that fresh produce constitute 45% of the total peach consumption and processed products 55%. The same relations in Iran would mean that 189,450 tons of peaches would be consumed fresh while 231,550 tons would be processed.

Traditional sun drying not only requires large amounts of time and space, it is also evident from the figures that a considerable proportion of the crops go to waste.

1.1.4 Economic Analysis

There are various types of fruit processing processes, such as biological, chemical and physical. Examples of value-added products are: ketchup, juice, baby food, dried fruits and fruit powder.

CNN Money [14] reported the food industry as having a strong growth rate of 8.3% (Figure 1-5)

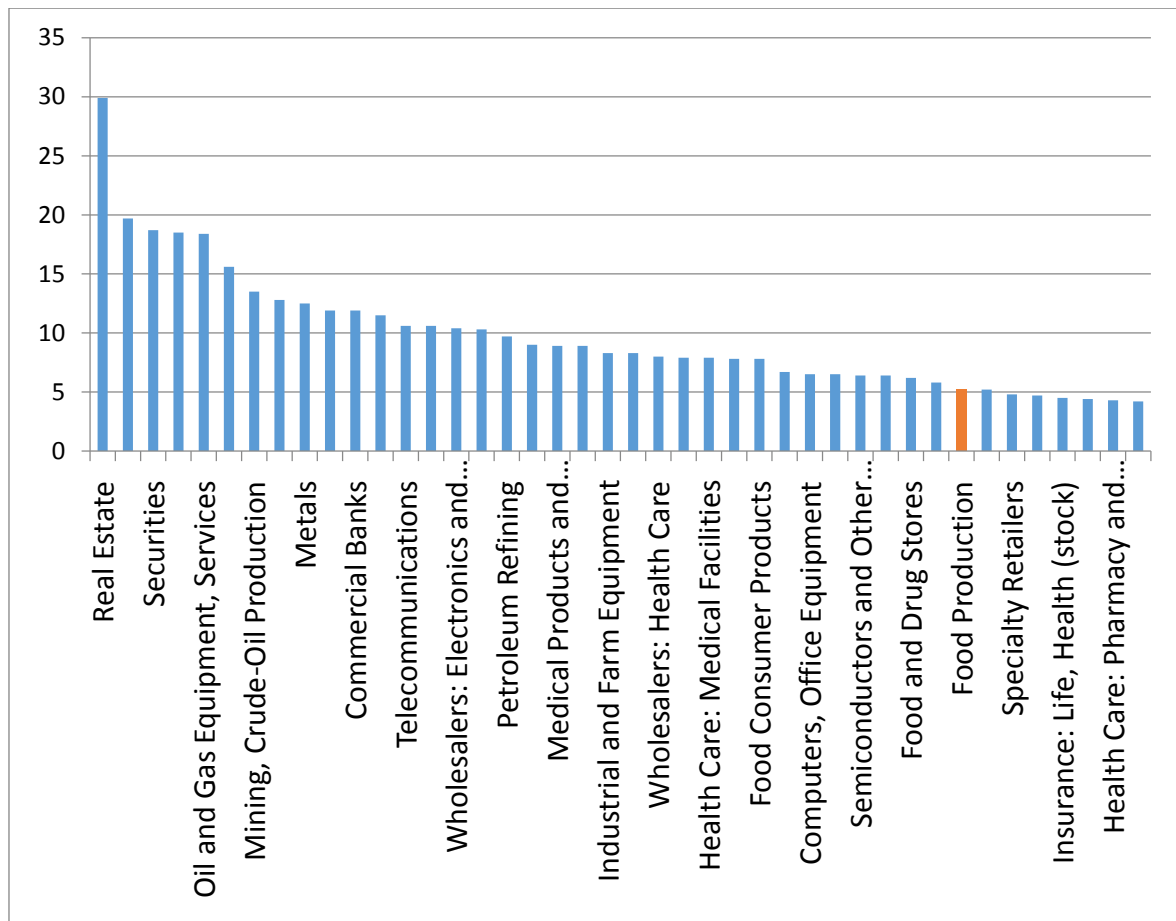


Figure 1-5: Top industries: Fast growers [14]

On average, consumers spend more money on fruits and vegetables than on any other type of food, see Figure 1-6 [15], the other categories being sugar, oils and fats, miscellaneous food, and non-alcoholic beverages. Annual household expenditure on vegetables and fruits in U.S.A. equals 18% of the total expenditure on food or \$858, of which fresh fruits account for \$295, fresh vegetables \$279, processed fruits \$174 and processed vegetables \$137.

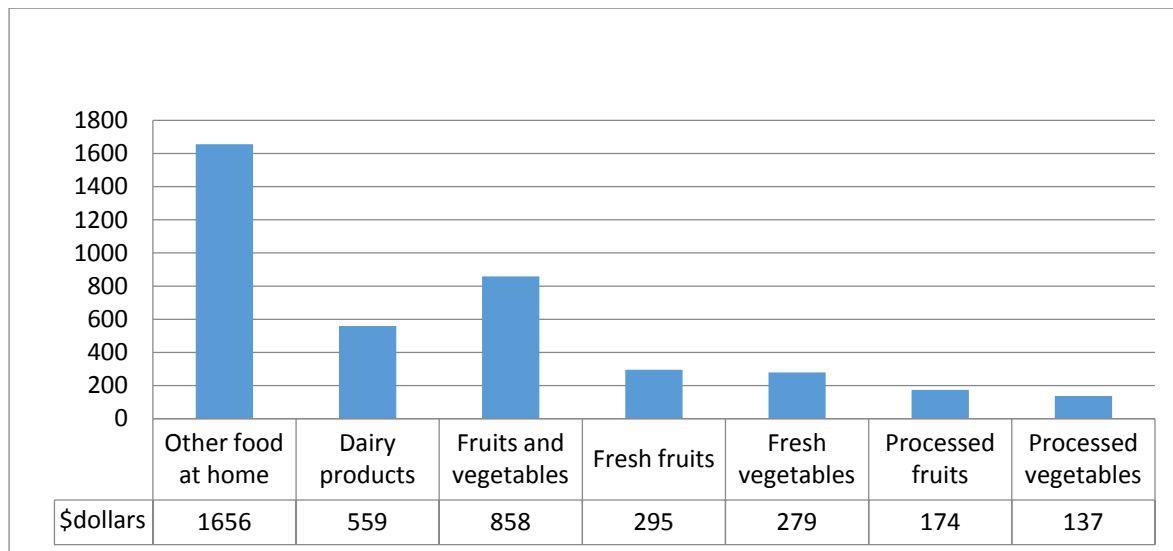


Figure 1-6 Average annual expenditure of U.S. households on food [15]

Vegetables and fruits are universally acclaimed for their health benefits [16]. They contain almost all of the essential vitamins, minerals, and fibers. A diet high in fruits is linked to a lower risk of getting several chronic degenerative diseases, including certain cancers and cardiovascular disease [17]. Moreover, it is beneficial for weight management as it facilitates a reduced-energy diet [18].

According to Mintel [19], annual consumer spending on fruit juices and fruit beverages in U.S.A. was approximately \$19 billion that year. Fruit juices represent the major form of the U.S. fruit consumption [20], accounting for 44% of commercially marketed fruit products in 2000 [21].

1.1.5 Advanced methods

Dried fruits are used extensively by the confectionery, baking, and sweets industries. Soup manufacturing plants use dried fruits in various sauces, garnishments, pudding, ice powders and food for infants and children. An example is fruit powder processed from juice or pulp that dissolves quickly [22].

Considering the large amount of fruits that go to waste in developing countries and the existing multibillion markets for processed fruits, there would seem to be considerable room for improvement in the way of increasing the amount of processing soon after harvesting, before the fruits have time to go to waste.

In countries like Iran where fruit trees produce fruits year round, it is quite feasible to implement a simple technology for extracting 60–70% of the material of apples in the form of juice and drying the remaining pulp into a fine powder.

In recent years, there have been several studies suggesting redesigns and improvements of the process line. Figure 1-7 shows the common existing fruit juice process line.

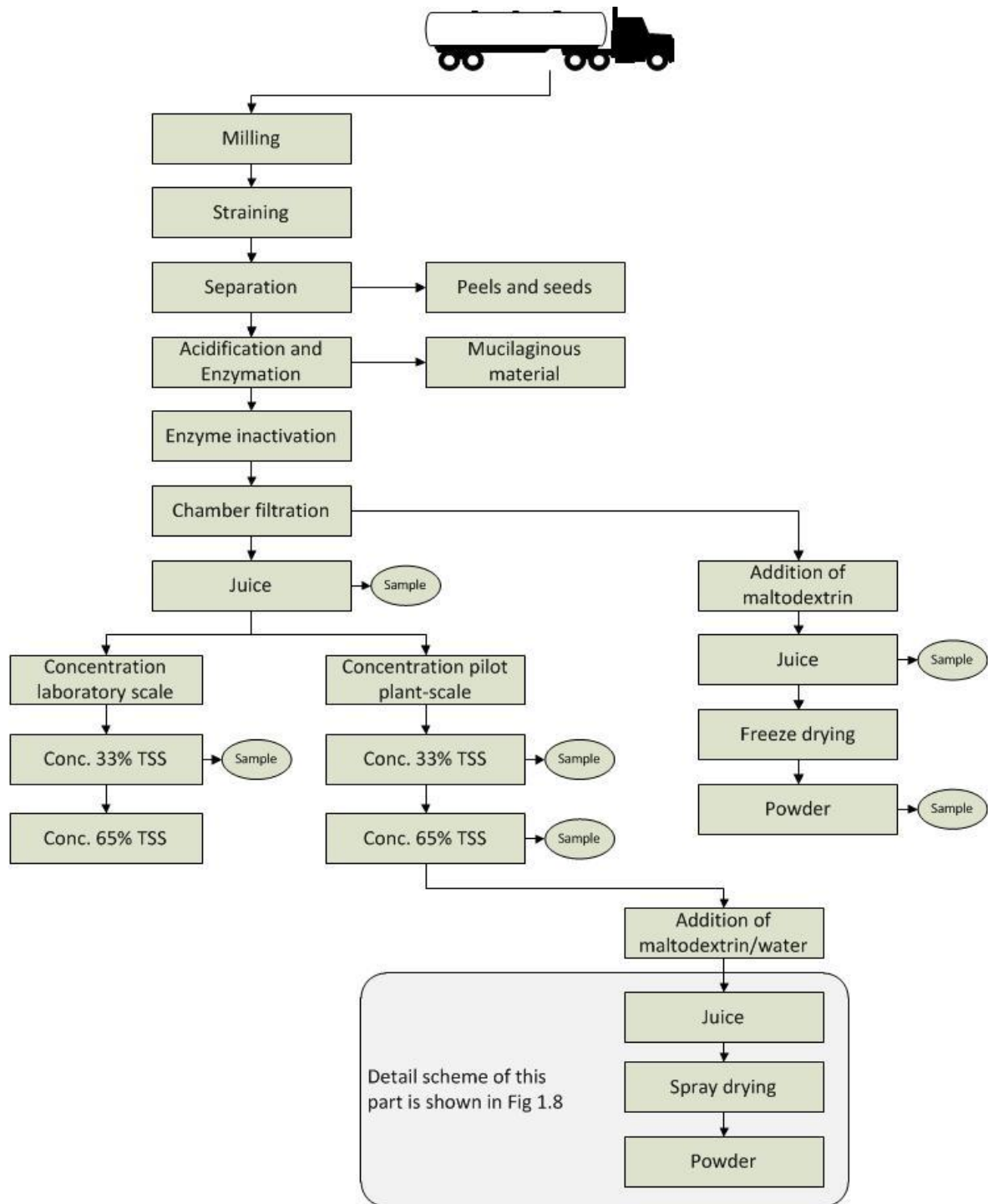


Figure 1-7: Production scheme and sampling of different fruit products (juice, concentrate, powder) [23]

Several studies have focused on the spray-drying processing line. There have been separate studies into each part of the line, such as the spray-dryer and the cyclone collector. (The spray-drying part of the process line in Figure 1-8 is especially designed to produce fruit powders). All of those studies have attempted to model, redesign and improve the efficiency of the part in question, usually focusing on improving the main parts. The

behavior of powder is mostly governed by both horizontal and vertical vibration, however, most of these studies consider only vertical vibrations.

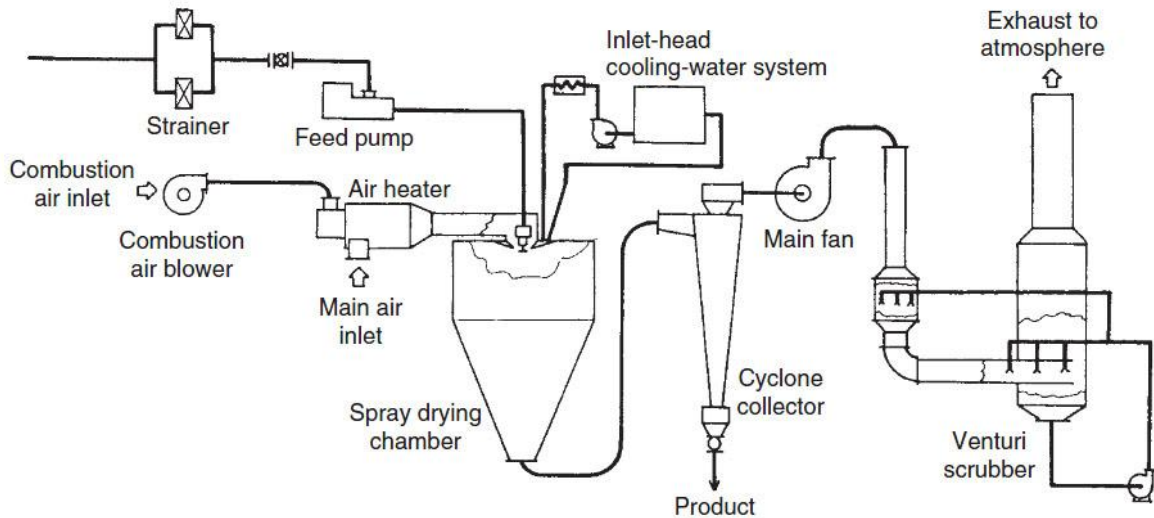


Figure 1-8: Spray-drying process and plant [24]

1.2 Subject of the work

This work was concerned with the effects of horizontal vibration on granular flows composed of different-sized particles. Its main goal was to understand the dependency of these effects on the material parameters of the granular material. This was done by setting up a computational model of the flow and running it in a computer cluster. The same flow was performed experimentally and used to verify the model using one of the most advanced image processing algorithms.

1.3 Spray Drying

The last step of the process line in Figure 1-7 is spray-drying. Spray-drying is a suspended particle process (SPP) technique designed to dry droplets generated by a liquid feed to solid particles by letting them move through hot air. It is a single-step, continuous process which can operate with different capacities [24]. The history of this method dates back to around 1800 and its use on an industry scale to around 1850 [25].

The spray-drying process takes place in the following way: The liquid feed is pumped to the atomizer whose placement depends on the design; usually it is placed at the top of the drying chamber. The drying air is drawn from the atmosphere by a supplying fan and is heated by the air heater from which it goes to the air distributor. The droplets that are generated by the atomizer get into contact with the hot air. During the evaporation process, the air cools. After the droplets have dried in the chamber, they pass through the cyclone which separates the dried particles from the hot air [24].

So, generally, spray-drying consists of three process steps:

- Atomization
- Spray-air mixing and moisture evaporation
- Separation of dry product from the exiting air

1.3.1 Atomization

The atomizer is the most important part of every spray dryer. It is small in size. Its design is governed by several requirements which are summarized below [26]:

- It must disperse the liquid feed into small droplets, which should be well distributed within the dryer and mixed thoroughly with the hot gas.
- The droplets must not be so large as to be incompletely dried, nor so small as to make product recovery difficult. Also, too small droplets may overheat and scorch.
- The atomizer must also act as a metering device, controlling the rate at which the material is fed into the dryer.

Drop Formation

Most atomizers generate a large number of small drops by shattering a continuous jet or sheet of liquid, usually by aerodynamics forces generated by the relative motion of the phases. Mechanical, centrifugal, electrical, and ultrasonic force fields may also be used.

The most important dimensionless measure of the stability of a single droplet is the Weber number based on relative velocity and gas density [27]:

$$We = \frac{\rho_g (v_g - v_f)^2 d_p}{\sigma} \quad (1.2)$$

For non-viscous fluids the critical value of the Weber number, above which droplets will break up, is about 12.

In the breakup process, the drop is punched into a baglike shape by the dynamic pressure of the gas acting at the stagnation point. The bag finally bursts to form a ring of smaller droplets.

If a drop is introduced into a gas stream at high values of the Weber number, several generations of droplets will be produced by successive shattering. An expression for the final drop size under these conditions is [27]:

$$\left(\frac{d}{d_0}\right)^{0.25} = \frac{1.9}{(We)_0^{0.25}} + 0.315 \left(\frac{\rho_g}{\rho_f}\right)^{1.5} (C_D)_0 (We)_0^{0.125} \ln\left(\frac{d_0}{d}\right) \quad (1.3)$$

where the subscript 0 refers to the initial conditions.

The drop sizes control the heat transfer surface available and thus the drying rate. Mujumdar [24] presents a comparison of spherical droplet surface and droplet size as shown in Table 1.1.

Table 1.1: Spherical droplet surface versus droplet size

Total volume (m³)	Diameter of droplets	No. of droplets	Surface per droplet	Total surface of droplets (m²)
1	1.234 m	1	3.14 m ²	3.14
1	1 cm	1.986×10^6	3.14 cm ²	623.6
1	1 mm	1.986×10^9	3.14 mm ²	6236
1	100 μm	1.986×10^{12}	31400 μm ²	62360
1	1 μm	1.986×10^{18}	3.14 μm ²	6236000

There are four different general types of atomizers available. The ones most commonly used are the rotary wheel atomizer and the pressure nozzle single-fluid atomizer. Pneumatic two-fluid nozzles are used only rarely in very special applications. Typical ranges of disintegrated droplets and particle sizes of various products in a spray dryer are listed in Table 1.2 [24].

Table 1.2: Range of droplet and particle sizes obtained in spray dryers (μm):

Rotating wheels	1-600
Pressure nozzles	10-800
Pneumatic nozzles	5-300
Sonic nozzles	5-1000

The rotary wheel atomizer and the pressure nozzle will now be briefly introduced.

Rotary wheel atomizer

A typical design of a wheel atomizer is shown in Figure 1-9. Liquid is fed from the center pipe, moves to the edge of the wheel under the centrifugal force and turns into droplets at the wheel's edge. Because of the straight radial vanes configuration of this model, the spray angle is about 180° and forms a broad cloud. The resulting large horizontal trajectories require the atomizer to be contained in a large-diameter chamber. The most common design of a wheel atomizer has radial vanes [24].

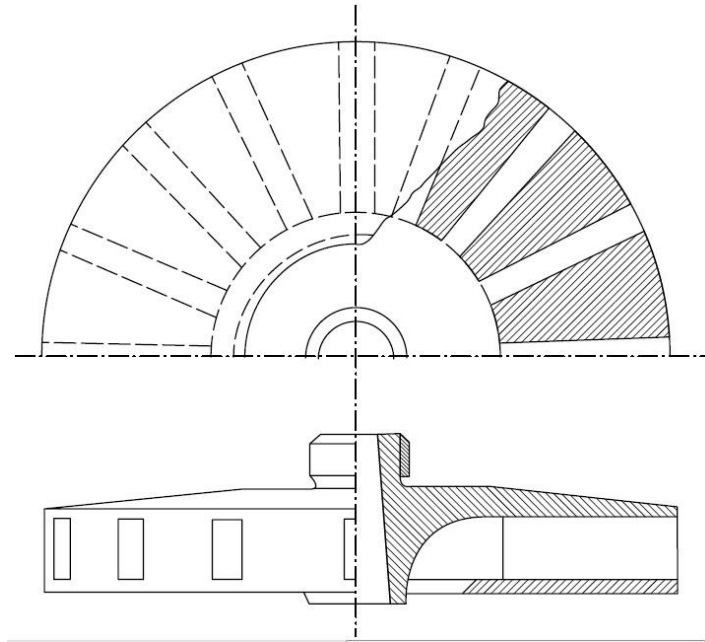


Figure 1-9: Wheel atomizer with straight radial vanes

The number and shape of the vanes differ according to the product quality and capacity requirements. Figure 1-10 shows three different types of wheel atomizers [24].

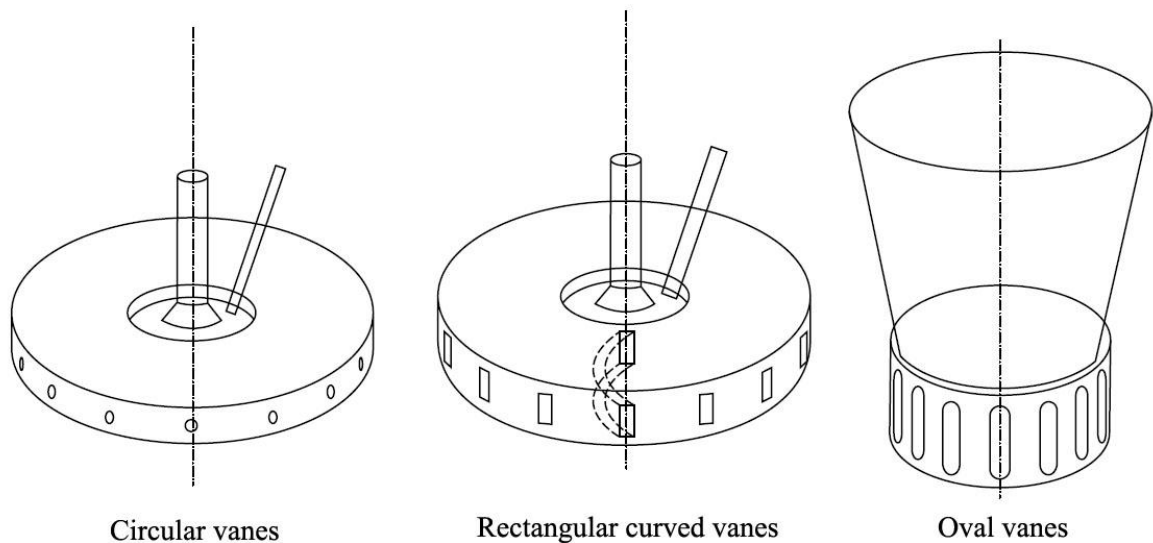


Figure 1-10: Various designs of wheel atomizers

Pressure nozzles

A pressure nozzle or single-fluid nozzle generates spray by applying pressure to the liquid as it passes through the nozzle, usually in the range of 5-7 MPa, see Figure 1-11 [24].

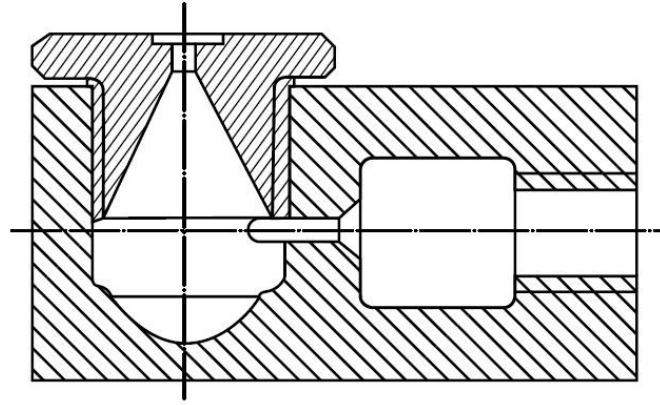


Figure 1-11: A pressure nozzle

The liquid leaves the nozzle's orifice in the form of a hollow cone at an angle that varies from 40° to 140° . The diameter of the orifice is usually between 0.4–4 mm and usually the capacity of the nozzle does not exceed 100 L/h. For larger feeds, usually several nozzles are used in one drying chamber like that shown in Figure 1-12 [28].

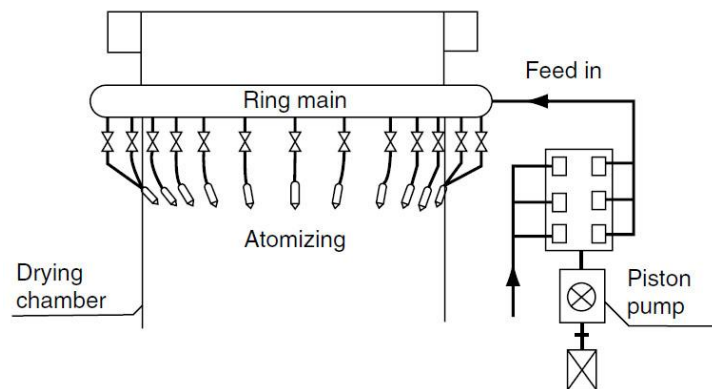


Figure 1-12: A system of multiple nozzles in a single drying chamber.

Mujumdar [24] presented a picture of droplets that were produced by a rotating wheel and a pressure nozzle, see Figure 1-13.

A study of the mathematical model of atomizers is outside of the scope of this thesis. Here, common structure models of nozzles are just briefly reviewed.

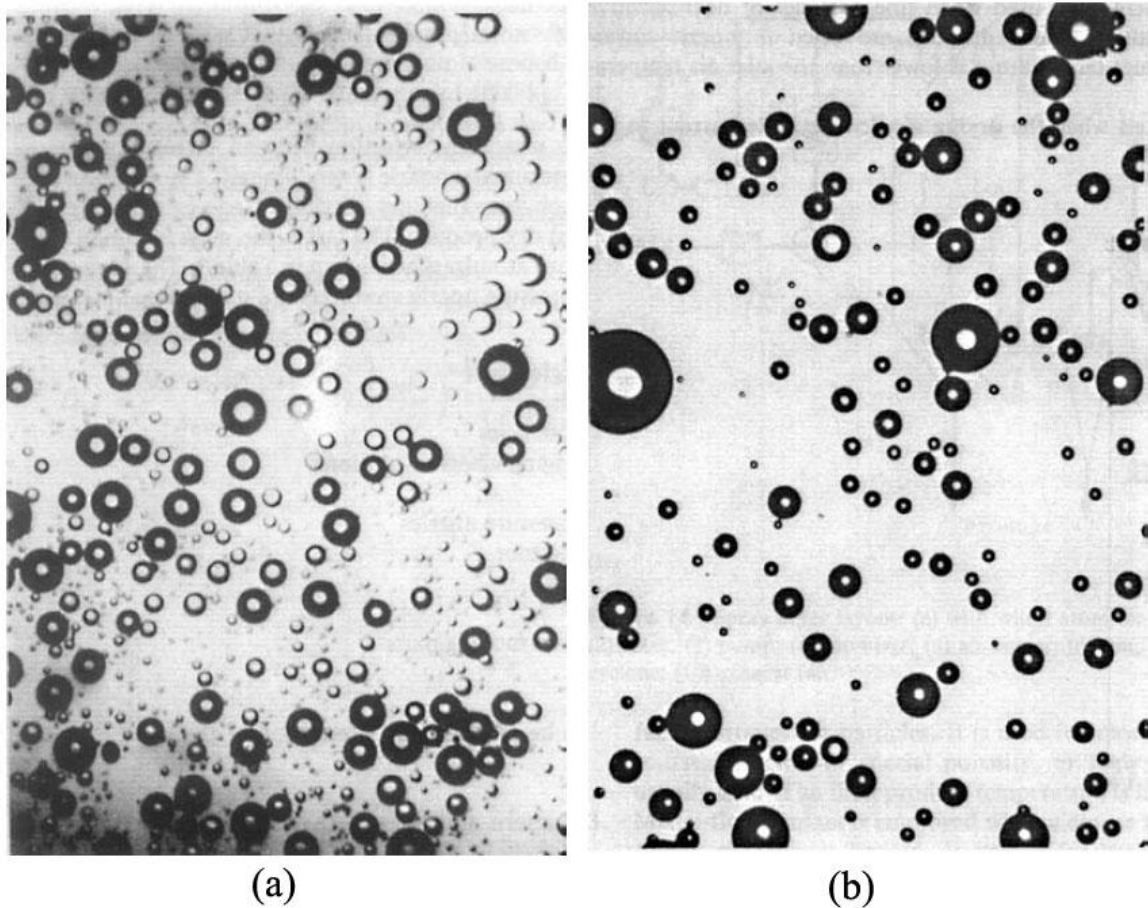


Figure 1-13: Spray-dried powder: (a) produced by a wheel atomizer; (b) produced by a pressure nozzle

1.3.2 Spray-air mixing and moisture (vaporization)

The process of spray-drying is a complex multi-phase system which includes the gas phase (drying air), liquid phase (droplets) and solid phase (particles). To make things worse, each phase is not pure but a mixture of several components. The theoretical modeling of such system is a difficult task and cannot be solved without some simplifications [29].

Mathematical models for numerical calculations that have enjoyed popularity thus far can be grouped into two categories: the continuum-continuum approach at a macroscopic level represented by the so called two-fluid model (TFM)[30], and the continuum-discrete approach at a microscopic level mainly represented by the so-called combined continuum and discrete model (CCDM) which is sometimes referred to as the computational fluid dynamics and discrete-element method (CFD-DEM) [31, 32].

In CCDM, the motion of particles is modeled as a discrete phase, described by Newton's laws of motion on an individual particle scale, while the flow of fluid (gas or liquid) is treated as a continuum phase, described by the local averaged Navier-Stokes equations on a computational cell scale. The method has been recognized as an effective method to study the fundamentals of particle-fluid flow under different conditions, as briefly reviewed by various researchers [32, 33].

As mentioned before, there are different models for calculating multiphase systems. The DEM model will now be considered.

The Discrete Element Method (DEM)

A particle in a multiphase system may have two types of motion: translation and rotational. During its movement, it interacts with neighboring particles, the container's wall and with the surrounding hot air, exchanging momentum and energy [34].

Cundall and Strack [35] showed that in the DEM approach, by choosing a numerical time step less than a critical value, during a single time step, the disturbance cannot propagate from the particle and fluid farther than its immediate neighboring particles and vicinal fluid.

The governing equations for the translational and rotational motion of particle i with mass m_i and moment of inertia I_i can be written as:

$$m_i \frac{dv_i}{dt} = \sum_j F_{ij}^c + \sum_k F_{ik}^{nc} + F_i^f + F_i^g \quad (1.4)$$

$$I_i \frac{d\omega_i}{dt} = \sum_j M_{ij} \quad (1.5)$$

Figure 1-14 schematically shows typical forces involved in a DEM simulation [34].

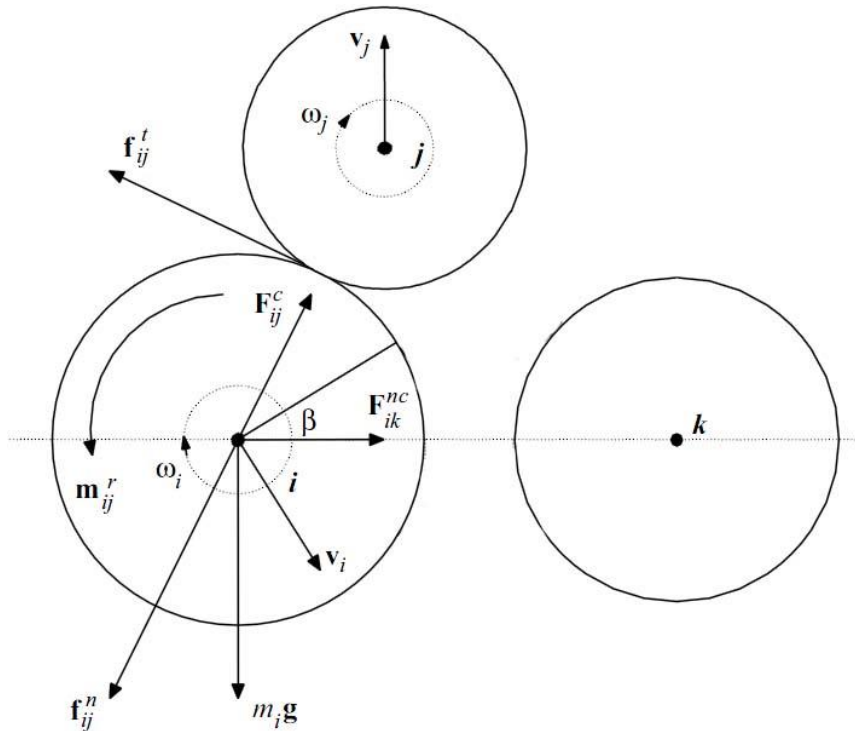


Figure 1-14: A schematic illustration of the forces acting on particle i from contacting particle j and non-contacting particle k .

Various models have been proposed to calculate these forces and torques; these are summarized in Table 1.3

Table 1.3: Contact force and torque models

Force Models	Normal Force	Tangential Force	References
Linear spring-dashpot model	$f_n = -K_n \delta_n n_c - C_n (v_c \cdot n_c) n_c$	$f_t = -K_t v_c^t + C_t (v_c \times n_c) \times n_c$	[35]
Simplified Hertz-Mindlin and Deresiewicz model	$f_n = -\frac{4}{3} E^* \sqrt{R^*} (\delta_n)^{3/2} n_c - C_n (8m^* E^* \sqrt{R^*} \delta_n)^{1/2} \cdot (v_c \cdot n_c) n_c$	$f_t = -\mu f_{n,c} (1 - (1 - v_c^t /\delta_{max})^{3/2}) \hat{v}_c^t + 2C_t \left(1.5\mu m * f_{n,c} \cdot \sqrt{1 - v_c^t /\delta_{max}/\delta_{max}} \right)^{1/2} \cdot (v_c \times n_c) \times n_c$	[36-40]
Walton and Braun's model	$f_n = \begin{cases} -k_1 \delta_n n_c, \dot{\delta}_n \geq 0 \\ \text{(loading)} \\ -k_2 (\delta_n - \delta_{n0}) n_c, \dot{\delta}_n < 0 \\ \text{(unloading)} \end{cases}$	$f_t = \begin{cases} f_t' + k_t^0 \left(1 - \frac{f_t - f_t^*}{\mu f_n - f_t^*} \right)^{\frac{1}{3}} \Delta v_c^t \\ \text{if } \dot{v}_c^t \text{ in initial direction} \\ f_t' + k_t^0 \left(1 - \frac{f_t^* - f_t}{\mu f_n + f_t^*} \right)^{\frac{1}{3}} \Delta v_c^t \\ \text{if } \dot{v}_c^t \text{ in opposite direction} \end{cases}$	[41, 42]
Where $f_t = f_t , f_n = f_n $			
Torque Models	Rolling friction torque	Torque from tangential forces	References
Method 1	$m_r = -k_r \theta_r - C_r d\theta_r/dt$	$m_t = R \times f_t$	[39, 40, 43, 44]
Method 2	$m_r = -\min\{\mu_r f_n , \mu_r' \omega_n \} \hat{\omega}_n$		

Particles continuously interact with the surrounding fluid generating various forces. One such force is the buoyancy force. However, the main particle-fluid interaction force is the drag force which is the driving force of fluidization. A number of particle-fluid interaction forces have been implemented in DEM approaches, such as the drag force, the pressure gradient force and other unsteady forces like the virtual mass force, the Basset force and lift forces that have been studied by Li et al. [45], Xiong et al. [46] and Potic et al. [47] [34].

Newton's equation can be used to determine the drag resistance force acting on an isolated particle in a fluid. There are three different regions in a particle-fluid system: the Stoke's law's region, the transition region, and the Newton's law region. These regions are characterized by different Reynold's numbers, Re . By knowing the Reynold's number the particle-fluid drag coefficient can be calculated [34]. But in a particulate system, the presence of other particles reduces the space for fluid and generates a sharp fluid velocity gradient, making the problem much more complicated [34].

Two general methods have been presented by Ergun [48] and Wen and Yu [49] for the bed pressure drop. Richardson [50] presented the bed expansion experiment. The effect of the presence of other particles is considered in terms of local porosity and is also related to flow regimes. Such work has e.g. been done by Di Felice [51]. The other method is based on numerical simulations at a microscale. Techniques used include direct numerical simulation (DNS) [52]. Both methods are summarized in Table 1.4 [34].

Table 1.4: Particle-fluid interaction forces

Forces	Correlations	References
Drag force	<p>For an isolated particle moving through a gas,</p> $F_d = C_d \pi \rho_f d_p^2 u - v (u - v) / 8$ <p>Effect of surrounding particles is described by a voidage function, $f(\varepsilon_f)$:</p> $F_d = f(\varepsilon_f) C_d \pi \rho_f d_p^2 u - v (u - v) / 8$ $C_d = \frac{24(1 + 0.15 Re_p^{0.687})}{Re_p} \quad (Re_p < 1000)$ $C_d = 0.44 \quad (Re_p > 1000), Re_p = \rho_f d_p \varepsilon_f u - v / \mu_f$	
Pressure gradient force	$F_p = -V_p dp/dx = -V_p (\rho_f g + \rho_f u du/dx)$ <p>It is of general validity and all relevant contributions are included when dp/dx is evaluated from the fluid equation of motion</p>	[53]
Virtual mass force	$F_{Vm} = C_{Vm} \rho_f V_p (\dot{u} - \dot{v}) / 2$ $C_{Vm} = 2.1 - 0.132 / (0.12 + A_c^2)$ $A_c = (u - v)^2 / (d_p d(u - v) / dt)$	[54, 55]
Basset force	$F_{Basset} = \frac{3}{2} d_p^2 \sqrt{\pi \rho_f \mu_f} \left[\int_0^t \frac{(\dot{u} - \dot{v})}{\sqrt{t - t'}} dt' + \frac{(u - v)_0}{\sqrt{t}} \right]$ <p>Where $(u - v)_0$ is the initial velocity difference</p>	[56, 57]
Saffman force	$F_{Saff} = 1.61 d_p^2 (\mu_f \rho_f)^{1/2} \omega_c ^{-1/2} [(u - v) \times \omega_c]$ $\omega_c = \nabla \times u$	[58, 59]
Magnus force	$F_{Mag} = \frac{\pi}{8} d_p^2 \rho_f \left[\left(\frac{1}{2} \nabla \times u - \omega_d \right) \times (u - v) \right]$ <p>Where $\frac{1}{2} \nabla \times u$ is the local fluid rotation and ω_d is the particle rotation. One notes that the lift would be zero if the particle rotation is equal to the location rotation of the fluid</p>	[60]

1.3.1 A model for the fluid phase

The deviation of the pressure below a granular bed of thickness h from ambient pressure is given by [61]:

$$\Delta p = -h\gamma\rho_a(1 - \emptyset)v_a \quad (1.6)$$

where γ describes the grain–air coupling introduced by the use of Darcy’s law, ρ_a is the air density, \emptyset is the bed porosity, and v_a is the air velocity. Darcy’s flow is observed for $0.3 < Re \leq 0.7$ [62], where the Darcian Reynolds number is defined as $Re = \rho_a v_a d_p / \mu_a$ and μ_a is the air dynamic viscosity. The physical properties of air are given in Table 2.1.

The flow Reynolds number in the experiments described in the preceding section is much larger than 0.7. Hence, the flow regime was probably turbulent [63]. The granular bed Reynolds number, used as the demarcation criterion, is defined as

$$Re_{slip} = \rho_a |v_a - v_p^i| d_p / \mu_a \quad (1.7)$$

where v_p^i is the velocity of the i^{th} particle.

In this work, an attempt was made to combine the Lagrangian (particle-based) model and LES [64] to achieve more accurate simulations of the tilting and, especially, the swirling granular flows. The filtered continuity momentum for an isothermal 3D flow of air is

$$\frac{\partial \bar{\rho}}{\partial t} + \nabla \cdot (\bar{\rho} \tilde{V}_a) = 0 \quad (1.8)$$

$$\frac{\partial \bar{\rho} \tilde{V}_a}{\partial t} + \nabla \cdot (\bar{\rho} \tilde{V}_a \tilde{V}_a) = -\frac{1}{\rho_a} \nabla (\bar{\rho} \bar{p}) + \frac{1}{\rho_a} \nabla \cdot (\bar{\rho} \tilde{\sigma}) + \nabla \cdot \tau + \bar{f}_{pf} + \bar{\rho} g \quad (1.9)$$

where $\bar{\rho}$ is the filtered density, defined as $\bar{\rho} = \rho_a \bar{\emptyset}$; \tilde{V}_a is the density weighted Favre filter velocity, defined as $\tilde{V}_a = \bar{\rho} \bar{V}_a / \bar{\rho}$; and \bar{p} is the filtered pressure at the supergrid scale. The forces exerted by the fluid on the particles per unit volume, \bar{f}_{pf} , encompass the drag, lifts, added mass, stress, and Basset history forces [65]; g is the acceleration of gravity.

The viscous stress tensor in Equation (1.9) is defined as

$$\sigma = -\frac{2}{3} \mu_a \nabla \cdot V_a I + \mu_a (\nabla V_a + (\nabla V_a)^T) \quad (1.10)$$

where I is the second-order identity tensor.

In Equation (1.9), τ is the subgrid scale (SGS) stress tensor,

$$\tau = -\bar{\rho} (\tilde{V}_a \tilde{V}_a - \tilde{V}_a \tilde{V}_a) - \bar{\rho} (\widetilde{V_a'' V_a} + \widetilde{V_a V_a''}) - \bar{\rho} (\widetilde{V_a'' V_a''}) \quad (1.11)$$

where V_a'' represents the subgrid-scale part of V_a based on Favre filtering.

The SGS stress tensor, τ , is required to close the equations for the large scale fields on a grid small enough (but much larger than the Kolmogorov scale) to provide reasonable resolutions. In contrast to the filtered single-phase equations, a conceptual restriction arising from the present approach is that the filter width, Δ , should be larger than the length

scale characteristic of the bubble phase. Thus, an appropriate choice of Δ should provide a sufficiently large-scale resolution without violating this restriction.

The particles make a contribution to the process of energy removal from the resolved scales of the fluid phase. This two-way coupling effect may be modeled by superposing particle-induced and shear-induced SGS energy dissipations. A tentative first attempt at closure of the momentum Equation (1.9) with an SGS model for τ is:

$$\tau_{mod} = -\bar{\rho}(\widetilde{u_f u_f} - \widetilde{u_f} \widetilde{u_f}) + \left[2(C_s \Delta)^2 \bar{\rho}(\tilde{S} : \tilde{S})^{1/2} + (C_s \Delta) \bar{\rho}(|\widetilde{V_{slip}}|) \right] \left(\tilde{S} - \frac{1}{3} tr \tilde{S} I \right) \quad (1.12)$$

where C_s is the Smagorinsky constant,

$$C_s = 2 \prod / 3\sqrt{3} \left(-\frac{R(1 + C_{b0}R^2)}{K^3} \right)^{1/2} \quad (1.13)$$

R is related to the ratio of the mesh spacing to the Kolmogorov length scale (so that $R = -1 + (\Delta)^{4/3}$), K is the Kolmogorov constant, C_{b0} is the backscatter parameter, which is set to $C_{b0} = 0.2$, \tilde{S} is the resolved rate of strain tensor, and V_{slip} represents the slip velocity.

Drying model

Mezhericher [25] presented particle drying as a two-stage process as shown in Figure 1-15.

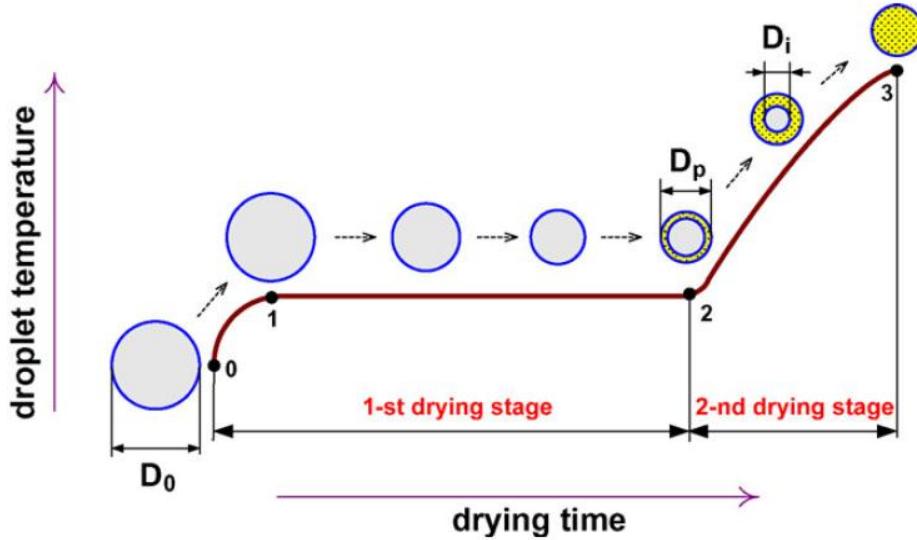


Figure 1-15: Two-stage drying of droplets containing solids

In the first stage, the liquid content of the droplets starts to evaporate. This results in shrinkage of the droplet diameter. In the second stage, the particles can be identified to have a dry crust and a wet core. As a result of further drying, the wet core shrinks and the crust thickens. This process continues until the moisture of the particle reaches the minimal possible value [25].

In the first drying stage, assuming a uniform distribution of the droplet's temperature the corresponding energy conservation equation is given by:

$$h_{fg}\dot{m}_v + c_{p,d}m_d \frac{dT_d}{dt} = h(T_g - T_d)4\pi R_d^2 \quad (1.14)$$

The coefficient of heat transfer, h , is calculated as the sum of convection and radiation heat transfer coefficients: $h = h_c + h_r$.

The rate of change of droplet diameter is determined as:

$$\frac{dR_d}{dt} = -\frac{1}{\rho_{d,w}4\pi(R_d)^2}\dot{m}_v \quad (1.15)$$

The mass transformation of the droplet surface can be calculated by using the law of mass convection:

$$\dot{m}_v = h_D(\rho_{v,s} - \rho_{v,\infty})4\pi(R_d)^2 \quad (1.16)$$

The convective heat and mass transfer coefficients, h_c and h_D , are evaluated in terms of the Ranz-Marshall correlation as [66]:

$$Nu_d = (2 + 0.6Re_d^{1/2}Pr^{1/3})(1 + B)^{-0.7} \quad (1.17)$$

$$Sh_d = (2 + 0.6Re_d^{1/2}Sc^{1/3})(1 + B)^{-0.7} \quad (1.18)$$

By integration from Eq. (1.15) the droplet's mass can be found as:

$$m_d = m_{d,0} - \frac{8}{6}\pi\rho_{d,w}\left[(R_{d,0})^3 - (R_d)^3\right] \quad (1.19)$$

Finally, the value of droplet moisture content on dry basis, X_d , is given by:

$$X_d = \frac{m_{d,w}}{m_{d,s}} = \frac{m_d}{m_{d,0}}(1 + X_{d,0}) - 1 \quad (1.20)$$

In the second drying stage, Mezhericher [25] considered a wet particle as a sphere with isotropic physical properties and a temperature-independent crust thermal conductivity. The equations for the energy conservation for the wet core and the crust are as follows:

$$\rho_{wc}c_{p,wc}\frac{\partial T_{wc}}{\partial t} = \frac{1}{r^2}\frac{\partial}{\partial r}\left(k_{wc}r^2\frac{\partial T_{wc}}{\partial r}\right), \quad 0 \leq r \leq R_i(t) \quad (1.21)$$

$$\frac{\partial T_c}{\partial t} = \frac{\alpha_c}{r^2}\frac{\partial}{\partial r}\left(r^2\frac{\partial T_c}{\partial r}\right), \quad R_i(t) \leq r \leq R_p \quad (1.22)$$

The boundary conditions for the above set of equations are:

$$\begin{cases} \frac{\partial T_{wc}}{\partial r} = 0, & r = 0; \\ T_{wc} = T_c, & r = R_i(t); \\ k_c \frac{\partial T_c}{\partial r} = k_{wc} \frac{\partial T_{wc}}{\partial r} + h_{fg} \frac{\dot{m}_v}{A_i}, & r = R_i(t); \\ h(T_g - T_c) = k_c \frac{\partial T_c}{\partial r}, & r = R_p; \end{cases} \quad (1.23)$$

The rate of recession of the crust–wet core interface is calculated as follows:

$$\frac{d(R_i)}{dt} = -\frac{1}{\varepsilon \rho_{wc,w} 4\pi R_i^2} \dot{m}_v \quad (1.24)$$

The total mass transfer rate through the crust pores is:

$$\dot{m}_v = \dot{m}_{v,diff} + \dot{m}_{v,flow} = h_D(\rho_{v,s} - \rho_{v,\infty})A_p \quad (1.25)$$

The mass flow rate of vapor diffusion is defined by:

$$\dot{m}_{v,diff} = \frac{8\pi \varepsilon^\beta D_{v,c} M_w R_p R_i}{R(T_{c,s} + T_{wc,s})(p_m - p_v)} \left(p_v \frac{\partial p_m}{\partial r} - p_m \frac{\partial p_v}{\partial r} \right) \quad (1.26)$$

The mass flow rate of forced vapor flow is determined as follows:

$$\dot{m}_{v,flow} = -\frac{B_k}{\mu_m} \frac{8\pi R_p R_i M_m p_m}{R(T_{c,s} + T_{wc,s})} \frac{\partial p_m}{\partial r} \quad (1.27)$$

The permeability, B_k , is calculated according to Carman-Kozeny equation:

$$B_k = \frac{d_p^2 \varepsilon^3}{180(1 - \varepsilon)^2} \quad (1.28)$$

The particle mass can be calculated as:

$$m_p = \frac{m_{d,0}}{(1 + X_{d,0})} \left(1 - \frac{\rho_{wc,w}}{\rho_{wc,s}} \right) + \frac{4}{3} \pi \rho_{wc,w} [\varepsilon R_i^3 + (1 - \varepsilon) R_p^3] \quad (1.29)$$

Finally, the particle moisture content is given by:

$$X_p = \frac{m_w}{m_s} = \frac{m_p}{m_{d,0}} (1 + X_{d,0}) - 1 \quad (1.30)$$

Mezhericher [29] solved this problem as a 2D symmetric problem and reported CFD results for particle surface temperature as shown in Figure 1-16.

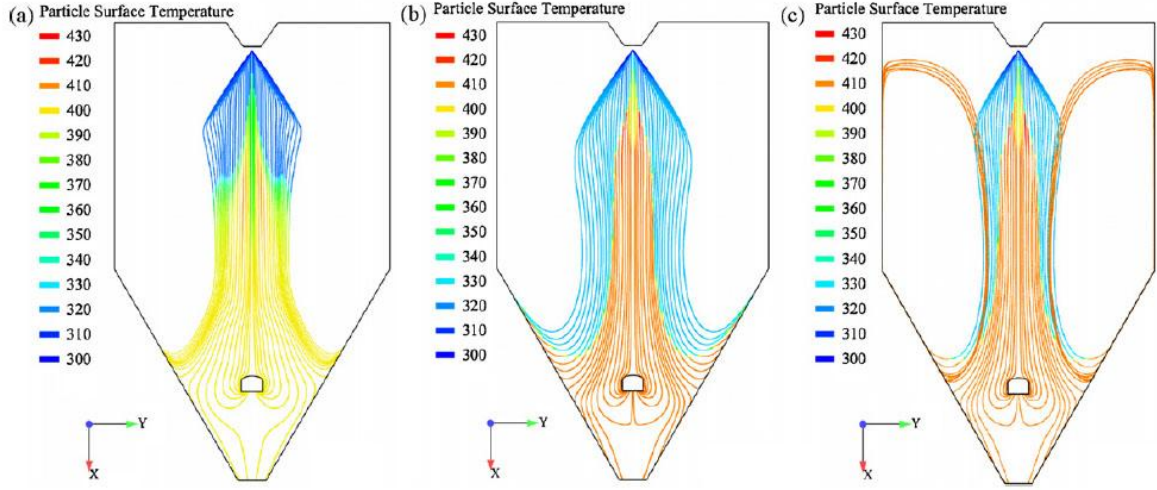


Figure 1-16: Particle traces colored by particle surface temperature (in K).

Considering all three phases as well as all particle contacts, the particle concentration can be calculated. Mezhericher [67] reported the particle concentration by considering particle-particle and droplet-droplet interactions, see Figure 1-17 (a), and droplet-droplet interactions only, see Figure 1-17 (b). The difference between two models can be seen in Figure 1-17(c).

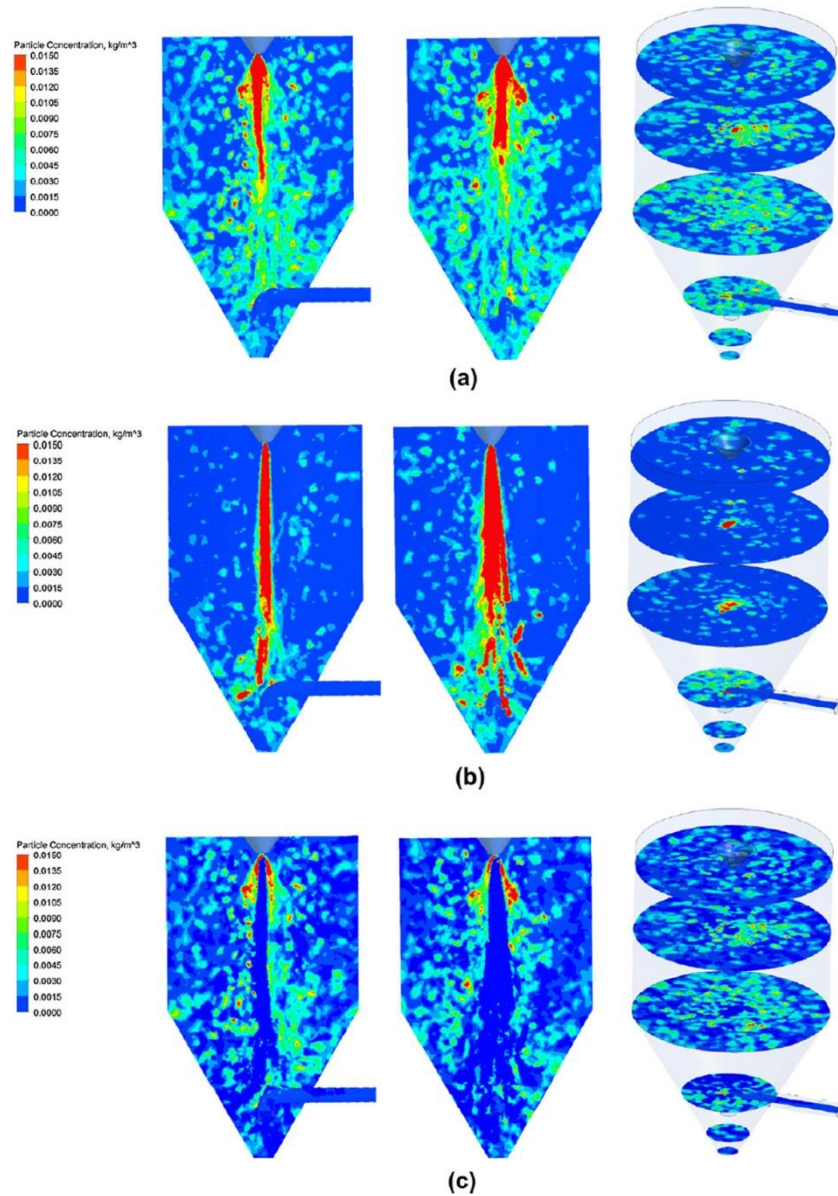


Figure 1-17: Three-dimensional contours of particle concentration at $t = 30$ s. (a) DD + PP model, (b) DD model built in ANSYS FLUENT solver, (c) the difference between the two model predictions. Left – XZ cut, middle – YZ cut, right – isometric view.

1.3.2 Separation of the dry product from the exiting air

The last step in the spray-drying process is the separation of the dry product from the exiting air; this step takes place in a cyclone separator. This is a device which performs centrifugal separation of materials in a fluid flow [68].

This type of separators is one of the most elegant and also most widely used of separators. It is a device with no moving parts, therefore requiring virtually no maintenance. It enables micrometer-sized particles to be separated from a moving gas without a substantial pressure-drop (Figure 1-18) [60].

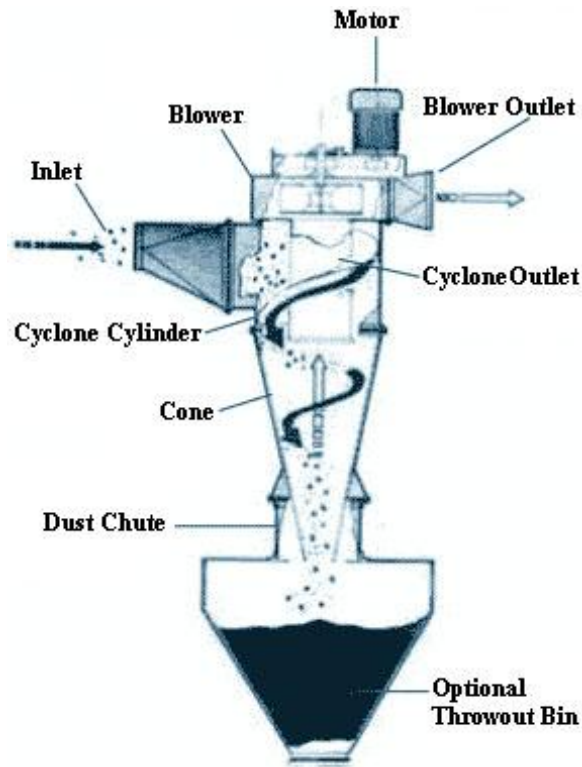


Figure 1-18: A cyclone collector

The cyclone utilizes the fluid pressure gradient to create rotational fluid motion. This rotational motion causes the dispersed phase to separate relatively fast due to the strong forces acting. In the widely used cylinder-on-cone type of cyclone with reverse flow, the gas spirals down from a tangential inlet towards the apex of a conical section, where the flow is reversed, upon which the particles separate and are collected in a hopper. The continuous phase then proceeds upward in an inner core flow towards the gas exit via the vortex finder [69].

Chu [70] presented a numerical solution of DEM for a cyclone collector with geometry as shown in Figure 1-19.

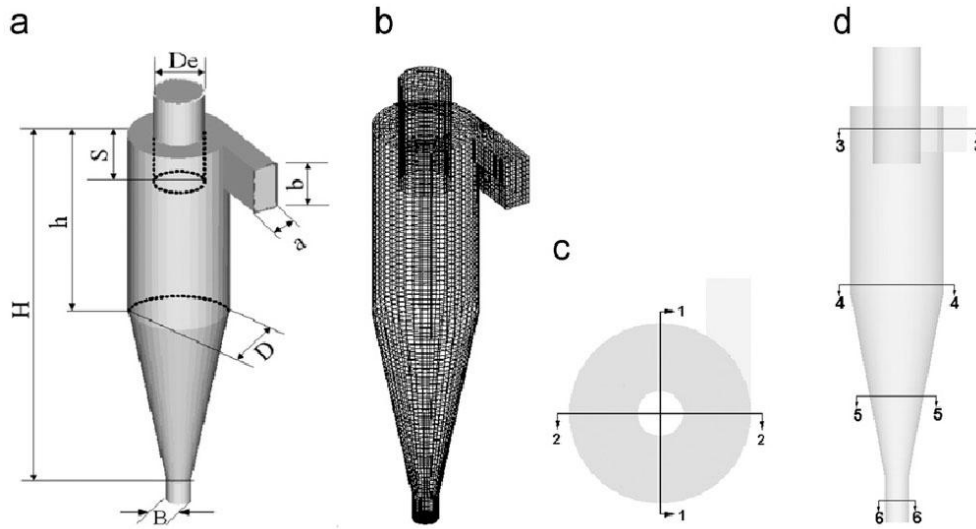
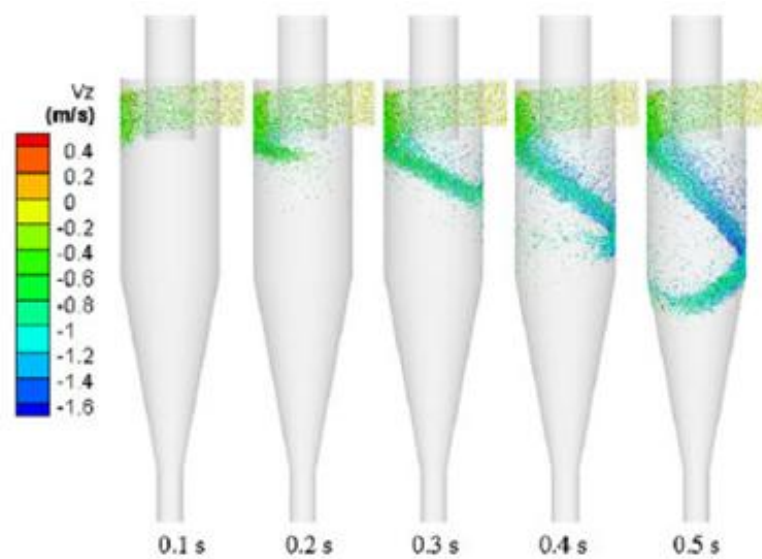


Figure 1-19: A schematic and grid representation of the cyclone considered, together with the definition of the sections: (a) 3D view of geometry; (b) 3D view of CFD grids; (c) top view of the sections; and (d) front view of the sections.

Chu [70] reported the results of running this model, see Figure 1-20 for particle velocities in the z direction. Bhasker [71] modeled a cyclone collector of industrial size.



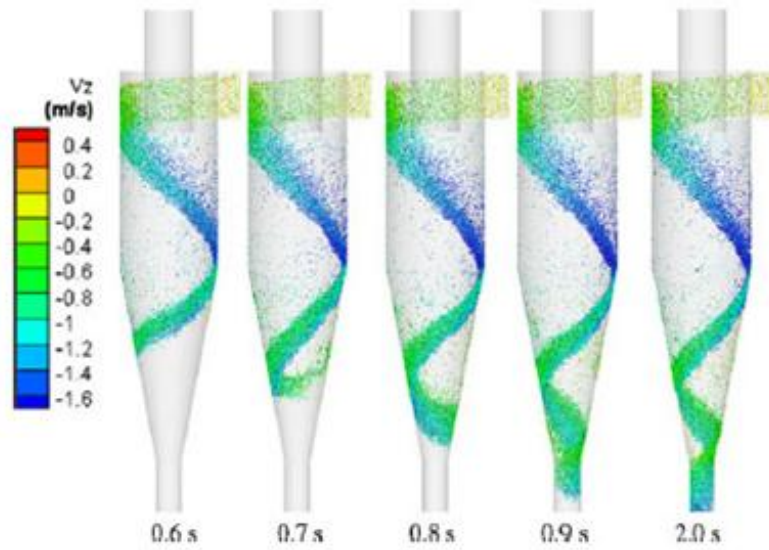


Figure 1-20: Snapshots showing the flow of particles in a cyclone with solid loading ratio 2.5 (colors signify particle velocity in the z direction)

As is easily observed from Figure 1-20, after some time the particles settle down in the throw out bin.

1.4 Dense granular materials

Granular materials are abundant in nature and their response to vibration plays an important role in natural events such as earthquakes [6] and avalanches [7]. Grains are vibrated as part of many industrial processes such as drying, powder mixing, and separation [5]. Horizontal vibration, used in applications such as vibrating screens, has been the topic of a number of studies [72]. One study, involving a bed of grains immersed in a fluid in a horizontal container and subjected to horizontal vibrations, reported a wealth of phenomena, including solid–fluid granular transitions with hysteresis that disappeared in the presence of a modest vertical air flow corresponding to approximately 40% of the weight of the bed [73]. Rubin, Goldenson, and Voth [74] used optical particle tracking [75] to measure a granular slope under horizontal vibration and observed that the beads underwent intermittent motion, indicating that micro-rearrangements affected the failure of slopes under external perturbations. A horizontal granular bed becomes unstable at the peak acceleration relative to gravity, Γ , by acquiring a tilt [76]. Aumaitre et al. [75] studied the onset and dynamics of flow in shallow, horizontally oscillating granular layers as a function of the depth of the layer and imposed acceleration. They found that the thresholds for starting and stopping the flow of avalanches in inclined layers were slightly different. At Γ , the motion was fluid-like over the entire cycle. The measured flow profiles had time-dependent shapes that differed significantly from previously measured avalanche flow profiles. The dynamics and stability of a bed composed of solid particles immersed in a fluid was analyzed by Anderson and Jackson [53]. Their treatment may be more suitable for modeling continuous flows [77]. The transition between intermittent and continuous flows is better predicted by combining Lagrangian (particle-based) and Eulerian (grid-based) methods (Eu/La). This approach uses large-eddy simulation (LES) to include gas

dynamics [78]. The dynamics of grains is described by molecular dynamics, where the interaction between the grain surfaces is modeled by the generalized form of contact theory developed by Hertz [79]. In addition, the coefficient of kinetic friction is assumed to depend on the relative velocity of slipping [80].

The current study reports the formation of tilts in shaken granular materials in a rectangular container that was vibrated horizontally according to

$$r = A_x \sin(\omega_x t) e_x + A_y \cos(\omega_y t) e_y \quad (1.31)$$

Two hollow cylindrical vessels were mounted vertically in the container. Unique swirling granular flows were observed in the cylinders, with grains cascading down the surface of the piles outside the cylinders. Numerical simulations were performed to investigate these complex granular flows.

2 Materials and methods

2.1 Experimental setup

This study used a polycarbonate plastic container, shown together with the pertinent nomenclature in Figure 2.1 (a) and (b). The container was filled with sand and attached to the center of a thin cardboard sheet that was clipped to the bottom of the rectangular pad of an orbital shaker. The physical and mechanical properties of polycarbonate plastics are given in Table 2.1. Orbital shakers are widely used in the pharmaceutical industry to mix liquids in biopharmaceutical processes [81]; they are also commonly used to study the aggregation and breakup of microorganisms and inorganic particle flows in water [82].

Table 2.1 Material properties [83, 84]

Material	Property	Symbol	Value
Polycarbonate	Density	ρ_P	1.20-1.22 g/cm ³
	Young's modulus	E	2.0-2.4 GPa
	Tensile strength	σ_t	55-75 MPa
	Poisson's ratio	ν	0.37
	Coefficient of friction	μ	0.31
Glass	Elastic modulus	E	$6.3 \times 10^{10} \text{ Pa}$
	Density	ρ_P	2390 kg/m^3
	Poisson's ratio	ν	0.244
	Instantaneous shear modulus	G_0	$2.53 \times 10^{10} \text{ kg/ms}$
	Long time shear modulus	G_∞	$6.1 \times 10^9 \text{ kg/ms}$
Air	Density	ρ_g	1.225 kg/m^3
	Kinematics Viscosity	ν_g	$1.7894 \times 10^{-5} \text{ kg/ms}$
	Temperature	T_g	293 K
Sand	Poisson's ratio	ν	0.17
	Density	ρ_g	2.203 g/cm^3
	Bulk modulus	K	37 GPa
	Young's modulus	E	71.7 GPa
Foam	Poisson's ratio	ν	0.1
	Density	ρ_g	1.05 g/cm^3
	Young's modulus	E	3000 MPa

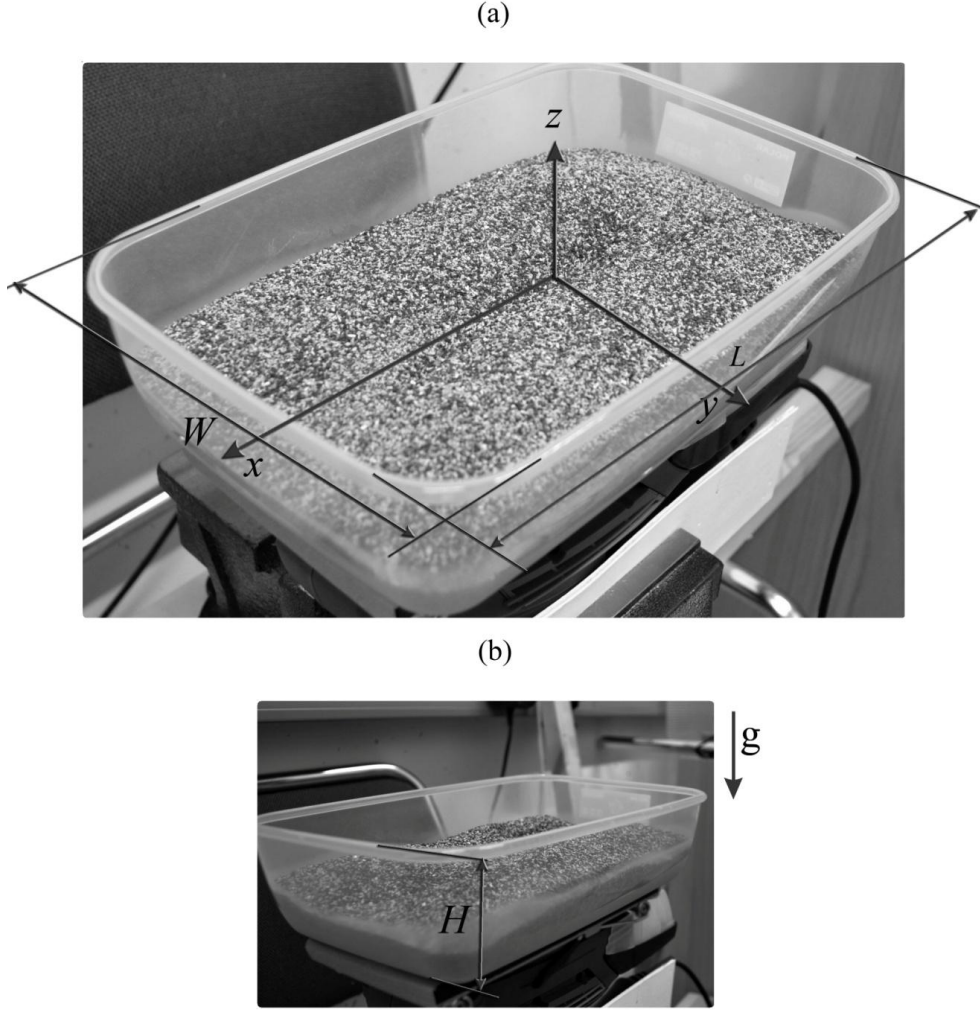


Figure 2.1: (a and b) Images of the container and nomenclature. The dimensions of the container are $W = 18$ cm, $L = 28$ cm, and $H = 7$ cm.

A function generator was used to deliver a sinusoidal signal of adjustable frequency and amplitude to a power amplifier, and then transmitted as the input signal to the orbital shaker. The accelerations in the x- and y-directions were monitored with a 3-axis accelerometer attached to the pad. A data acquisition system collected the acceleration data from the accelerometer and transferred them via a USB link to a computer for analysis.

The shaker pad underwent horizontal oscillations with the form given in Equation (1.31). Figure 2.2 depicts the ellipse-type orbits that resulted when an offset weight was placed on the motor shaft of the shaker at ($\omega_x/2 = 42$ Hz and $A_x = 10^{-3}$ m) and ($\omega_y/2 = 25$ Hz and $A_y = 10^{-3}$ m) corresponding to the values of $\Gamma_x = 7.1$ and $\Gamma_y = 2.5$, respectively. It was possible to operate the shaker at different angular speeds.

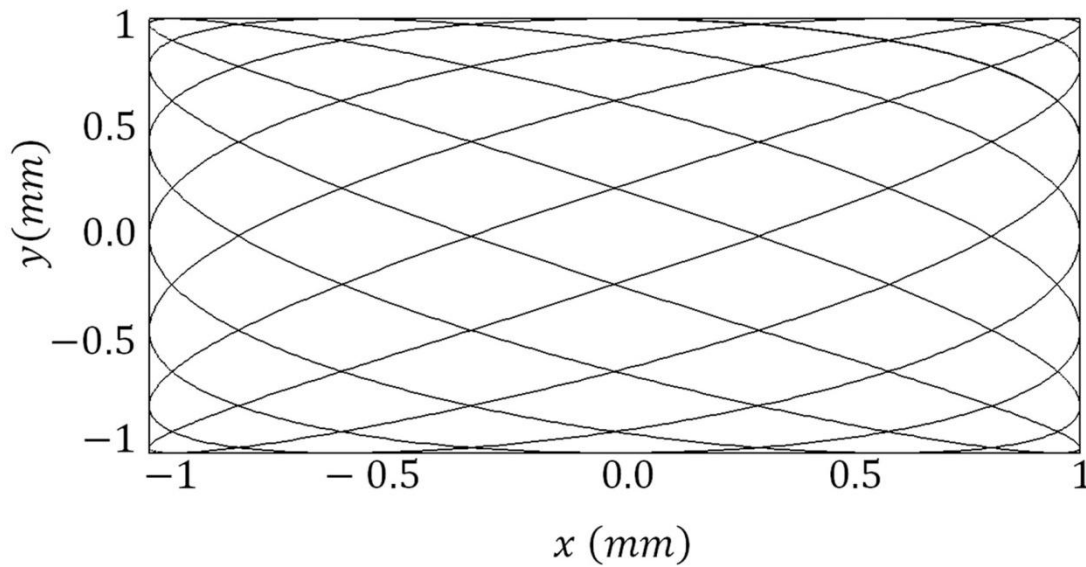


Figure 2.2 The ellipse-type orbits of the shaker.

2.2 Measurement of acceleration

An accelerometer is a sensor that measures the physical acceleration experienced by an object due to inertial forces or mechanical excitation [85].

Traditionally, accelerometers have been used first and foremost in aircraft, but also in dynamometers and bridges. Today's advanced technology has introduced new devices, smart phones, computer hard disk drives and automobile airbag systems that all use accelerometers to perform their specific tasks [86].

There are various types of accelerometers, such as:

- Capacitive spring mass base (separate seismic masses)
- DC response
- Electromechanical servo (servo force balance)
- High gravity
- High temperature
- Low frequency
- Magnetic induction
- Strain gauge
- Surface acoustic wave (SAW)
- Surface micro machined capacitive (MEMS¹ [87])
- Thermal (sub micrometer CMOS process)

¹ MEMS technology is based on a number of tools and methodologies which are used to form small structures with dimensions on the micrometer scale. Significant parts of the technology have been adopted from integrated circuit (IC) technology. For instance, almost all devices are built on wafers of silicon, like ICs. The structures are realized in thin films of materials, like ICs. They are patterned using photolithographic methods, like ICs. There are however several processes that are not derived from IC technology.

In this section the design principles of two different types will be briefly described.

- **Thermal**

Thermal accelerometers are designed to eliminate the need for proof masses to improve reliability. The limitation of thermal accelerometers is their low-frequency response [88-90].

The working principle of thermal accelerometers is based on free convection heat transfer inside the system [90]. Figure 2.3 presents a schematic diagram of a thermal accelerometer. It is an enclosed system containing a heater and temperature sensors that uses air as a working fluid [91].

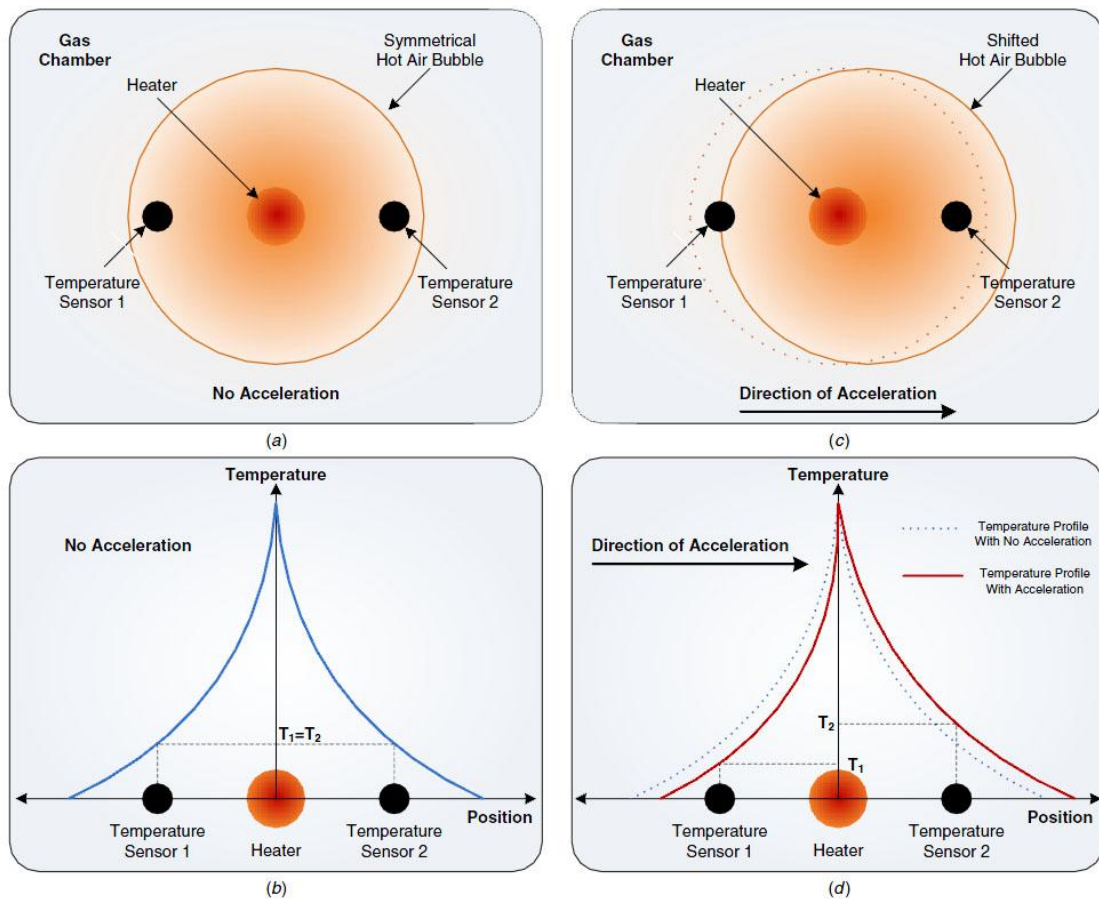


Figure 2.3 Differential temperature sensing inside a closed chamber: (a) hot air bubble experiencing no acceleration, (b) no temperature difference sensed at zero acceleration, (c) a hot air bubble shifted due to acceleration, and (d) a temperature difference sensed due to acceleration [92].

A central heater reduces the density of the surrounding fluid and creates a hot bubble. The working principle for this type of accelerometers is measuring the bubble's movement.

Single-axis thermal accelerometers use two temperature sensors equidistant from the heater [92].

As illustrated in Figure 2.3 (a) in the case of no acceleration, the hot bubble is symmetrical about the heater. Therefore, as can be observed from Figure 2.3 (b), the two temperature sensors detect no temperature difference. In the other case (apply acceleration in the direction of the accelerometer's sensitivity direction) the hot bubble's symmetry is disturbed (Figure 2.3(c)). As illustrated in Figure 2.3(d), two sensors detect a temperature difference and produce an output proportional to the magnitude and direction of the applied acceleration. This temperature difference produces a voltage difference, referred to as the Seebeck voltage, δV , proportional to the temperature difference, δT , between two sensors:

$$\delta V = \alpha \delta T. \quad (2.1)$$

The constant of proportionality, α , is the Seebeck coefficient, usually specified as $\mu V^\circ C^{-1}$. The sensitivity of a thermal accelerometer is defined as the ratio of the output voltage to the acceleration applied to the system. In this system there is only convection heat transfer and natural convection governed by the Grashof number, Gr . Leung [91] established that the sensitivity of a thermal accelerometer is linearly proportional to the Grashof number:

$$Gr = \frac{a \rho^2 x^3 \beta \Delta T}{\mu^2} \quad (2.2)$$

Eq. (2.2) shows that the sensitivity of a thermal accelerometer can be improved significantly without changing the device design just by using a high-density fluid. [91]

- **Separate Seismic Masses**

There have been a few three-axes accelerometer designs based on four separate seismic masses, each one suspended on a slanted beam, giving identical resolution and frequency response in all directions [93, 94]. This type is the simplest one that can be used to describe the principles.

By exchanging the beam with a spring and damper, the accelerometer working principle can be easily explained by a mass-spring-damper system in a case. The acceleration applied to the case causes the mass to move, and this motion can be used to determine the magnitude of the acceleration.

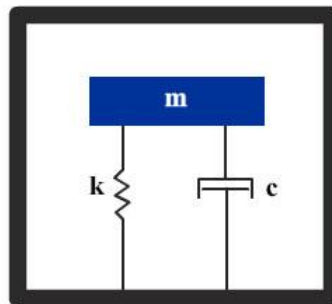


Figure 2.4 Mass-spring damper system

The mass used in accelerometers is often called the seismic-mass or proof-mass [95].

By considering all forces in the z direction:

$$F_{applied} - F_{spring} - F_{damp} = m\ddot{z} \quad (2.3)$$

$$m\ddot{z} + F_{spring} + F_{damp} = F_{applied} \quad (2.4)$$

$$m\ddot{z} + kz + c\dot{z} = F \quad (2.5)$$

Equation (2.5) is a second order linear differential equation with constant coefficients. The general solution $Z(t)$ is the sum of the complementary function $Z_c(t)$ and the particular integral $Z_p(t)$ [96]:

$$Z = Z_c(t) + Z_p(t) \quad (2.6)$$

The complementary function satisfies the homogeneous equation

$$m\ddot{z} + kz + c\dot{z} = 0 \quad (2.7)$$

The solution for $Z_c(t)$ is:

$$Z_c(t) = Ce^{st} \quad (2.8)$$

Substituting equation (2.8) in equation (2.7) gives:

$$(ms^2 + cs + k)Ce^{st} = 0 \quad (2.9)$$

Ce^{st} cannot be zero for any value of t . Then equating the rest of the equation to zero, the two solutions for s are:

$$s_{1,2} = \frac{1}{2}m(-C \pm \sqrt{C^2 - 4mk}) \quad (2.10)$$

From this equation, the following identities can be derived:

$$\omega_n = \sqrt{\frac{k}{m}} \quad (2.11)$$

$$\frac{c}{m} = 2\zeta\omega_n \quad (2.12)$$

$$\zeta = c/2\sqrt{km} \quad (2.13)$$

• Steady state performance

In the steady state condition, i.e., with the excitation acceleration amplitude ‘ a ’ and frequency ‘ ω ’, the amplitude of the response is constant and is a function of the excitation amplitude and frequency ‘ ω ’. Thus for the static response $\omega = 0$, the deflection amplitude Z is:

$$Z = Z_0 = \frac{F}{k} \quad (2.14)$$

$$Z = ma/k \quad (2.15)$$

Here the sensitivity S of an accelerometer is defined as:

$$S = Z/a = m/k \quad (2.16)$$

- **Dynamic performance**

In order to obtain the dynamic performance, it is easier to consider the Laplace transform of Eq. (2.5):

$$\frac{Z(s)}{a(s)} = \frac{1}{s^2 + \frac{c}{m}s + \frac{k}{m}} \quad (2.17)$$

It can be seen by comparing Eqs. (2.11) and (2.16) that the bandwidth of an accelerometer sensing element has to be traded off with its sensitivity since $S \propto 1/\omega_n^2$.

In this section only the basic calculations will be presented. More elaborate calculations can be found in Rodjegård et al. [97], based on their design of accelerometers using four separate seismic masses, see Figure 2.5.

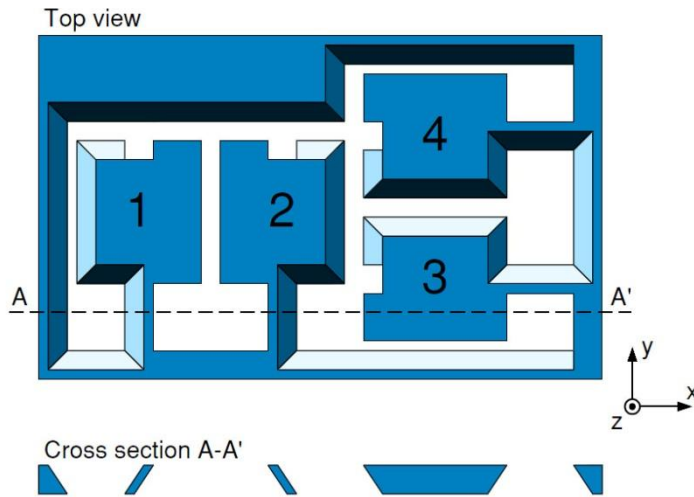


Figure 2.5: Top and cross-sectional views illustrating the triple-axis detection principle. The four seismic masses are suspended from thin beams oriented in different {1 1 1} planes.

The geometric parameters of this design are presented in Table 2.2, referring to Figure 2.6.

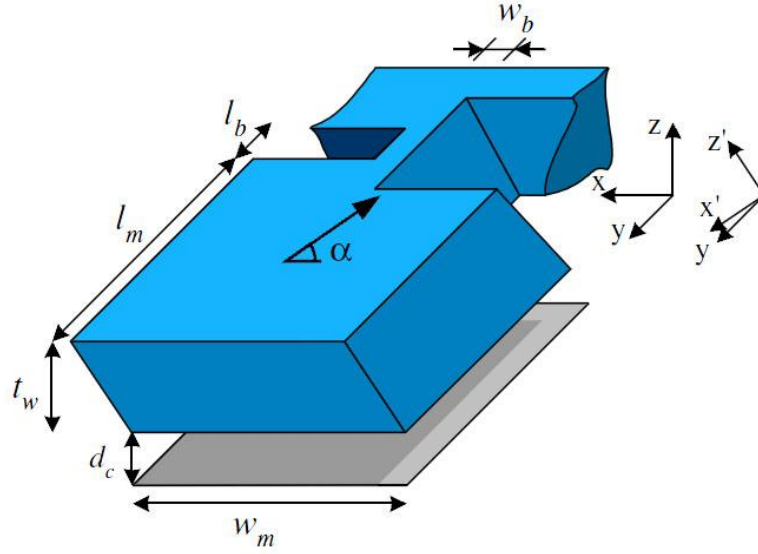


Figure 2.6: A single sensing element with a capacitor plate for read-out. A local coordinate system, x' , y' and z' , oriented along the $\{1\ 1\ 1\}$ plane of the crystal, is used for the analytical model.

Table 2.2: Geometrical parameters of the accelerometer design

Wafer thickness	t_w	300 μm
Seismic mass width	w_m	1.5 mm
Seismic mass length	l_m	1.5 mm
Beam width (top projection)	w_b	80 μm
Beam length	l_b	1.35 mm
Readout electrode/ gas film gap	d_c	3.1 μm
Packaging pressure	P_a	10 mbar

This study used an accelerometer of the type ADXL345, manufactured by ANALOG DEVICES. It is a small, thin, ultralow-power, three-axis accelerometer with high resolution (13-bit) measurement covering up to $\pm 16\text{ g}$ [85]. The ADXL345 is a surface micro machined accelerometer [98] which uses the principle described above with a different mass configuration. A simple design of this type is shown in Figure 2.7 [99].

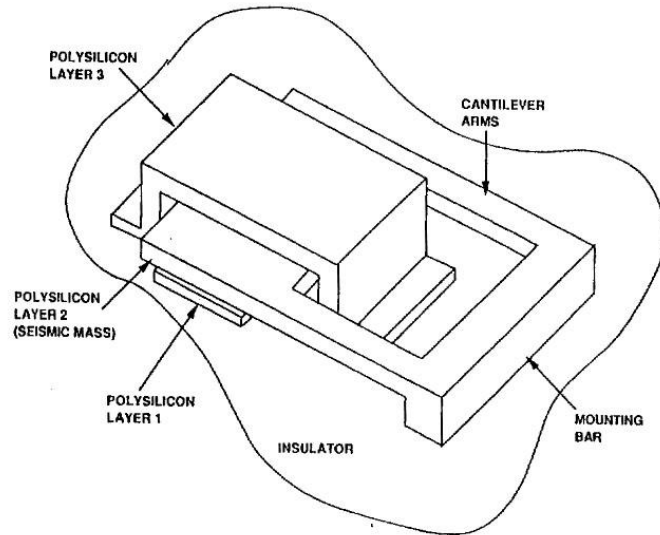


Figure 2.7: A schematic view of a surface micromachined polysilicon accelerometer

The data obtained from the accelerometer was analyzed with Matlab and the motion pattern of the orbital shaker was used for simulating the system. The accelerometer firmware used was a full resolution (13 bit) version with a 800 Hz sampling time setting. In order to reduce the noise sensed by the accelerometer, the data was analyzed after running the system for 30 s and also the average of every 100 data values was used to plot the acceleration diagrams.

A set of collected data is presented in Table 2.3. The unit used for the acceleration is LSB (Least Significant Bit) which can be converted to mg by multiplying by 31.2 [85].

The software LabView was used for monitoring the acceleration.

Table 2.3: A set of data collected from the accelerometer

X	Y	Z
-1568	895	-1115
2797	768	1464
2153	-2311	-817
-1297	-289	-1577
-44	1632	641
2584	-992	70
1020	-1606	-649
-2023	195	-1578
1755	1618	1848
2645	-2228	-517
-508	-974	-1436
-1133	774	-343
2460	317	1225
1911	-2060	-710
-1741	-154	-1638

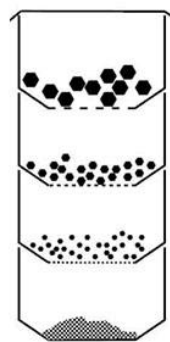
281	2108	1291
2593	-1372	182
719	-1473	-719
-2057	530	-1515
2017	1541	1989
2532	-2293	-705
-797	-970	-1513
-1213	1144	-322
2619	330	1341

2.3 Particle size distribution (PSD)

One of the important parameters of two-phase flow is particle size [68]. Particle size distributions are divided into two types: discrete and continuous [68].

In order to calculate the particle size distribution, the first step was to select a particle size measurement technique. This choice depends on the accuracy required and the circumstances. There is no general ‘best’ method for PSD analysis. The best method in a particular case depends on the nature of the soil being analyzed, the purpose of the analysis, time constraints, and the equipment available.

In this study the technique of multiple sieves was used. A stack of sieves is placed on top of a shaker with the coarsest sieve at the top and the finest one at the bottom (Figure 2.8). A pan is placed underneath the stack. A sample of granular material is placed on the top sieve and shaken for a fixed period of time at a fixed amplitude and pulse frequency. The material in each sieve is then weighed and the particle size distribution obtained. The complete procedure for this test is outlined in guidelines from the American Society for Testing and Materials (ASTM) C 136 [100].



(a)



(b)

Figure 2.8 a) A stack of sieves, schematic b) The stack of sieves on a shaker used in this study

The results from performing this test in the current study can be seen in Table 2.4.

Table 2.4 Sieve analysis results

Sieve mesh #	Aperture	Weight without sand (g)	Weight with sand (g)	Weight of sand (g)
10	2 mm	434.9	436.6	1.7
18	1mm	422.9	674.3	251.4
35	500μm	422.2	1118.8	696.6
60	250μm	395.1	1037	641.9
120	125μm	355.7	471.6	115.9
200	75μm	301.4	308.6	7.2
Pan	---	334.5	335.5	1
			total	1715.7

Sieve analysis results are commonly fitted by the log-normal distribution. Crow and Shimizu [101] present the probability density and cumulative distribution functions for the log-normal distribution thus:

$$f_x(d_p^*) = \frac{1}{d_p^* \sigma \sqrt{2\pi}} e^{-(\ln d_p^* - \mu)^2 / 2\sigma^2} \quad (2.18)$$

where the mean (μ) and standard deviation (σ) are calculated as a function of the normalized diameter of the aggregate ($d_p^* = \frac{d}{d_0}$) where $d_0 = 400 \mu\text{m}$, thus:

$$\mu = \ln(E[d_p^*]) - \frac{1}{2} \ln \left(1 + \frac{\text{Var}[d_p^*]}{(E[d_p^*])^2} \right) \quad (2.19)$$

$$\sigma^2 = \ln \left(1 + \frac{\text{Var}[d_p^*]}{(E[d_p^*])^2} \right) \quad (2.20)$$

Using these equations, a log-normal diagram could be plotted, see Figure 2.9. The mean and standard deviation were $\mu = 0.69$ and $\sigma = 0.68$, respectively. In Figure 2.9 the crosslets represent the relative numbers of particles of a given size and the solid line is a log-normal model of the size distribution of the sand.

Figure 2.10 is a photograph of the sand that was used in flat-surface experiments in this study. The heap has a linear region characterized by an angle of repose, θ_s , which was here 34° . The overall coefficient of static friction of the grains was calculated from this as $\mu_s = \tan(\theta_s) = 0.65$.

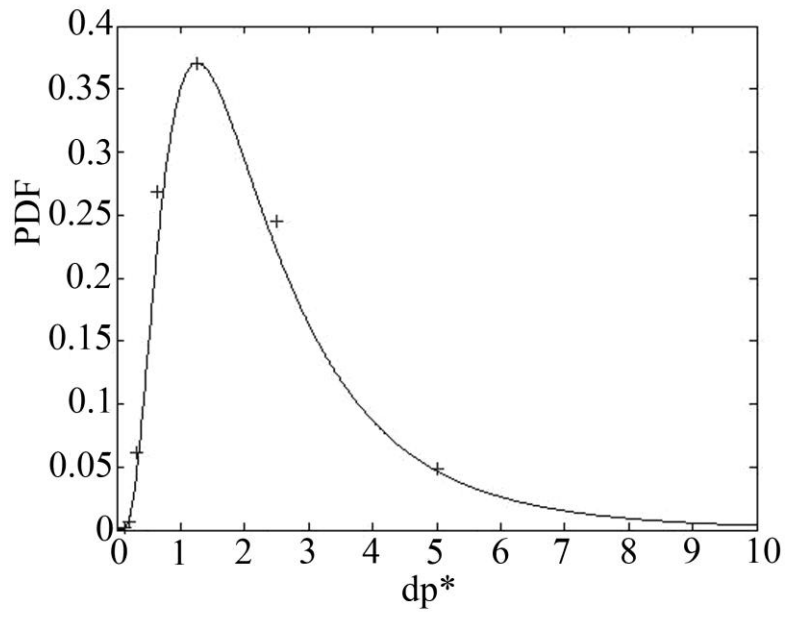


Figure 2.9 The particle size distribution of the sand used in the current study. The crosslets signify the results of the sieving. The solid line is a log-normal fit with location and scale parameters $\mu = 0.69$ and $\sigma = 0.68$, respectively.

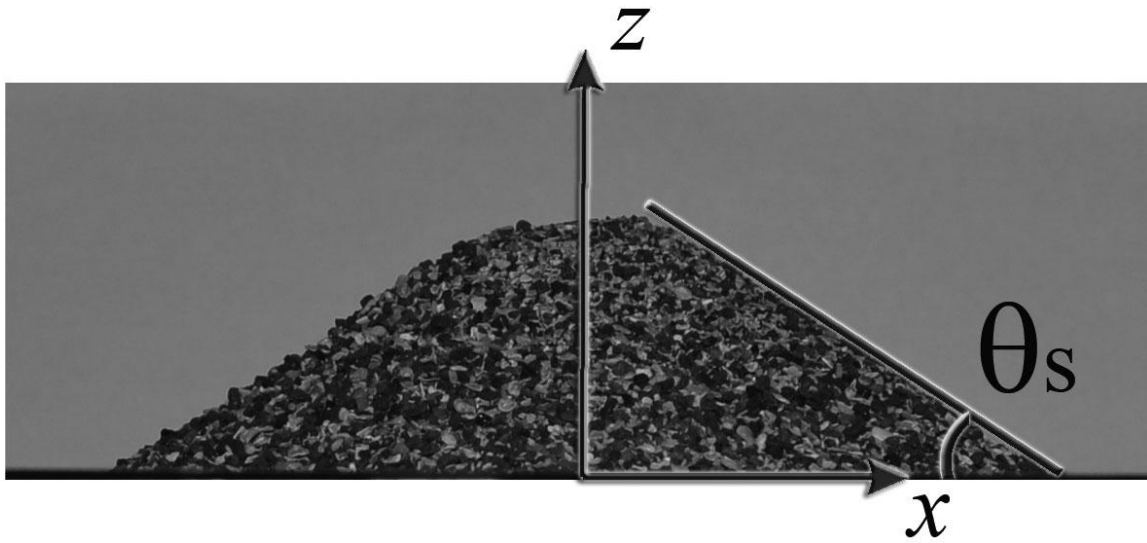


Figure 2.10 An image of a pile of a ternary mixture of glass beads used in the current study on a flat surface. The slope of the pile is $\theta_s = 34^\circ$.

2.4 Observations

2.4.1 Flowing grains in a rectangular container

The aim of the first set of experiments was to determine whether tilts occur in a rectangular container when an initially flat bed of sand is vibrated horizontally with ($\omega_x/2\pi = 42$ Hz and $A_x = 10^{-3}$ m) and ($\omega_y/2\pi = 25$ Hz and $A_y = 10^{-3}$ m). Figure 2.11 (a) and (b) illustrates instantaneous configurations after $t = 5$ s. The bed geometry became unstable, and the bed lost spatial symmetry by forming piles near the container walls. The particles moved down the outer surface of the piles and rearranged in a trough in the middle of the container. The north-south direction corresponds to the x -axis.

2.4.2 Free surface mapping

It is not possible to reconstruct a 3D model from a single image of the container. However, an optical processing algorithm can create a 3D model from photographs taken at multiple known fixed locations.

These types of algorithms are based on so-called edge detection. There are different edge detection algorithms, a few of whom have been developed for gray images. In this study, the main purpose of using this method is to give experimental results in a form that can be used to check the simulation results. The edge-detecting algorithm will now be described briefly.

Unlike gray imagery that uses only color (black), color images have three color components (red, green and blue), making edge detection correspondingly more difficult.

Recently, however, commercial software has been appearing that employs 3D color image processing in an accessible manner. For example, Autodesk recently released a scanning software called 123D Catch [102]. A 3D mesh of the instantaneous free surface of the sand in the container was obtained from a number of photographs that were taken with six synchronized cameras arranged around the container as shown in Figure 2.11(a). The said algorithm transformed a set of six 2D photos into a fully rendered 3D computer model of the instantaneous free surface of sand, see Figure 2.11 (b). Figure 2.11 (c) provides detailed, cross-sectional views of the free surface. It is comparable to looking into a loaf of bread by cutting it into thin slices. Figure 2.11 (d) represents the contours of the free surface of sand on the 7th slice at $x = L$. The position of this slice in the top view of the free surface is shown in Figure 2.11 (b). The dynamic angle of repose, θ_d , can be measured from Figure 2.11 (d). In this case, $\theta_d = 29^\circ$.

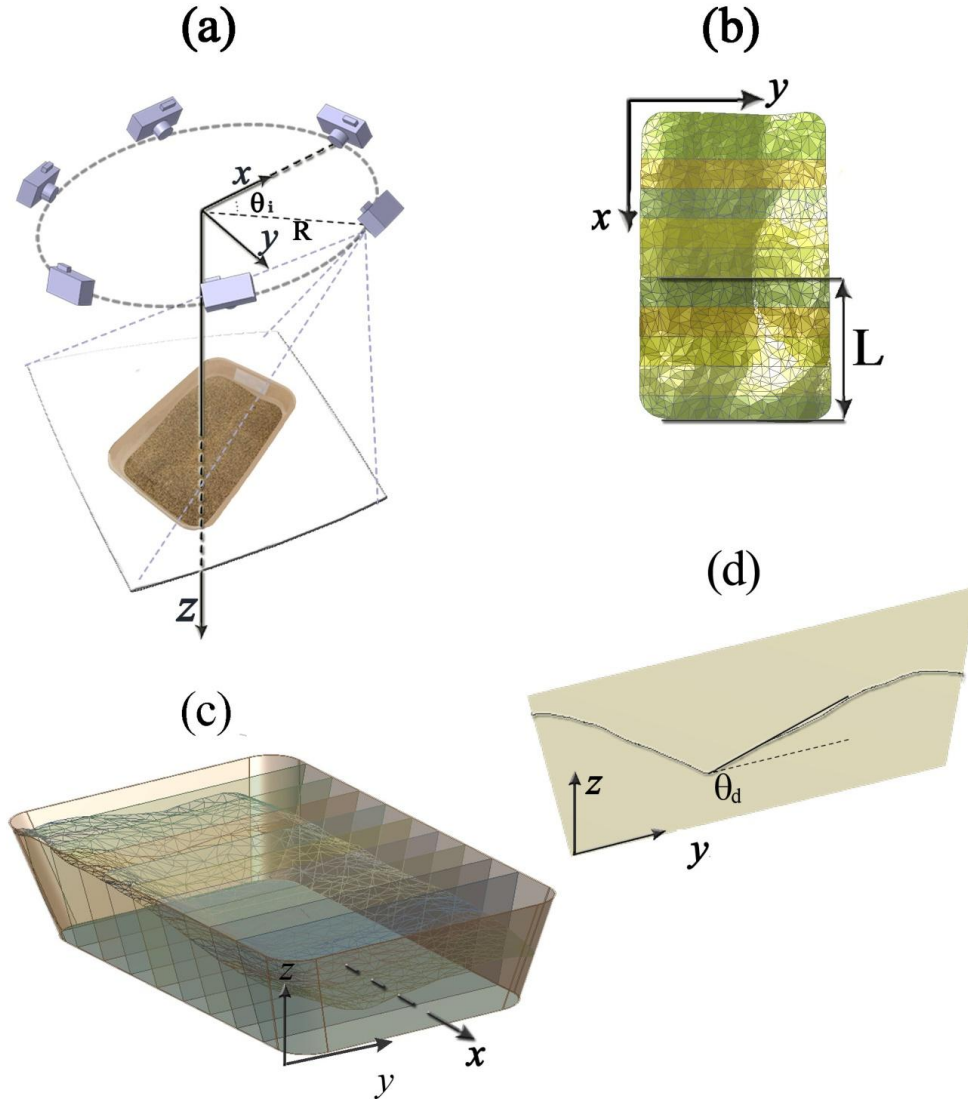


Figure 2.11 (a) Multi-camera arrangement. Six cameras were located at the vertices of a regular hexagon with side length of 35 cm, $R = 35$ cm, and $\theta = 60^\circ$. (b) An instantaneous free surface, obtained using Autodesk 123D Catch. The sampling slice is located at $x = L$, where L is approximately 10 cm. (c) A set of cross-sectional views of the free surface of the sand in the container. (d) The contour of the free surface on the sampling slice shown in (b).

3 Results[103]

3.1 Computer Simulations

Figure 2.9 shows that the most common particle size was $d_p \approx 500 \mu\text{m}$. The size distribution and shape of the particles are important factors in the observed granular flows. However, the simulations were performed for one mixture of spherical grains with diameters $d_{p1} = 500 \mu\text{m}$, $d_{p2} = 350 \mu\text{m}$, and $d_{p3} = 600 \mu\text{m}$. The simulation of air-grain coupling defined an upper grain size limit for adequate air-grain coupling at $600 \mu\text{m}$.

3.2 Polydisperse aggregates

In a polydisperse aggregate, both slipping and sticking motions may be observed. Sticking may cause the aggregates to fold and become considerably more compact. Figure 3.1(a) illustrates the sketch and grid for a simple granular aggregate that consists of three spheres with diameters $d_{p1} = 500 \mu\text{m}$, $d_{p2} = 350 \mu\text{m}$, and $d_{p3} = 600 \mu\text{m}$. The grid was made sufficiently fine to model regions with large stress and strain gradients. The coefficient of friction between the spheres was assumed to be $\mu_s = 0.65$.

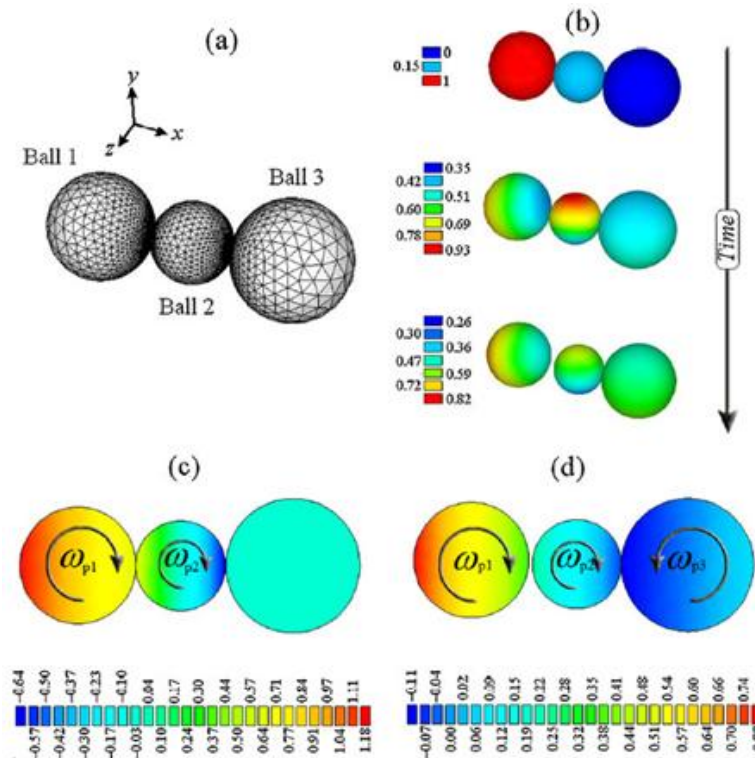


Figure 3.1 (a) A polydisperse aggregate and its computational grid. The diameters of ball-1, ball-2 and ball-3 are $500 \mu\text{m}$, $350 \mu\text{m}$, and $600 \mu\text{m}$, respectively. (b) Time evolution of the dimensionless velocities of the particles in the aggregate. At the end of the contact process, ball-2 and ball-3 stuck together. (c and d) Time evolution of the translational and

angular velocities of the particles in the aggregate. The two configurations are separated by $t = 20 \mu s$.

The coefficient of kinetic friction was assumed to depend on V_{rel} , which is the relative velocity of the surfaces in contact [80]. The value of this coefficient decreases with an increase in velocity, thus:

$$\mu_c = \mu_d + (\mu_p - \mu_d)e^{-CV_{rel}} \quad (3.1)$$

where μ_d is the coefficient of dynamic friction and C is the exponential decay coefficient, which was not known in advance but was extracted from the data as described by Zamankhan [104]. The coefficient of dynamic friction was estimated from $\mu_d = \tan(\theta_d)$. In this work, μ_d was assumed to be 0.55.

The finite-element method (FEM) [105] was used to predict the time evolution of the dimensionless velocities of the balls, as shown in Figure 3.1(b). The final configuration in Figure 3.1 (b) shows that “ball 2” and “ball 3” stuck together at the end of the interaction. Figure 3.1 (c) and (d) shows the time evolution of the translational and angular velocities of the balls in the aggregate. “Ball 2” was displaced in the x-direction and collided with the stationary “ball 3”. After this collision, the angular velocity of “ball 3” was in the opposite direction to “ball 2”.

The dimensionless velocities of the ball centroids in the x- and y-directions as functions of time are shown in Figure 3.2(a) and (c), with squares, circles, and diamonds representing the dimensionless velocities of “ball 1”, “ball 2”, and “ball 3”, respectively. The dimensionless velocities in the x- and y-directions were defined as

$$V_x^* = \frac{V_x}{V_{x0}^{(1)}} \quad (3.2)$$

$$V_y^* = V_y/V_{y0}^{(1)} \quad (3.3)$$

Figure 3.2 (e) shows ω_{pz}^* , defined as

$$\omega_{pz}^* = \frac{\omega_{pz}}{V_{x0}^{(1)}} \quad (3.4)$$

where ω_{pz} represents the particle angular velocity as a function of time.

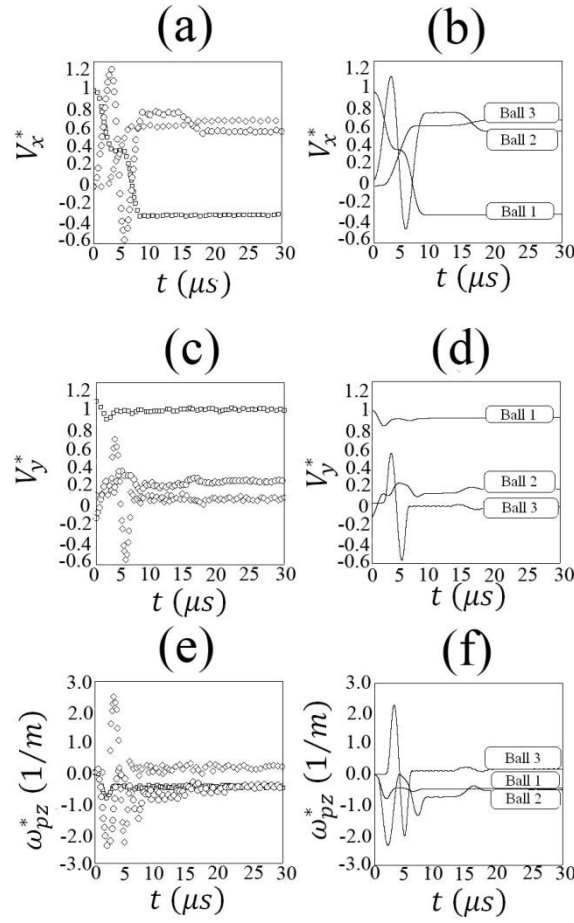


Figure 3.2 (a) The computed dimensionless velocity of particles in the x-direction as a function of time using FEM. Here and in (c) and (e), squares, circles and diamonds represent the dimensionless velocities of “ball 1”, “ball 2”, and “ball 3”, respectively. (b) The computed dimensionless velocity of particles in the x-direction as a function of time. Here and in (d) and (f), the results were obtained with a simplified model. (c) The computed dimensionless velocity of particles in the y-direction as a function of time using FEM. (d) The computed dimensionless velocity of the particles in the y-direction as a function of time. (e) The computed angular velocity of particles in the z-direction as a function of time using FEM. (f) The computed angular velocity of particles in the z-direction as a function of time.

The contact dynamics of the particles in this simple polydisperse aggregate were also calculated by a simplified model [105]. The results are shown in Figure 3.2 (b), (d) and (f). The purpose was to assess the ability of the simplified model to predict complex flows of dense granular materials. Figure 3.2 shows a satisfactory agreement between the FEM results and the predictions of the simplified model.

3.3 Simulation of sand perturbed by an orbital shaker

Simulations of a bed of air-immersed solid particles inside a polycarbonate plastic container were performed with the models described in the preceding sections. The time step used in the simulations was $\Delta t = 10^{-7}$ s. The moving deforming mesh model where the node motion varied sinusoidally in time and space was used, and the ratio of the mean particle diameters to the minimum mesh size did not exceed 0.48.

A mixture of spherical solid particles with diameters $d_{pm} = 500 \text{ } \mu\text{m}$, $d_{ps} = 350 \text{ } \mu\text{m}$, and $d_{pl} = 600 \text{ } \mu\text{m}$ was poured into the container to a height of h_{p0} , see Fig. 6(a). The volume fraction of the smallest particles in the mixture was $\phi_{ss} = 0.20$, that of the largest particles was $\phi_{sl} = 0.18$, and the total solid volume fraction in the container was $\phi_s = 0.64$. The free surface of the solid particles was nearly flat at the start of the simulation. The container underwent orbital (horizontal) oscillations of the form of Equation (1.31) with $(\omega_x/2\pi = 42 \text{ Hz and } A_x = 10^{-3} \text{ m})$ and $(\omega_y/2\pi = 25 \text{ Hz and } A_y = 10^{-3} \text{ m})$.

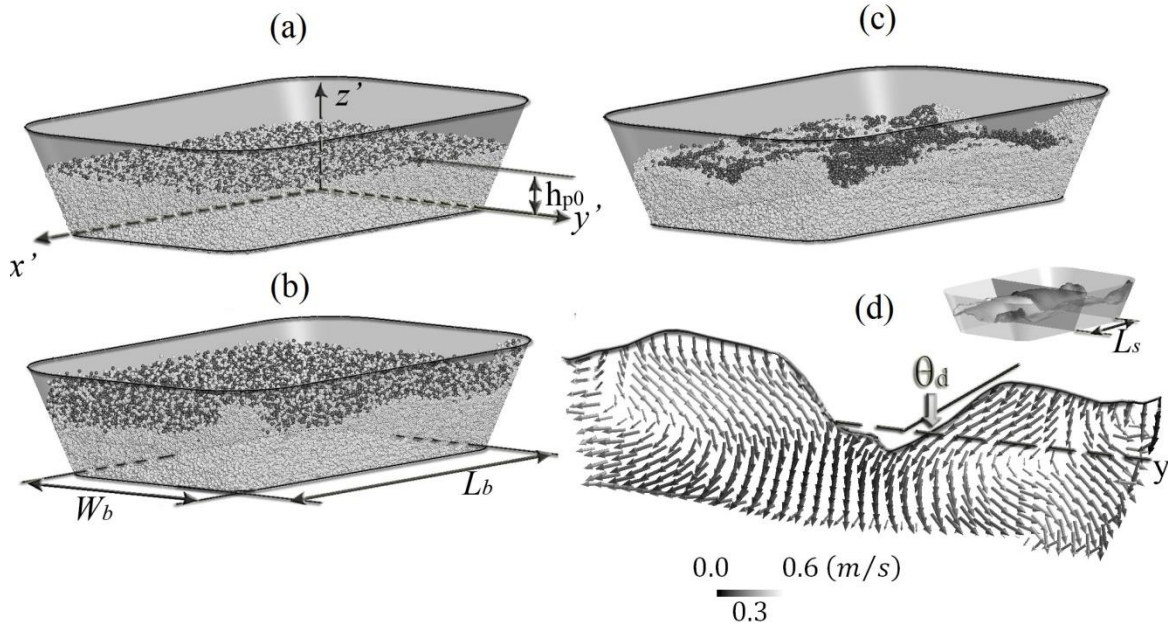


Figure 3.3 (a) The initial configuration of the solid particles used for the numerical simulation where $h_{p0} = 3.5$ cm. (b) The instantaneous configuration of the solid particles at $t = 1$ s, with $W_b = 14$ cm and $L_b = 24$. (c) The instantaneous configuration of the solid particles at $t = 2$ s. (d) The computed average particle velocity distribution on a yz -plane. Inset: the free surface and position of the plane, $L_s = 11$ cm.

We compared the results in Figure 2.11 (a) and Figure 3.3 (c) and concluded that the model captured a number of salient features of the experiments. The Reynolds number of the granular bed is larger than 50, which justifies the use of LES for simulations of tilting granular flows.

3.4 Simulation of swirling granular flows

Figure 3.4 (a) and (b) illustrates the initial configuration of sand before it undergoes horizontal vibration. Similar to the case described in the preceding section, a mixture of spherical solid particles with diameters $d_{pm} = 500 \mu\text{m}$, $d_{ps} = 350 \mu\text{m}$, and $d_{pl} = 600 \mu\text{m}$ was used in the simulation. The volume fractions of the small, medium and large particles in the mixture were $\phi_{ss} = 0.20$, $\phi_{sm} = 0.26$, and $\phi_{sl} = 0.18$, respectively.

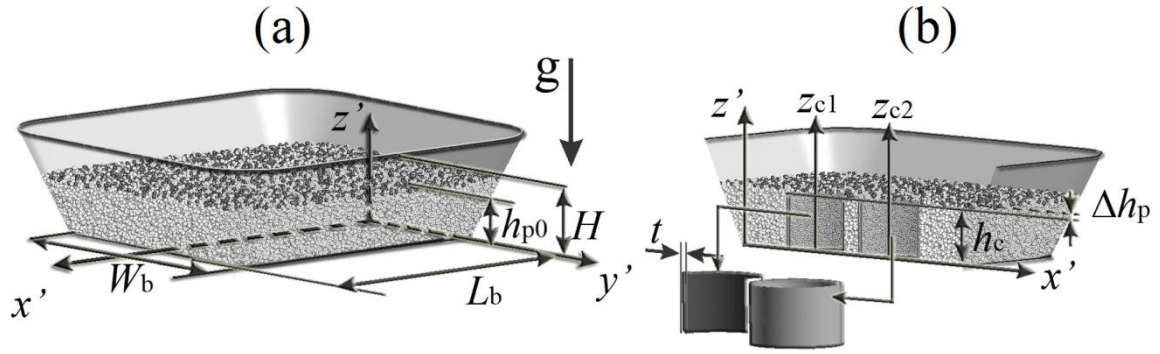


Figure 3.4 (a and b) The initial configuration of the solid particles used for the numerical simulation, where $h_{p0} = 3.5 \text{ cm}$, $H = 6 \text{ cm}$, $W_b = 14 \text{ cm}$, $L_b = 16 \text{ cm}$, $h_c = 3.2 \text{ cm}$, $t = 0.2 \text{ cm}$ and $\Delta h_p = 0.3 \text{ cm}$.

Figure 3.5 (a)–(c) shows instantaneous configurations of the particles after $t = 2 \text{ s}$. Figure 3.5 (d) depicts the computed average particle velocity field in the xy -plane, in the same position as in the video. A simple analysis of Figure 3.5 (d) reveals that the average spin rate of the particles was $\omega_p = 15.7 \text{ rad/s}$, which was nearly constant; the system shown in the video, combined with the mathematical model used in this study, has the potential to be used as a viscometer for dense granular fluids.

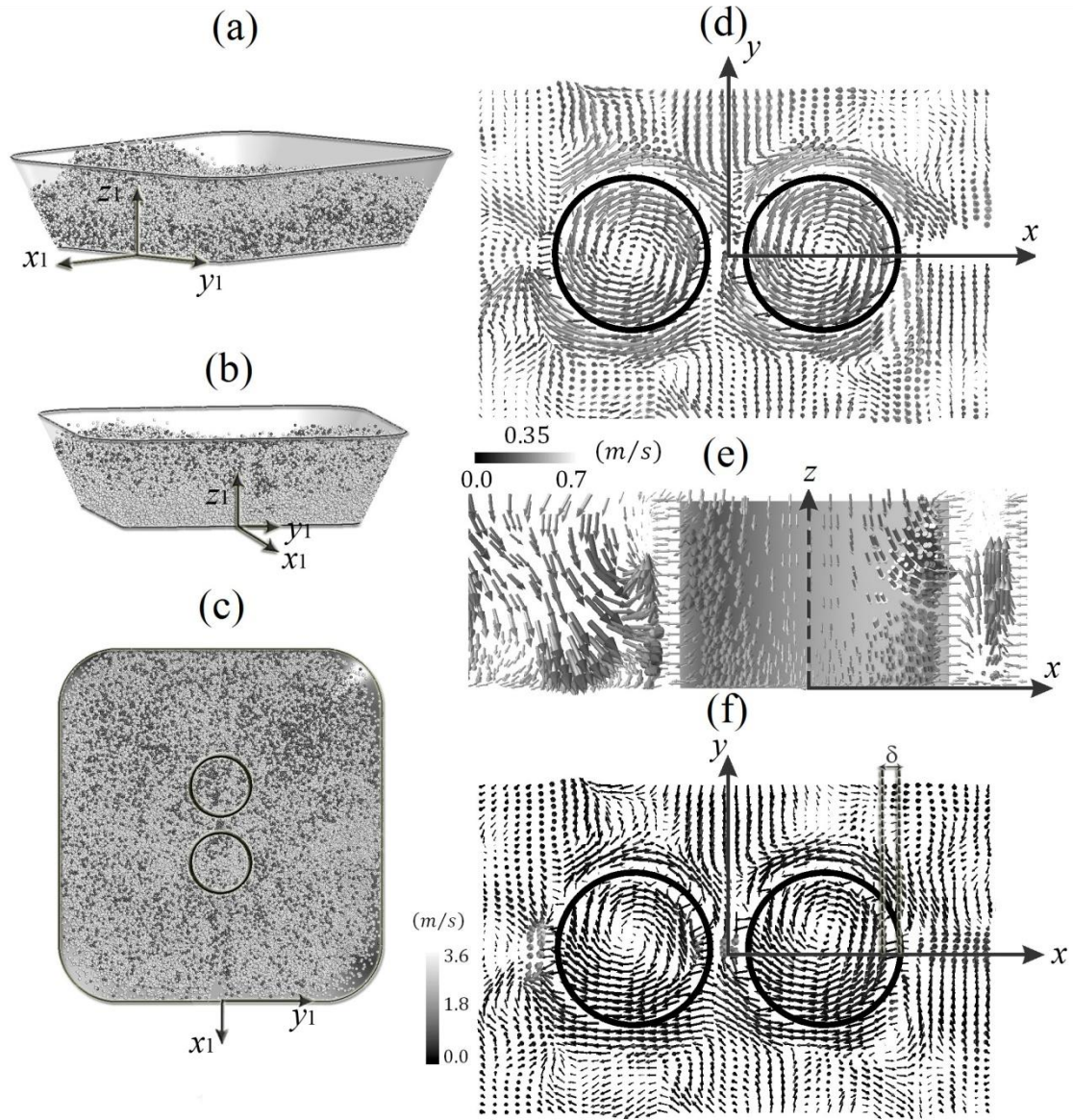


Figure 3.5 (a–c) The instantaneous configuration of the solid particles at $t = 2$ s. (d) The computed average particle velocity field in the xy -plane at $z_l = 3.22$ cm. (e) The computed average particle velocity field in the xz -plane at $y_l = 0$. (f) The computed average air velocity field in the same xy -plane as (d).

Figure 3.5 (e) shows the computed average particle velocity field in the xz -plane, indicating that a unique swirling-convection regime for granular flow was found in this study. Figure 3.5 (f) illustrates the computed average air velocity field in the xy -plane, similar to that in Figure 3.5 (d). As shown in Figure 3.5 (f), the air is being displaced in the negative x -direction due to the instantaneous acceleration of the container. However, the displacement of solid particles appears to be smaller, as shown in Figure 3.5 (d).

The large granular bed Reynolds number computed for the swirling-convection regime indicates that it is necessary to use LES for accurately simulating complex granular flows.

4 Conclusions

A general fruit powder product line has been considered. The advantages of adding value to the organic fruits in different points of view such as finance and reducing the percentage of the waste fruits discussed and the usefulness of the system has been proved.

Different parts of the product line introduced and mathematical models that employing for design those parts (i.e. spray drier, cyclone collector) briefly discussed and introduced. Also recent works that has been done to adapt the design of those equipments briefly reviewed.

As the last section of the every single product line is the packing system, the main focus of this study was study the behavior of the granular flow under specific vibrating condition. Because most of the recent studies just applied and studied this behavior under the vertical vibration, here, horizontal vibration applied to our experimental system.

The acceleration that applied to system has been measured by ADXL345 accelerometer and applied in the models. A LabView software employed in order to observe the acceleration in a t live time.

The horizontally vibrated air–grain system exhibited novel swirling granular flow. The granular bed Reynolds number is in the range $25 < Re_{slip} \leq 180$, which indicates that the flow regime was turbulent.

The new swirling-convection regime was simulated successfully with a Lagrangian (particle-based) method combined with LES.

An optical processing algorithm was developed, which generated a three-dimensional model of the system from photographs taken at multiple locations at approximately the same time. Comparing the results from the experience surface scan with employing the image processing algorithm confirmed the CFD results.

This image processing algorithm, combined with the Eu/La mathematical methods running on GPUs, is possibly the most interesting approach for future work on the development of a viscometer for dense granular fluids.

References

1. Borlaug, N.E., *The Green Revolution Revisited and The Road Ahead*, 2000: Anniversary Nobel Lecture, Norwegian Nobel Institute in Oslo, Norway.
2. Kwa, A., *Agriculture in Developing Countries*, 2001.
3. MAJ. *Ministry of Agriculture of Iran*. 2007; Available from: <http://www.maj.ir/portal/Home/Default.aspx>.
4. Ilyas, M.B., et al., *Post harvest losses in apple and banana during transport and storage* Pakistan Journal of Agricultural Sciences, 2007. **44**(3).
5. Gutman, I., *Industrial uses of mechanical vibrations* 1968, London,: Business Books Ltd. xv, 331 p.
6. Hough, S.E., *Earthshaking science : what we know (and don't know) about earthquakes* 2002, Princeton, N.J.: Princeton University Press. xvi, 238 p.
7. Pudasaini, S.P. and K. Hutter, *Avalanche dynamics : dynamics of rapid flows of dense granular avalanches* 2007, Berlin ; New York: Springer. xxiv, 602 p.
8. SARE. 2011; Available from: <http://www.westernsare.org/>.
9. Stickler, G. *Solar Radiation and the Earth System*. 2009; Available from: <http://education.gsfc.nasa.gov/experimental/all98invproject.site/pages/science-briefs/ed-stickler/ed-irradiance.html>.
10. Loster, M. *Solar radiation at the Earth's surface*. 2006; Available from: http://www.sheffieldsolarfarm.group.shef.ac.uk/welcome/solar_radiation_at_earth_surface.
11. FAO. *Food and Agriculture Organization of the UNITED NATIONS*. 2007; Available from: http://www.fao.org/index_en.htm.
12. USAPPLE. *US Apple Association*. 2007; Available from: <http://www.usapple.org/>.
13. ERS. *Economic Research Service*. 2007; Available from: <http://www.ers.usda.gov/>.
14. CNNMoney. *Top Industries: Fast growers*. 2007; Available from: <http://money.cnn.com/magazines/fortune/fortune500/2008/performers/industries/fastgrowers/>.
15. BLS, *Consumers Expenditures 2008*, 2008, Bureau of Labor and Statistics.
16. Cox, D.N., et al., *Vegetables and fruits: barriers and opportunities for greater consumption*. Nutrition & Food Science, 1996. **96**(5): p. 44-47.
17. Van Duyn, M.S. and E. Pivonka, *Overview of the health benefits of fruit and vegetable consumption for the dietetics professional: Selected literature*. Journal of the American Dietetic Association, 2000. **100**(12): p. 1511-1521.
18. Rolls, B.J., J.A. Ello-Martin, and B.C. Tohill, *What can intervention studies tell us about the relationship between fruit and vegetable consumption and weight management?* Nutrition Reviews, 2004. **62**(1): p. 1-17.
19. Mintel. 2008; Available from: <http://www.mintel.com/>.
20. Rosson, C.P. and F.J. Adcock, *The US market for passion fruit juice: International marketing case study.*, 2000: Department of Agricultural Economics, Texas A&M University.
21. Thor, E. and A. Savitry, *Assessing Trends in the U.S. Fruit Juice Market: Opportunities for Mexican Fruit Juices*, 2001: Center for North American Studies, Department of Agricultural Economics, The Texas A&M University System.

22. Hui, Y.H. and J.z. Barta, *Handbook of fruits and fruit processing*. 1st ed 2006, Ames, Iowa: Blackwell Pub. xii, 697 p.
23. Mosshammer, M.R., F.C. Stintzing, and R. Carle, *Evaluation of different methods for the production of juice concentrates and fruit powders from cactus pear*. Innovative Food Science & Emerging Technologies, 2006. **7**(4): p. 275-287.
24. Mujumdar, A.S., *Handbook of industrial drying*. 3rd ed 2007, Boca Raton, FL: CRC/Taylor & Francis. 1280 p.
25. Mezhericher, M., A. Levy, and I. Borde, *Modelling of particle breakage during drying*. Chemical Engineering and Processing, 2008. **47**(8): p. 1410-1417.
26. Patel, R.P., M.P. Patel, and A.M. Suthar, *Spray drying technology: an overview*. Indian Journal of Science and Technology, 2009. **2**(10): p. 44-47.
27. Wallis, G.B., *One-dimensional two-phase flow* 1969, New York,: McGraw-Hill. xxi, 408 p.
28. Kessler, H.G., *Food Engineering and Dairy Technology*. International Journal of Dairy Technology, 1981. **34**(4): p. 171-171.
29. Mezhericher, M., A. Levy, and I. Borde, *Spray drying modelling based on advanced droplet drying kinetics*. Chemical Engineering and Processing: Process Intensification, 2010. **49**(11): p. 1205-1213.
30. Gidaspow, D., *Multiphase flow and fluidization : continuum and kinetic theory descriptions* 1994, Boston: Academic Press. xx, 467 p.
31. Tsuji, Y., T. Kawaguchi, and T. Tanaka, *Discrete Particle Simulation of 2-Dimensional Fluidized-Bed*. Powder Technology, 1993. **77**(1): p. 79-87.
32. Yu, A.B. and B.H. Xu, *Particle-scale modelling of gas-solid flow in fluidisation*. Journal of Chemical Technology and Biotechnology, 2003. **78**(2-3): p. 111-+.
33. Deen, N.G., et al., *Review of discrete particle modeling of fluidized beds*. Chemical Engineering Science, 2007. **62**(1-2): p. 28-44.
34. Zhu, H.P., et al., *Discrete particle simulation of particulate systems: Theoretical developments*. Chemical Engineering Science, 2007. **62**(13): p. 3378-3396.
35. Cundall, P.A. and O.D.L. Strack, *A Discrete Numerical-Model for Granular Assemblies - Reply*. Geotechnique, 1980. **30**(3): p. 335-336.
36. Langston, P.A. and U. Tuzun, *Continuous Potential Discrete Particle Simulations of Stress and Velocity-Fields in Hoppers - Transition from Fluid to Granular Flow*. Chemical Engineering Science, 1994. **49**(8): p. 1259-1275.
37. Langston, P.A., U. Tuzun, and D.M. Heyes, *Discrete Element Simulation of Internal-Stress and Flow-Fields in Funnel Flow Hoppers*. Powder Technology, 1995. **85**(2): p. 153-169.
38. Langston, P.A., U. Tuzun, and D.M. Heyes, *Discrete Element Simulation of Granular Flow in 2d and 3d Hoppers - Dependence of Discharge Rate and Wall Stress on Particle Interactions*. Chemical Engineering Science, 1995. **50**(6): p. 967-987.
39. Zhu, H.P. and A.B. Yu, *Averaging method of granular materials*. Physical Review E, 2002. **66**(2).
40. Zhou, Y.C., et al., *Rolling friction in the dynamic simulation of sandpile formation*. Physica a-Statistical Mechanics and Its Applications, 1999. **269**(2-4): p. 536-553.
41. Walton, O.R. and R.L. Braun, *Viscosity, Antigranulocytes-Temperature, and Stress Calculations for Shearing Assemblies of Inelastic, Frictional Disks*. Journal of Rheology, 1986. **30**(5): p. 949-980.
42. Walton, O.R., *Numerical-Simulation of Inclined Chute Flows of Monodisperse, Inelastic, Frictional Spheres*. Mechanics of Materials, 1993. **16**(1-2): p. 239-247.
43. Iwashita, K. and M. Oda, *Rolling resistance at contacts in simulation of shear band development by DEM*. Journal of Engineering Mechanics-Asce, 1998. **124**(3): p. 285-292.
44. Iwashita, K. and M. Oda, *Micro-deformation mechanism of shear banding process based on modified distinct element method*. Powder Technology, 2000. **109**(1-3): p. 192-205.

45. Li, Y., J.P. Zhang, and L.S. Fan, *Numerical simulation of gas-liquid-solid fluidization systems using a combined CFD-VOF-DPM method: bubble wake behavior*. Chemical Engineering Science, 1999. **54**(21): p. 5101-5107.
46. Xiong, Y.Q., M.Y. Zhang, and Z.L. Yuan, *Three-dimensional numerical simulation method for gas-solid injector*. Powder Technology, 2005. **160**(3): p. 180-189.
47. Potic, B., et al., *Fluidization with hot compressed water in micro-reactors*. Chemical Engineering Science, 2005. **60**(22): p. 5982-5990.
48. Ergun, S., *Fluid flow through packed columns*. Chemical Engineering and Processing, 1952. **48**: p. 89-94.
49. Wen, C.Y. and Y.H. Yu, *Mechanics of fluidization*, in *A.I.Ch.E.* 1966. p. 100-111.
50. Richardson, J.F., *Incipient fluidization and particulate systems* 1971, In: Davidson, J.F., Harrison, D. (Eds.), *Fluidization*. Academic Press, New York.
51. Di Felice, R., *The voidage function for fluid-particle interaction systems*. International Journal of Multiphase Flow, 1994. **20**: p. 153-159.
52. Choi, H.G. and D.D. Joseph, *Fluidization by lift of 300 circular particles in plane Poiseuille flow by direct numerical simulation*. Journal of Fluid Mechanics, 2001. **438**: p. 101-128.
53. Anderson, T.B. and R. Jackson, *A fluid mechanical description of fluidized beds Equations of motion*. Industrial and Engineering Chemistry Fundamentals, 1967. **6**: p. 527-539.
54. Odar, F. and W.S. Hamilton, *Forces on a sphere accelerating in a viscous fluid*. Journal of Fluid Mechanics, 1964. **18**: p. 302-314.
55. Odar, F., *Verification of proposed equation for calculation of forces on a sphere accelerating in a viscous fluid*. Journal of Fluid Mechanics, 1966. **25**: p. 591-592.
56. Reeks, M.W. and S. Mckee, *The Dispersive Effects of Basset History Forces on Particle Motion in a Turbulent-Flow*. Physics of Fluids, 1984. **27**(7): p. 1573-1582.
57. Mei, R., R.J. Adrian, and T.J. Hanratty, *Particle Dispersion in Isotropic Turbulence under Stokes Drag and Basset Force with Gravitational Settling*. Journal of Fluid Mechanics, 1991. **225**: p. 481-495.
58. Saffman, P.G., *Lift on a small sphere in a slow shear flow*. Journal of Fluid Mechanics, 1965. **22**: p. 385-400.
59. Saffman, P.G., *Corrigendum to "The lift on a small sphere in a slow shear flow"*. Journal of Fluid Mechanics, 1968. **31**.
60. Rubinow, S.I. and J.B. Keller, *The transverse force on a spinning sphere moving in a viscous fluid*. Journal of Fluid Mechanics, 1961. **11**: p. 447-459.
61. King, P.J., et al., *Instabilities in vertically vibrated fluid-grain systems*. European Physical Journal E, 2007. **22**(3): p. 219-226.
62. Jafari, A., et al., *Modeling and CFD simulation of flow behavior and dispersivity through randomly packed bed reactors*. Chemical Engineering Journal, 2008. **144**(3): p. 476-482.
63. Serini, V., *"Polycarbonates" in Ullmann's encyclopedia of industrial chemistry* 2000: Weinheim: Wiley-VCH.
64. Sagaut, P., *Large eddy simulation for incompressible flows: An introduction* 1998, Berlin: Springer.
65. Maxey, M.R. and J.J. Riley, *Equation of Motion for a Small Rigid Sphere in a Nonuniform Flow*. Physics of Fluids, 1983. **26**(4): p. 883-889.
66. Ranz, W.E., *Rate-Processes at a Spherical Boundary - a Citation-Classic Commentary on Evaporation from Drops .1.2. By Ranz, W.E., and Marshall, W.R.* Current Contents/Physical Chemical & Earth Sciences, 1993(22): p. 8-8.
67. Mezhericher, M., A. Levy, and I. Borde, *Probabilistic hard-sphere model of binary particle-particle interactions in multiphase flow of spray dryers*. International Journal of Multiphase Flow, 2012. **43**: p. 22-38.
68. Crowe, C.T., *Multiphase flow handbook*. Mechanical engineering series 2006, Boca Raton, FL: CRC : Taylor & Francis.

69. Hoffmann, A.C. and L.E. Stein, *Gas cyclones and swirl tubes : principles, design, and operation*. 2nd ed 2008, Berlin ; New York: Springer. xxvi, 422 p.
70. Chu, K.W., et al., *CFD-DEM simulation of the gas-solid flow in a cyclone separator*. Chemical Engineering Science, 2011. **66**(5): p. 834-847.
71. Bhasker, C., *Flow simulation in industrial cyclone separator*. Advances in Engineering Software, 2010. **41**(2): p. 220-228.
72. Orpe, A.V. and D.V. Khakhar, *Solid-fluid transition in a granular shear flow*. Physical Review Letters, 2004. **93**(6).
73. Metcalfe, G., et al., *Granular friction, Coulomb failure, and the fluid-solid transition for horizontally shaken granular materials*. Physical Review E, 2002. **65**(3).
74. Rubin, D., N. Goldenson, and G.A. Voth, *Failure and strengthening of granular slopes under horizontal vibration*. Physical Review E, 2006. **74**(5).
75. Aumaitre, S., et al., *Comparing flow thresholds and dynamics for oscillating and inclined granular layers*. Physical Review E, 2007. **75**(6).
76. Bejan, A. and A.D. Kraus, *Heat transfer handbook* 2003, New York: J. Wiley. xiv, 1477 p.
77. Lemieux, P.A. and D.J. Durian, *From avalanches to fluid flow: A continuous picture of grain dynamics down a heap*. Physical Review Letters, 2000. **85**(20): p. 4273-4276.
78. Sagaut, P., *Large eddy simulation for incompressible flows : an introduction*. 2nd ed. Scientific computation, 2002, Berlin ; New York: Springer. xxii, 426 p.
79. Zamankhan, P., *Solid structures in a highly agitated bed of granular materials*. Applied Mathematical Modelling, 2012. **36**(1): p. 414-429.
80. Rabinowicz, E., *Friction and wear of materials* 1965, New York,: Wiley. x, 244 p.
81. Bai, G., et al., *Computational fluid dynamics (CFD) insights into agitation stress methods in biopharmaceutical development*. International Journal of Pharmaceutics, 2012. **423**(2): p. 264-280.
82. Colomer, J., F. Peters, and C. Marrase, *Experimental analysis of coagulation of particles under low-shear flow*. Water Research, 2005. **39**(13): p. 2994-3000.
83. Lekhnitskiĭ, S.G., *Theory of elasticity of an anisotropic elastic body*. Holden-Day series in mathematical physics 1963, San Francisco,: Holden-Day. 404 p.
84. Bandyopadhyay, A. and G.C. Basak, *Studies on photocatalytic degradation of polystyrene*. Materials Science and Technology, 2007. **23**(3): p. 307-314.
85. Analog Devices. *Digital Accelerometer*. 2011; Available from: http://www.analog.com/static/imported-files/data_sheets/ADXL345.pdf.
86. MEMSnet. *A Beginner's Guide to MEMS Processes*. 2010; Available from: <https://www.memsnet.org/about/processes/>.
87. MEMSnet. *An information portal for the MEMS and Nanotechnology community*. 2012; Available from: <http://www.memsnet.org/mems/beginner/>.
88. Dao R, M.D.E., Kries H H and Bachelder D M *Convective accelerometer and inclinometer in US Patent Specification*, 5581034, Editor 1996.
89. Leung, A.M., et al. *Micromachined accelerometer based on convection heat transfer*. in *Micro Electro Mechanical Systems, 1998. MEMS 98. Proceedings., The Eleventh Annual International Workshop on*. 1998.
90. Dao R, M.D.E., H.H. Kries, and D.M. Bachelder, *Convective accelerometer and inclinometer*, in *US Patent Specification* 1996.
91. Leung, A.M., et al., *A micromachined accelerometer with no proof mass* 1997: Technical Digest of Int. Electron. Device Meeting (IEDM '97) (Washington, DC, December 1997) p. 899-902.
92. Bahari, J. and A.M. Leung, *Micromachined three-axis thermal accelerometer with a single composite heater*. Journal of Micromechanics and Microengineering, 2011. **21**(7).
93. Butefisch, S., A. Schoft, and S. Buttgenbach, *Three-axes monolithic silicon low-g accelerometer*. Journal of Microelectromechanical Systems, 2000. **9**(4): p. 551-556.

94. Andersson, G.I., *A novel 3-axis monolithic silicon accelerometer*, in *8th Int. Conf. on solid-state sensors and actuators* 1995, Transducers'95/Eurosensors IX: Stockholm, Sweden. p. 558-561.
95. Siva Prasad, M.S.Y., *Design Simulation & Fabrication of Micromachined Acceleration Sensor*, in *Department of Mechanical Engineering* 2010, Jawaharlal Nehru Technological University.
96. Bishop, R.E.D. and D.C. Johnson, *The mechanics of vibration*. Reissued with minor revisions . ed 1979, Cambridge Eng. ; New York: Cambridge University Press. xiv, 592 p.
97. Rodjégård, H., et al., *Capacitive slanted-beam three-axis accelerometer: I. Modelling and design*. Journal of Micromechanics and Microengineering, 2005. **15**.
98. ANALOG_DEVICES, ADXL345, A. DEVICES, Editor 2011.
99. Ristic, L., et al. *Surface micromachined polysilicon accelerometer*. in *Solid-State Sensor and Actuator Workshop, 1992. 5th Technical Digest., IEEE*. 1992.
100. ASTM, *Standard Test Method for Sieve Analysis of Fine and Coarse Aggregates*, 2006.
101. Crow, E.L. and K. Shimizu, *Lognormal distributions : theory and applications*. Statistics, textbooks and monographs 1988, New York: M. Dekker. xiv, 387 p.
102. Autodesk. *Autodesk 123D Catch Software*. 2012; Available from: <http://www.123dapp.com/catch>.
103. Bakhshinejad, A. and P. Zamankhan, *Swirling flows in horizontally vibrated beds of dense granular materials*. Particuology, 2012. **10**(6): p. 683-691.
104. Zamankhan, P., *Bubbling in vibrated granular films*. Physical Review E, 2011. **83**(2).
105. Zamankhan, P. and M.H. Bordbar, *Complex flow dynamics in dense granular flows - Part I: Experimentation*. Journal of Applied Mechanics-Transactions of the Asme, 2006. **73**(4): p. 648-657.

Appendix A

Particuology 10 (2012) 683–691



Contents lists available at SciVerse ScienceDirect

Particuology

journal homepage: www.elsevier.com/locate/partic



Swirling flows in horizontally vibrated beds of dense granular materials

Ali Bakhshinejad*, Piroz Zamankhan

Faculty of Industrial Engineering, Mechanical Engineering and Computer Science, University of Iceland, Hjarðarhagi 2-6, IS-107 Reykjavík, Iceland

ARTICLE INFO

Article history:

Received 5 February 2012

Received in revised form 10 June 2012

Accepted 13 June 2012

Keywords:

Swirl granular flows

Instability

Computer simulation

Measurements

3D drawing tools

3D photo-tracing geometry

ABSTRACT

In a series of experiments, a granular material in a rectangular container with two hollow cylinders was studied as it underwent horizontal vibrations. At the peak values of acceleration, novel swirling granular flows were observed in the cylinders while the grains cascaded down the outer surface of the piles that formed outside the cylinders. Computer simulations were performed that supported our interpretation of the behaviour observed in the experiments.

© 2012 Chinese Society of Particuology and Institute of Process Engineering, Chinese Academy of Sciences. Published by Elsevier B.V. All rights reserved.

1. Introduction

Granular materials are abundant in nature, and their response to vibration plays an important role in natural events such as earthquakes (Hough, 2002) and avalanches (Pudasaini & Hutter, 2007). Grains are vibrated during many industrial applications such as drying, powder mixing, and separation processes (Gutman, 1968).

Horizontal vibrations are used in applications such as vibrating screens. A number of studies have focused on horizontal vibrations (Orpe & Khakhar, 2004). When a bed of grains was immersed in fluid in a horizontal container and subjected to horizontal vibrations, a wealth of phenomena was observed, including solid–fluid granular transitions with hysteresis that disappeared in the presence of a modest vertical air flow corresponding to approximately 40% of the weight of the bed (Metcalf, Tennakoon, Kondic, Schaeffer, & Behringer, 2002). Rubin, Goldenson, and Voth (2006) used optical particle tracking (Aumaitre, Puls, McElwaine, & Gollub, 2007) to measure a granular slope under horizontal vibration and observed that the beads underwent intermittent motion, indicating that micro-rearrangements affected the failure of slopes under external perturbations.

A horizontal granular bed becomes unstable at the peak acceleration relative to gravity, Γ , by acquiring a tilt (Bejan & Kraus, 2003). Aumaitre et al. (2007) studied the onset and dynamics of

flow in shallow, horizontally oscillating granular layers as a function of the depth of the layer and imposed acceleration. They found that the thresholds were slightly different for starting and stopping the flow of avalanches in inclined layers. At Γ , the motion was fluid-like over the entire cycle. The measured flow profiles had time-dependent shapes that differed significantly from previously measured avalanche flow profiles.

The dynamics and stability of a bed composed of solid particles immersed in a fluid may be analysed with a treatment developed by Anderson and Jackson (1968). Their treatment may be more suitable for modelling continuous flows (Lemieux & Durian, 2000). Hence, an alternative approach that combines Lagrangian (particle-based) and Eulerian (grid-based) methods (Eu/La) is required to predict the transition between intermittent and continuous flows. This approach uses large-eddy simulations (LES) to include gas dynamics (Sagaut, 1998). The dynamics of grains is described through molecular dynamics, where the interaction between the grain surfaces is modelled with the generalised form of contact theory developed by Hertz (Zamankhan, 2012). In addition, the coefficient of kinetic friction is assumed to depend on the relative velocity of slipping (Rabinowicz, 1965).

The current study reports the formation of tilts in shaken granular materials in a rectangular container that is vibrated horizontally according to

$$r = A_x \sin(\omega_x t) \mathbf{e}_x + A_y \cos(\omega_y t) \mathbf{e}_y, \quad (1)$$

where A_x , A_y , ω_x , ω_y , \mathbf{e}_x , and \mathbf{e}_y denote, respectively, the displacement amplitudes of the vibrating container, the angular frequencies of the vibration, and the unit vectors in the x and

* Corresponding author. Tel.: +354 696 0932.

E-mail addresses: alb27@hi.is, ali.bakhshinejad@yahoo.com (A. Bakhshinejad), piroz@hi.is (P. Zamankhan).

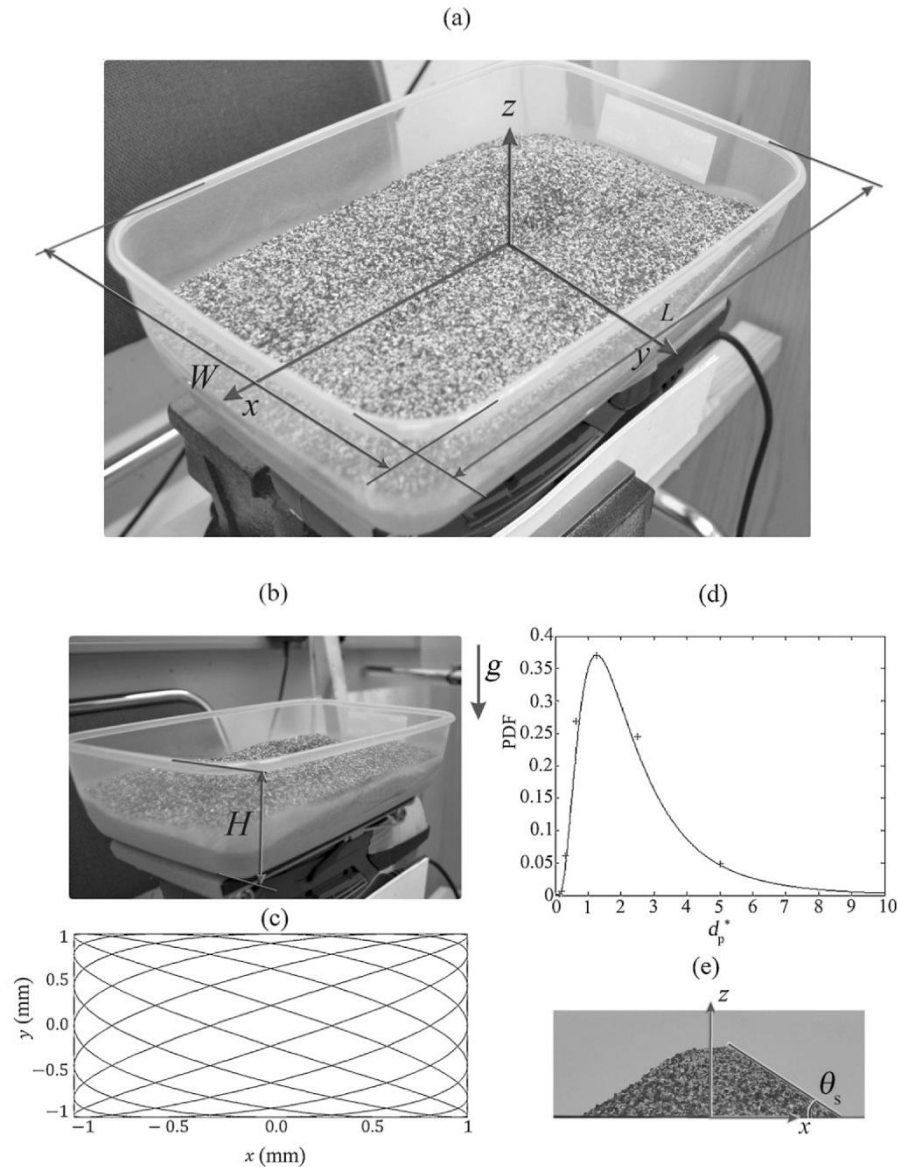


Fig. 1. (a and b) Images of the container and nomenclature. The dimensions of the container are $W = 18$ cm, $L = 28$ cm, and $H = 7$ cm. (c) The typical ellipse-type orbits of the shaker. (d) The particle size distribution of the sand used in these experiments. The crosslets represent the results of a sieve analysis. The solid line is a log-normal fit with location and scale parameters $\mu = 0.69$ and $\sigma = 0.68$, respectively. (e) An image of a pile of a ternary mixture of glass beads used in these experiments on a flat surface. The slope of the pile is $\theta_s = 34^\circ$.

y -directions. Two hollow cylindrical vessels were mounted in the container, with their axes vertical, as shown in the supplemental video. Unique swirling granular flows were observed in the cylinders, with the grains cascading down the surface of the piles outside the cylinders. Numerical simulations were performed to investigate these complex granular flows.

The organisation of this paper is as follows: in Section 2, the experimental apparatus, procedure and experimental results are described. Section 3 presents a mathematical model and the results of numerical simulations of swirling granular flows. The results were obtained with nVidia GPU (graphics processing unit) technology (NVIDIA GPU Computing, 2012). Finally, conclusions are given in Section 4.

2. Experimental methods and observations

2.1. Methods

The polycarbonate plastic container used in this study and pertinent nomenclature are shown in Fig. 1(a) and (b). The container was filled with sand and attached to the centre of a thin cardboard sheet that was clipped to the bottom of the rectangular pad of an orbital shaker. The physical and mechanical properties of polycarbonate plastics are given in Table 1. Orbital shakers are widely used in the pharmaceutical industry to mix liquids in biopharmaceutical processes (Bai & Bee, 2012), and they are also used commonly to study the aggregation and breakup of

Table 1
Material properties (Lekhnitskii, 1963; Bandyopadhyay & Basak, 2007).

Material	Property	Symbol	Value
Polycarbonate	Density	ρ_p	1.20–1.22 g/cm ³
	Young's modulus	E	2.0–2.4 GPa
	Tensile strength	σ_t	55–75 MPa
	Poisson's ratio	ν	0.37
	Coefficient of friction	μ	0.31
Glass	Elastic modulus	E	6.3×10^{10} Pa
	Density	ρ_p	2390 kg/m ³
	Poisson's ratio	ν	0.244
	Instantaneous shear modulus	G_0	2.53×10^{10} Pa
Air	Long time shear modulus	G_∞	6.1×10^9 Pa
	Density	ρ_g	1.225 kg/m ³
	Kinematic viscosity	ν_g	1.7894×10^{-5} m ² /s
Sand	Temperature	T_g	293 K
	Poisson's ratio	ν	0.17
	Density	ρ_p	2.203 g/cm ³
	Bulk modulus	K	37 GPa
Foam	Young's modulus	E	71.7 GPa
	Poisson's ratio	ν	0.1
Foam	Density	ρ_p	1.05 g/cm ³
	Young's modulus	E	3000 MPa

microorganisms and inorganic particle flows in water (Colomer, Petersb, & Marrase, 2005).

A function generator was used to deliver a sinusoidal signal of adjustable frequency and amplitude to a power amplifier, and then transmitted as the input signal to the orbital shaker. The accelerations in the x - and y -directions were monitored with a 3-axis accelerometer attached to the pad. The accelerometer was based on MEMS sensors whose masses were significantly smaller than the mass of the system. These sensors had a sensitivity of 100 mV/g with high resolution up to ± 16 g. A data acquisition system collected the acceleration data from the accelerometer and transferred them via a USB link to a computer for analysis.

The shaker pad underwent horizontal oscillations with the form given in Eq. (1). Fig. 1(c) depicts the ellipse-type orbits that resulted when an offset weight was placed on the motor shaft of the shaker at ($\omega_x/2\pi = 42$ Hz and $A_x = 10^{-3}$ m) and ($\omega_y/2\pi = 25$ Hz and $A_y = 10^{-3}$ m) corresponding to the values of $\Gamma_x = 7.1$ and $\Gamma_y = 2.5$, respectively. It was possible to operate the shaker at different angular speeds.

The sand particles used in the experiments had rough surfaces with medium sphericity and high elasticity. The physical and mechanical properties of the sand are given in Table 1. A sieve analysis (ASTM International-Standards Worldwide, 2006) was performed to assess the particle size distribution, as shown in Fig. 1(d): the crosslets represent the relative numbers of particles of a given size and the solid line is a log-normal model of the size distribution of the sand,

$$f_x(d_p^*) = \frac{1}{d_p^* \sigma \sqrt{2\pi}} e^{-\left(\ln d_p^* - \mu\right)^2 / 2\sigma^2}, \quad (2)$$

where d_p^* is the normalised particle size defined as $d_p^* = d_p/d_0$, d_0 is the reference particle size, μ is the mean and σ is the standard deviation. In the present case, $d_0 = 400$ μ m, $\mu = 0.69$ and $\sigma = 0.68$.

Fig. 1(e) is a photograph of a pile of the sand particles that were used in flat surface experiments in this work. The grains accumulated in a heap with a linear region characterised by an angle of repose, θ_s . The overall coefficient of static friction of the grains was estimated as $\mu_s = \tan(\theta_s) = 0.65$.

2.2. Observations

2.2.1. Flowing grains in a rectangular container

The aim of the first set of experiments was to determine whether tilts occur in a rectangular container when a flat bed of sand is vibrated horizontally, with ($\omega_x/2\pi = 42$ Hz and $A_x = 10^{-3}$ m) and ($\omega_y/2\pi = 25$ Hz and $A_y = 10^{-3}$ m). Fig. 1(a) and (b) illustrates instantaneous configurations after $t = 5$ s. The bed geometry became unstable, and the bed lost spatial symmetry by forming piles near the container walls. The particles moved down the outer surface of the piles and rearranged in a trough in the middle of the container. The north-south direction corresponds to the x -axis.

2.2.2. Free surface mapping

It is not possible to reconstruct a 3D model from a single image of the container. However, an optical processing algorithm can create a 3D model from photographs taken at multiple known fixed locations. For example, Autodesk recently released scanning software called "123D Catch" (Autodesk 123D Catch Software, 2012). A 3D mesh of the instantaneous free surface of the sand in the container was obtained from a number of photographs that were taken from positions around the container. The photos were taken with six synchronised cameras as shown in Fig. 2(a). This algorithm transformed a set of six 2D photos into a fully rendered computer model of the instantaneous free surface of sand, presented in Fig. 2(b). Fig. 2(c) provides detailed, cross-sectional views of the free surface. It is comparable to looking into a loaf of bread by cutting the loaf into thin slices. Fig. 2(d) represents the contour of the free surface of sand on the 7th slice at $x = L$. The position of

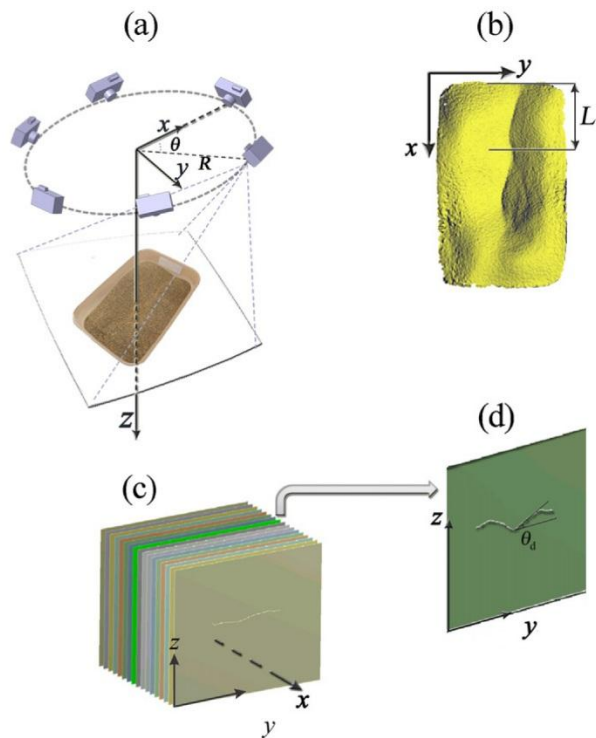


Fig. 2. (a) Multi-camera arrangement. The cameras were located at the vertices of a regular hexagon with side length of 35 cm, $R = 35$ cm, and $\theta = 60^\circ$. (b) An instantaneous free surface, obtained using Autodesk 123D Catch. The sampling slice is located at $x = L$, where L is approximately 10 cm. (c) A set of cross-sectional views of the free surface of the sand in the container. (d) The contour of the free surface on the sampling slice shown in (b).

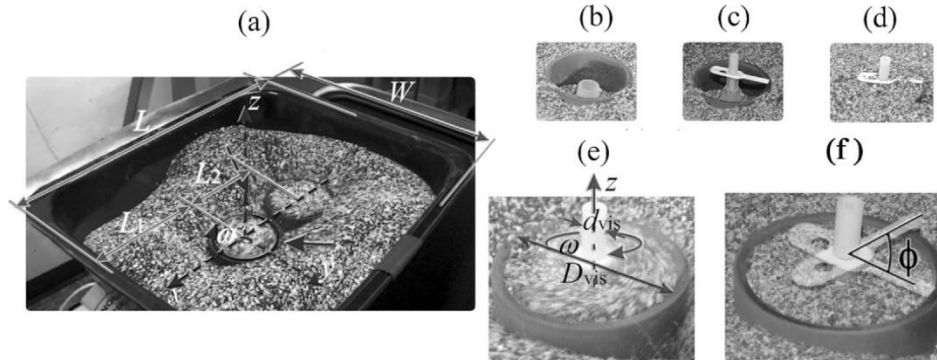


Fig. 3. (a) An image of the black foam tray with two hollow glass cylinders inside the tray. The dimensions are $W = 22$ cm, $L = 24$ cm, $L_1 = 9$ cm, and $L_2 = 6$. (b–d) The propeller and shaft system used to measure the spin of granular material. The length and the height of the propeller are 2.5 cm and 1.5 mm, respectively. Its weight is less than one gram. (e) A snapshot of the circulatory granular flow where $D_{vis} = 2.5$ cm. (f) Positions of the propeller at two different instants with $\phi = 86^\circ$.

this slice in the top view of the free surface is shown in Fig. 2(b). The dynamic angle of repose, θ_d , can be measured from Fig. 2(d). In this case, $\theta_d = 29^\circ$.

2.2.3. Swirling flow

Granular flows can be influenced significantly by container geometry. To investigate the influence of the geometry, a second set of experiments was carried out. Fig. 3 shows a black foam container that contained two hollow glass cylinders. The physical and mechanical properties of the foam and glass containers are given in Table 1. The container was filled with sand and attached to the centre of a thin cardboard sheet. The cardboard was clipped onto the bottom of the rectangular pad of the shaker. At the beginning of the experiment, the sand had a flat free surface. The container underwent horizontal oscillations of the form of Eq. (1), where $(\omega_x/2\pi = 42$ Hz and $A_x = 10^{-3}$ m) and $(\omega_y/2\pi = 25$ Hz and $A_y = 10^{-3}$ m).

Swirling granular flows formed within the cylinders and grains cascaded down the outer surfaces of the piles outside the cylinders as shown in the video. To quantify the spin of the sand particles at the top of the cylinders, a simple propeller shaft system was used, as shown in Fig. 3(b)–(d). The components included a simple bearing, Fig. 3(b); a shaft-bearing assembly that allowed the shaft to spin in the vertical direction relative to the cylindrical container, Fig. 3(c); and a plastic propeller attached to the shaft, Fig. 3(d). The physical and mechanical properties of the propeller made from polycarbonate plastic are given in Table 1.

Fig. 3(e) is a photograph of the spinning propeller that was taken with a slow shutter speed. The propeller speed depends on a number of factors including the particle size and shape. A thorough inspection of this image revealed that the sand particles were spinning at a rather high rate. Images of the propeller and the container were captured and saved using a frame grabber board connected to a video camera. Fig. 3(f) shows the propeller at two positions separated in time by $\Delta t = 0.083$ s. The average spin rate of the propeller was estimated as $\omega = \phi/\Delta t = 18$ rad/s. Here, ϕ is the measure of radians that the propeller was rotated about a fixed point.

It appears that there are no other studies that focus on swirling granular flows similar to those in our video. To further explore this new granular flow regime, we performed computer simulations of a granular material within a rectangular container undergoing horizontal oscillations of the form given by Eq. (1).

3. Computer simulations

Fig. 1(d) shows that the most common particle size was $d_p \approx 500$ μm . The size distribution and shape of the particles are

important factors in these granular flows. However, the simulations were performed for one mixture of spherical grains with diameters $d_{p1} = 500$ μm , $d_{p2} = 350$ μm , and $d_{p3} = 600$ μm . The simulation of adequate air-grain coupling defined an upper grain size limit of 600 μm .

3.1. Polydisperse aggregates

In a polydisperse aggregate, both slipping and sticking motions can be observed. The sticking motion may cause the aggregates to fold and become considerably more compact. Fig. 4(a) illustrates the sketch and grid for a simple granular aggregate that consists of three spheres with diameters $d_{p1} = 500$ μm , $d_{p2} = 350$ μm , and $d_{p3} = 600$ μm . The grid was made sufficiently fine to model regions with large stress and strain gradients. The coefficient of friction between the spheres was assumed to be $\mu_s = 0.65$.

The coefficient of kinetic friction was assumed to depend on V_{rel} , which is the relative velocity of the surfaces in contact (Rabinowicz, 1965). The value of this coefficient decreases with an increase in velocity, represented by $\mu_c = \mu_d + (\mu_p - \mu_d)e^{-CV_{rel}}$ where μ_d is the coefficient of dynamic friction and C is the exponential decay coefficient, which was not known in advance but was extracted from the data as described in an earlier paper (Zamankhan, 2011). The coefficient of dynamic friction was estimated from $\mu_d = \tan(\theta_d)$. In this work, μ_d was assumed to be 0.55.

Finite element method (FEM) (Zamankhan & Bordbar, 2006) was used to predict the time evolution of the dimensionless velocities of the balls, as shown in Fig. 4(b). The final configuration in Fig. 4(b) shows that “ball 2” and “ball 3” stuck together at the end of the interaction. Fig. 4(c) and (d) shows the time evolution of the translational and angular velocities of the balls in the aggregate. “Ball 2” was displaced in the x -direction and collided with stationary “ball 3”. After this collision, the angular velocity of “ball 3” was in the opposite direction to “ball 2”.

The dimensionless velocities of the ball centroids in the x - and y -directions as functions of time are shown in Fig. 5(a) and (c), with squares, circles, and diamonds representing the dimensionless velocities of “ball 1”, “ball 2”, and “ball 3”, respectively. The dimensionless velocities in the x - and y -directions were defined as $V_x^* = V_x/V_{x0}^{(1)}$ and $V_y^* = V_y/V_{y0}^{(1)}$, respectively. Fig. 5(e) shows ω_{pz}^* , defined as $\omega_{pz}^* = \omega_{pz}/V_{x0}^{(1)}$, where ω_{pz} represents the particle angular velocity as a function of time.

The complex contact dynamics of the particles in this simple polydisperse aggregate were also calculated with a simplified model (Zamankhan & Bordbar, 2006). The results are shown in

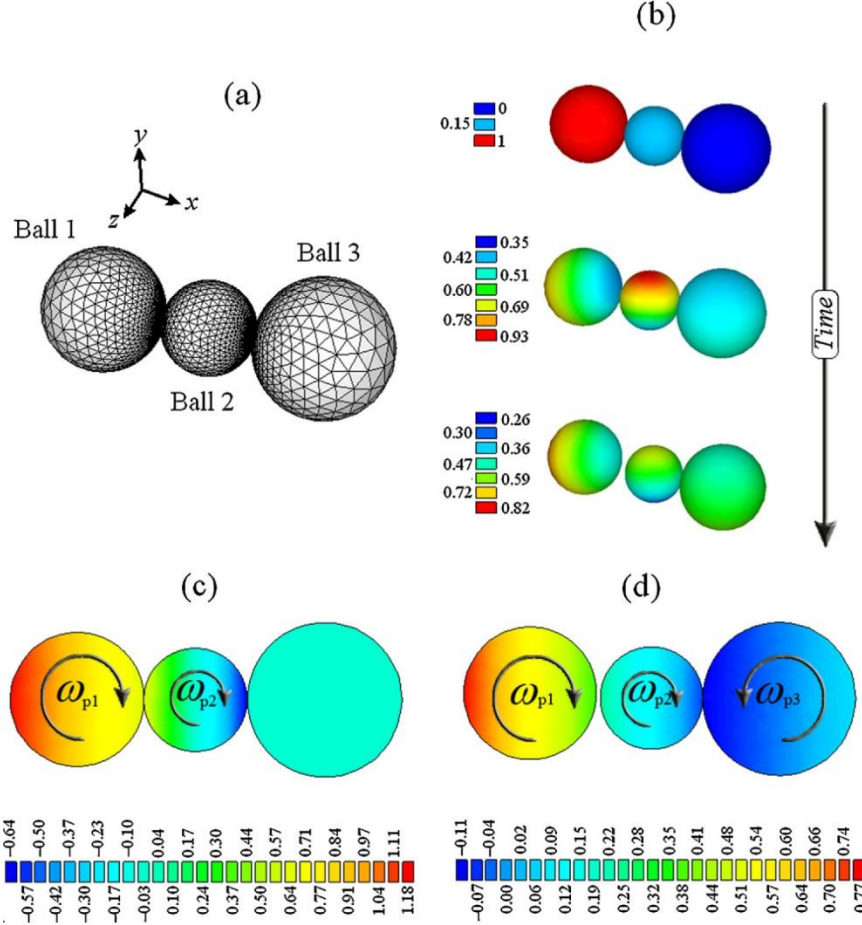


Fig. 4. (a) A polydisperse aggregate and its computational grid. The diameters of ball-1, ball-2 and ball-3 are 500 μm , 350 μm , and 600 μm , respectively. (b) Time evolution of the dimensionless velocities of the particles in the aggregate. At the end of the contact process, ball-2 and ball-3 stuck together. (c and d) Time evolution of the translational and angular velocities of the particles in the aggregate. The two configurations are separated by $t = 20 \mu\text{s}$.

Fig. 5(b), (d) and (f) to assess the ability of the simplified model to predict complex flows of dense granular materials. Fig. 5 shows satisfactory agreement between the FEM results and the predictions of the simplified model.

3.2. A model for the fluid phase

The deviation of pressure below a granular bed of thickness h from ambient pressure is (King et al., 2007)

$$\Delta p = -h\gamma\rho_a(1 - \phi)v_a, \quad (3)$$

where γ describes the grain–air coupling introduced by the use of Darcy's law, ρ_a is the air density, ϕ is the bed porosity, and v_a is the air velocity. Darcy's flow is observed for $0.3 < \text{Re} \leq 0.7$ (Jafari, Zamankhan, Mousavi, & Pietarnen, 2008), where the Darcian Reynolds number is defined as $\text{Re} = \rho_a v_a d_p / \mu_a$ and μ_a is the air dynamic viscosity. The physical properties of air are given in Table 1.

The flow Reynolds number in the experiments described in the preceding section is much larger than 0.7. Hence, the flow regime was probably turbulent (Serini, 2000). The granular bed Reynolds number, used as the demarcation criterion, is defined as $\text{Re}_{slip} = \rho_a |v_a - v_p^i| d_p / \mu_a$, where v_p^i is the velocity of the i th particle.

In this work, an attempt was made to combine the Lagrangian (particle-based) model and LES (Sagaut, 1998) to achieve more accurate simulations of the tilting and, especially, the swirling granular flows. The filtered continuity momentum for an isothermal 3D flow of air is

$$\frac{\partial \bar{\rho}}{\partial t} + \nabla \cdot (\bar{\rho} \tilde{\mathbf{v}}_a) = 0, \quad (4)$$

$$\frac{\partial \bar{\rho} \tilde{\mathbf{v}}_a}{\partial t} + \nabla \cdot (\bar{\rho} \tilde{\mathbf{v}}_a \tilde{\mathbf{v}}_a) = -\frac{1}{\rho_a} \nabla (\bar{\rho} \bar{p}) + \frac{1}{\rho_a} \nabla \cdot (\bar{\rho} \tilde{\sigma}) + \nabla \cdot \tau + \tilde{f}_{pf} + \bar{\rho} \mathbf{g}, \quad (5)$$

where $\bar{\rho}$ is the filtered density, defined as $\bar{\rho} = \rho_a \bar{\phi}$; $\tilde{\mathbf{v}}_a$ is the density-weighted Favre filter velocity, defined as $\tilde{\mathbf{v}}_a = \overline{\rho \mathbf{v}_a} / \bar{\rho}$; and \bar{p} is the filtered pressure at the supergrid scale. The forces exerted by the fluid on the particles per unit volume, \tilde{f}_{pf} , encompass the drag, lifts, added mass, stress, and Basset history forces (Maxey & Riley, 1983); \mathbf{g} is the acceleration of gravity.

The viscous stress tensor in Eq. (5) is defined as

$$\sigma = -\frac{2}{3} \mu_a \nabla \cdot \mathbf{v}_a \mathbf{I} + \mu_a (\nabla \mathbf{v}_a + (\nabla \mathbf{v}_a)^T), \quad (6)$$

where \mathbf{I} is the second order identity tensor.

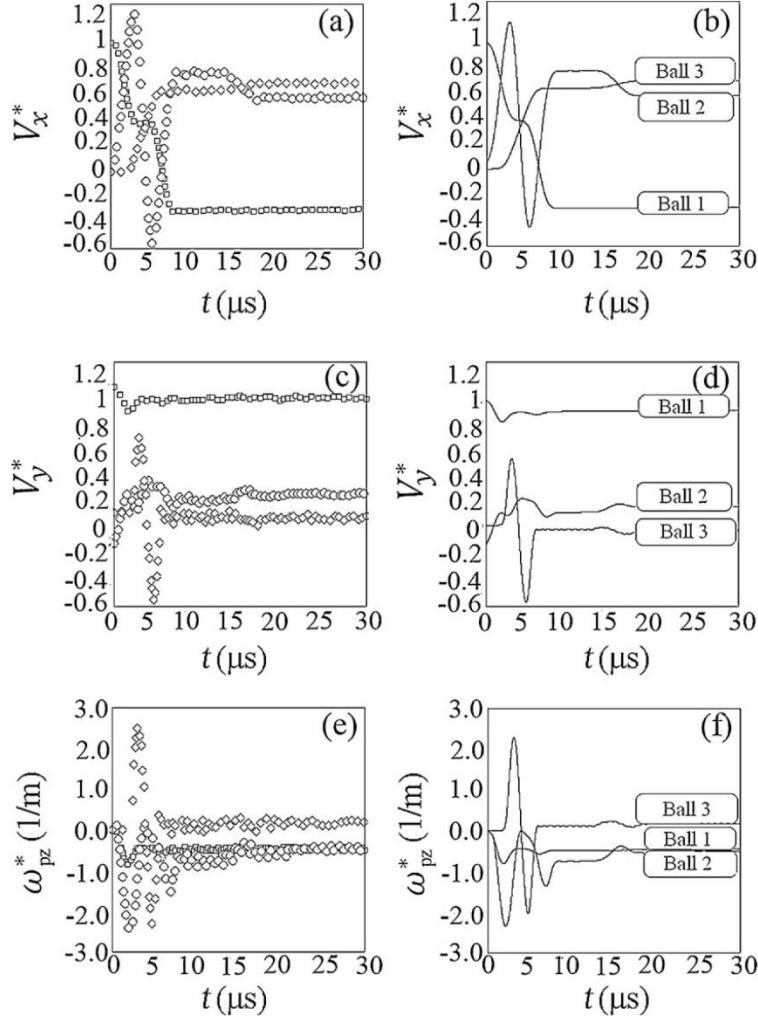


Fig. 5. (a) The computed dimensionless velocity of particles in the x-direction as a function of time using FEM. Here and in (c) and (e), squares, circles and diamonds represent the dimensionless velocities of “ball 1”, “ball 2”, and “ball 3”, respectively. (b) The computed dimensionless velocity of particles in the x-direction as a function of time. Here and in (d) and (f), the results were obtained with a simplified model. (c) The computed dimensionless velocity of particles in the y-direction as a function of time using FEM. (d) The computed dimensionless velocity of the particles in the y-direction as a function of time. (e) The computed angular velocity of particles in the z-direction as a function of time using FEM. (f) The computed angular velocity of particles in the z-direction as a function of time.

In Eq. (5), τ is the subgrid scale (SGS) stress tensor,

$$\tau = -\bar{\rho} \left(\widetilde{\mathbf{v}_a \mathbf{v}_a} - \widetilde{\mathbf{v}_a} \widetilde{\mathbf{v}_a} \right) - \bar{\rho} \left(\widetilde{\mathbf{v}_a'' \mathbf{v}_a} + \widetilde{\mathbf{v}_a} \widetilde{\mathbf{v}_a''} \right) - \bar{\rho} \left(\widetilde{\mathbf{v}_a'' \mathbf{v}_a''} \right), \quad (7)$$

where \mathbf{v}_a'' represents the subgrid-scale part of \mathbf{v}_a based on Favre filtering.

The SGS stress tensor, τ , is required to close the equations for the large scale fields on a grid small enough (but much larger than the Kolmogorov scale) to provide reasonable resolutions. In contrast to the filtered single-phase equations, a conceptual restriction arising from the present approach is that the filter width, Δ , should be larger than the length scale characteristic of the bubble phase. Thus, an appropriate choice of Δ should provide a sufficiently large-scale resolution without violating this restriction.

The particles make a contribution to the process of energy removal from the resolved scales of the fluid phase. This two-way coupling effect may be modelled by superposing particle-induced and shear-induced SGS energy dissipations. A tentative first attempt at closure of the momentum Eq. (5) with an SGS model

for τ , is

$$\tau_{\text{mod}} = -\bar{\rho} \left(\widetilde{\mathbf{u}_f \mathbf{u}_f} - \widetilde{\mathbf{u}_f} \widetilde{\mathbf{u}_f} \right) + \left[2(C_s \Delta)^2 \bar{\rho} (\tilde{\mathbf{S}} : \tilde{\mathbf{S}})^{1/2} + (C_s \Delta) \bar{\rho} (|\mathbf{v}_{\text{slip}}|) \right] \left(\tilde{\mathbf{S}} - \frac{1}{3} \text{tr} \tilde{\mathbf{S}} \mathbf{I} \right), \quad (8)$$

where C_s is the Smagorinsky constant, $C_s = 2 \prod / 3\sqrt{3} (-R(1 + C_{b0} R^2) / K^3)^{1/2}$, R is related to the ratio of the mesh spacing to the Kolmogorov length scale (so that $R = -1 + (\eta/\Delta)^{4/3}$), K is the Kolmogorov constant, C_{b0} is the backscatter parameter, which is set to $C_{b0} = 0.2$, $\tilde{\mathbf{S}}$ is the resolved rate of strain tensor, and \mathbf{v}_{slip} represents the slip velocity.

3.3. Simulation of sand perturbed by an orbital shaker

Simulations of a bed of air-immersed solid particles inside a polycarbonate plastic container were performed with the

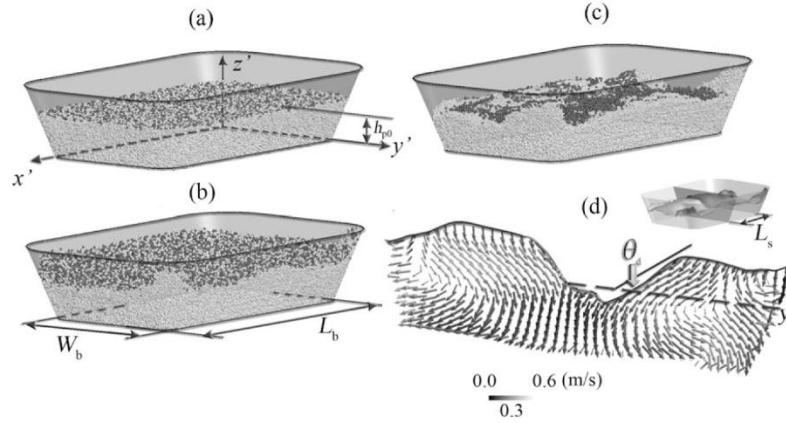


Fig. 6. (a) The initial configuration of the solid particles used for the numerical simulation where $h_{p0} = 3.5$ cm. (b) The instantaneous configuration of the solid particles at $t = 1$ s, with $W_b = 14$ cm and $L_b = 24$. (c) The instantaneous configuration of the solid particles at $t = 2$ s. (d) The computed average particle velocity distribution on a $y'z'$ -plane. Inset: the free surface and position of the plane, $L_s = 11$ cm.

models described in the preceding sections. The time step used in the simulations was $\Delta t = 10^{-7}$ s. In the present case, we used the moving-deforming mesh model where the node motion varied sinusoidally in time and space, and the ratio of the mean particle diameters to the minimum mesh size did not exceed 0.48.

A solid mixture of spherical particles with diameters $d_{pm} = 500$ μm , $d_{ps} = 350$ μm , and $d_{pl} = 600$ μm , was poured into the container to a height of h_{p0} , as shown in Fig. 6(a). The volume fraction of the smallest particles in the mixture was $\phi_{ss} = 0.20$, that of the largest particles was $\phi_{sl} = 0.18$, and the total solid volume fraction in the container was $\phi_s = 0.64$. The free surface of the solid particles was nearly flat at the start of the simulation. The container underwent orbital (horizontal) oscillations of the form of Eq. (1) with $(\omega_x/2\pi = 42$ Hz and $A_x = 10^{-3}$ m) and $(\omega_y/2\pi = 25$ Hz and $A_y = 10^{-3}$ m).

Fig. 6(b) shows the tilted surface of the solid particles until the tilt angle reached θ_d at time $t = 1$ s. Fig. 6(c) illustrates the configuration of solid particles at time $t = 2$ s. Fig. 6(d) depicts the computed average particle velocity field on the $y'z'$ -plane whose position is shown in the inset. The inset also shows the computed free surface of the air-particle interface. The free surface with tilt angle reaching θ_d is highlighted in Fig. 6(d). The computed dynamic angle of repose, $\theta_d = 29^\circ$, was in good agreement with the measured value, as shown in Fig. 2(d).

We compared the results in Figs. 1(a) and 6(c) and concluded that the model captured a number of salient features of the experiments shown in the video. The Reynolds number of the granular

bed is larger than 50, which justifies the use of LES for simulations of tilting granular flows.

3.4. Simulation of swirling granular flows

Fig. 7(a) and (b) illustrates the initial configurations of sand before it undergoes horizontal vibrations as in the video. Similar to the case described in the preceding section, a solid mixture of spherical particles with diameters $d_{pm} = 500$ μm , $d_{ps} = 350$ μm , and $d_{pl} = 600$ μm was used in the simulation. The volume fractions of the small, medium and large particles in the mixture were $\phi_{ss} = 0.20$, $\phi_{sm} = 0.26$, and $\phi_{sl} = 0.18$, respectively.

Fig. 8(a)–(c) shows instantaneous configurations of the particles after $t = 2$ s. Fig. 8(d) depicts the computed average particle velocity field in the xy -plane, in the same position as in the video. A simple analysis of Fig. 8(d) reveals that the average spin rate of the particles was $\omega_p = 15.7$ rad/s, which was nearly constant; the system shown in the video, combined with the mathematical model used in this study, has the potential to be used as a viscometer for dense granular fluids.

Fig. 8(e) shows the computed average particle velocity field in the xz -plane, indicating that a unique swirling-convection regime for granular flow was found in this study. Fig. 8(f) illustrates the computed average air velocity field in the xy -plane, similar to that in Fig. 8(d). As shown in Fig. 8(f), the air is being displaced in the negative x -direction due to the instantaneous acceleration of the container. However, the displacement of solid particles appears to be smaller, as shown in Fig. 8(d).

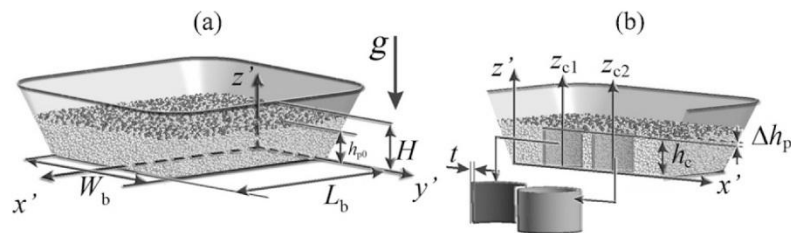


Fig. 7. (a and b) The initial configuration of the solid particles used for the numerical simulation, where $h_{p0} = 3.5$ cm, $H = 6$ cm, $W_b = 14$ cm, $L_b = 16$ cm, $h_c = 3.2$ cm, $t = 0.2$ cm and $\Delta h_p = 0.3$ cm.

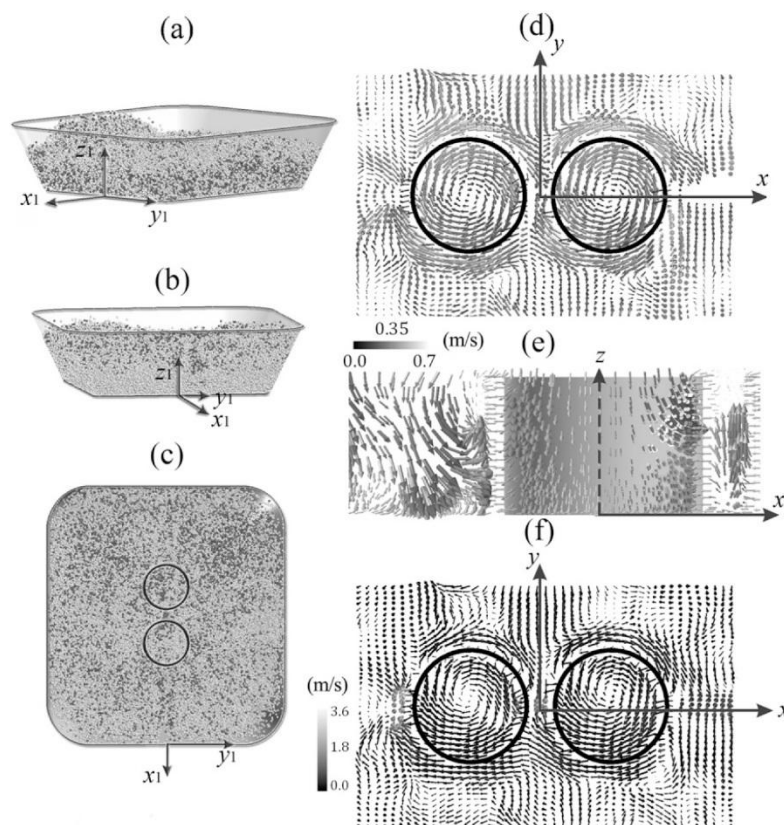


Fig. 8. (a–c) The instantaneous configuration of the solid particles at $t = 2$ s. (d) The computed average particle velocity field in the xy -plane at $z_1 = 3.22$ cm. (e) The computed average particle velocity field in the xz -plane at $y_1 = 0$. (f) The computed average air velocity field in the same xy -plane as (d).

The large granular bed Reynolds number computed for the swirling-convection regime indicates that it is necessary to use LES for accurately simulating complex granular flows.

4. Conclusions

A horizontally vibrated air–grain system exhibited novel swirling granular flow, as shown in the [supplement video](#). The granular bed Reynolds number is in the range $25 < Re_{slip} \leq 180$, which indicates that the flow regime was turbulent.

The new swirling-convection regime was simulated successfully with a Lagrangian (particle-based) method combined with LES.

An optical processing algorithm was developed, which generated a three-dimensional model of the system from photographs taken at multiple locations at approximately the same time.

This image processing algorithm, combined with the Eu/La mathematical methods running on GPUs, is possibly the most interesting approach for future work on the development of a viscometer for dense granular fluids.

Appendix A. Supplementary data

Supplementary data associated with this article can be found, in the online version, at <http://dx.doi.org/10.1016/j.partic.2012.06.005>.

References

- Anderson, T. B., & Jackson, R. (1968). Fluid mechanical description of fluidized beds. *Industrial & Engineering Chemistry Fundamentals*, 7(1), 12–21.
- ASTM International-Standards Worldwide. (2006). ASTM C136-06. Retrieved February 15, 2006, from <http://www.astm.org/cgi-bin/SoftCart.exe/DATABASE.CART/REDLINE.PAGES/C136.htm>.
- Aumaitre, S., Puls, C., McElwaine, J. N., & Gollub, J. P. (2007). Comparing flow thresholds and dynamics for oscillating and inclined granular layers. *Physical Review E*, 75, 061307.
- Autodesk 123D Catch Software. Retrieved March 20, 2012, from <http://www.123dapp.com/catch/>.
- Bai, G., & Bee, J. S. (2012). Computational fluid dynamics (CFD) insights into agitation stress methods in biopharmaceutical development. *International Journal of Pharmaceutics*, 423, 264–280.
- Bandyopadhyay, A., & Basak, G. C. (2007). Studies on photocatalytic degradation of polystyrene. *Materials Science and Technology*, 23(3), 307–317.
- Bejan, A., & Kraus, A. D. (2003). *Heat transfer handbook*. New Jersey: John Wiley and Sons, Inc.
- Colomer, J., Peters, F., & Marrase, C. (2005). Experimental analysis of coagulation of particles under low-shear flow. *Water Research*, 39, 2994–3000.
- Gutman, I. (1968). *Industrial uses of mechanical vibrations*. London: Business Books Ltd.
- Hough, S. (2002). *Earthshaking science: What we know (and don't know) about earthquakes*. New Jersey: Princeton University Press.
- Jafari, A., Zamankhan, P., Mousavi, S. M., & Pietarnen, K. (2008). Modeling and CFD simulation of flow behavior and dispersivity through randomly packed bed reactors. *Chemical Engineering Journal*, 144, 476–482.
- King, P. J., Lopez-Alcaraz, P., Pacheco-Martinez, H. A., Clement, C. P., Smith, A. J., & Swift, M. R. (2007). Instabilities in vertically vibrated fluid–grain systems. *The European Physical Journal E*, 22, 219–226.
- Lekhnitskii, S. G. (1963). *Theory of elasticity of an anisotropic elastic body*. San Francisco: Holden-Day Inc.
- Lemieux, P.-A., & Durian, D. J. (2000). From avalanches to fluid flow: A continuous picture of grain dynamics down a heap. *Physical Review Letters*, 85(20), 4273–4276.

- Maxey, M. R., & Riley, J. J. (1983). Equation of motion for a small rigid sphere in a no uniform flow. *Physics of Fluids*, 26, 883–889.
- Metcalfe, G., Tennakoon, S. G. K., Kondic, L., Schaeffer, D. G., & Behringer, R. P. (2002). Granular friction, Coulomb failure, and the fluid–solid transition for horizontally shaken granular materials. *Physical Review E*, 65, 1–15.
- NVIDIA GPU Computing. (2012). What is GPU computing? Retrieved May 16, 2012, from <<http://www.nvidia.com/object/what-is-gpu-computing.html>>.
- Orpe, A. V., & Khakhar, D. V. (2004). Solid–fluid transition in a granular shear flow. *Physical Review Letters*, 93, 068001.
- Pudasaini, S. P., & Hutter, K. (2007). *Avalanche dynamics*. Berlin: Springer.
- Rabinowicz, E. (1965). *Friction and wear of materials*. New York: Wiley.
- Rubin, D., Goldenson, N., & Voth, G. A. (2006). Failure and strengthening of granular slopes under horizontal vibration. *Physical Review E*, 74, 051307.
- Sagaut, P. (1998). *Large eddy simulation for incompressible flows: An introduction*. Berlin: Springer.
- Serini, V. (2000). "Polycarbonates" in *Ullmann's encyclopedia of industrial chemistry*. Weinheim: Wiley-VCH.
- Zamankhan, P., & Bordbar, M.-H. (2006). Complex flow dynamics in dense granular flows. Part I: Experimentation. *Journal of Applied Mechanics (T-ASME)*, 73, 648–657.
- Zamankhan, P. (2011). Bubbling in vibrated granular films. *Physical Review E*, 83, 021306.
- Zamankhan, P. (2012). Solid structures in a highly agitated bed with a granular material. *Applied Mathematical Modelling*, 36, 414–429.